ON-CHIP LABEL-FREE BIOMOLECULAR CAPTURING AND DETECTION USING INTEGRATED OPTICAL MICRO-RESONATORS

A Dissertation
Presented to
The Academic Faculty

By

Ahmad Usman

In Partial Fulfillment
of the Requirements for the Degree
Doctor of Philosophy in the
School of Electrical and Computer Engineering

Georgia Institute of Technology

August 2018

ON-CHIP LABEL-FREE BIOMOLECULAR CAPTURING AND DETECTION USING INTEGRATED OPTICAL MICRO-RESONATORS

Approved by:

Dr. Ali Adibi, Advisor
School of Electrical and Computer Engineering
Georgia Institute of Technology

Dr. Gee-Kung Chang
School of Electrical and Computer Engineering
Georgia Institute of Technology

Dr. Benjamin D.B. Klein
School of Electrical and Computer Engineering
Georgia Institute of Technology

Dr. Azadeh Ansari
School of Electrical and Computer Engineering
Georgia Institute of Technology

Dr. Rick Trebino
School of Physics
Georgia Institute of Technology

Date Approved: July 24th, 2018

Dedicated to the loving memory of my “Maa Jee”

Amna Sarfraz

(April, 1960 - February, 2010)

May her soul rest in peace.

ACKNOWLEDGEMENTS

I would like to thank my advisor, Professor Ali Adibi, for his guidance and endless support throughout my time at the Georgia Institute of Technology. I thank him for his respect, concern, and confidence in me. I may not be able to appreciate him enough for allowing me to pursue my interests, and for enabling an extremely relaxed working environment for me. It has been a pleasure working under his supervision, learning from his experience and expertise.

I would like to thank Professor Gee-kung Chang and Professor Benjamin D.B. Klein for reviewing my PhD proposal, PhD thesis, and serving on my PhD defence committee. I would like to thank them for their insights and advice on the work. I would also like to thank Professor Rick Trebino and Dr. Azadeh Anasari for their feedback on my work and serving on my defense committee.

I would especially like to thank Dr. Ali Asghar Eftekhar (Reza Eftekhar) for his patience dealing with me. I may not be able to thank him enough for his support, care, concern, patience, and time which he has given me throughout the duration of my PhD. For someone like me, with no background in optics, nanotechnology, microfabrication, biosensing, and integrated photonics, he has always been there for the individual meetings, discussions, and sharing ideas. I have learned a lot from him. I wish him all the success and happiness.

I would like to thank the members of the Photonic Research Group, with whom I had an amazing time. I would especially like to thank my dear friend Dr. Razi Dehghannasiri. When I first joined this group, I really did not have any idea and experience regarding optics, rest assured integrated photonics. I truly learned a lot from him and gained a respectable insight regarding integrated photonics through our profound discussions. It has been an amazing time with him. I heartily thank him for the numerous insightful discussions, motivation to stay in the field of optics, and laughs. I will always cherish the time

I have spend with him. I would like to thank my friends Hossein Taghinejad, Mohammad Taghinejad, and Dr. Hesam Moradinejad for the amazing time we had together in the group. I would also like to thank Tianren Fan, Dr. Hamed Shams Mousavi, Dr. Amir H. Hosseinnia, Dr. Reza Pourabolghasem, Dr. Hossein Taheri, Dr. Majid Sodagar, Dr. Zhixuan Xia, Dr. Farshid Ghasemi, Dr. Payam Alipour, Dr. Qing Li, and Dr. Murtaza Askari. I would also like to thank the recent members in the group Xi Wu, Yashar Kiarashinejad, Sajjad Abdollahramezani, Ali Eshaghian Dorche, Iman Taghavi, and Sara Bitarafan. I wish all of them the best for their future endeavours. I would also like to thank all the lab managers and especially Nicole Brown for diligently managing all the lab-support of the group for the last two years.

I would like to acknowledge the staff of Institute of Electronics and Nanotechnology (IEN) for their dedication towards running the cleanrooms (Marcus and Pettit) at Georgia Tech smoothly. In particular, I want to acknowledge Gary Spinner, Devin Brown, David Gottfried, Viny Nguyen, Eric Woods, Ben Hollerbach, Charlie Suh, Hang Chen, Rebhadevi Monikandan, and Chris (Yeyuan) Yang for their efforts and professionalism. I would like to thank the support staff at the School of Electrical and Computer Engineering, in particular Dr. Daniela Staiculescu and Tasha M. Torrence for their courteous support and professionalism towards me throughout my program.

I would like to thank my friends Muhammad Faizan Khan (Faizi) and Saba Azhar Khan (Meechu) for their support, love, and care when I needed that the most. I wish them all the happiness and success for this life and hereafter. I would like to thank my friends Talha Ahmad Khan and Nauman Shahid for the support and advice on applying to the Fulbright Scholarship. I would like to thank my friends Kausar Abbas and Usman Sadiq for the guidance they have provided throughout the Fulbright application process.

I would especially like to thank my homemates at 389 Calhoun, 1014 Hemphill, and 511 Lynch: Hassan Jaleel, Sajid Saleem, Bashir Akbar, Saad bin Nasir, Ubaid Ullah Fayyaz, Shoaib Azmat, Faisal Kakar, Asif Ali, Dildar Ali Lakho, Usman Ali, Muhammad Shahbaz,

Hamza Abbasi, Omer Lateef, Muhammad Ali Murtaza, Mubeen Ahmad, Muhammad Amir Shafiq, Zaheer Ahmad, Muhammad Asif Rana, Nauman Ahad, Ahmad Mubeen Piracha, Muhammad Usama, Aqeel Anwar, Muhammad Ali, Ahmal Jawad Zafar, and Habib Ahmad. Its been memorable staying with all of you. Atlanta was and will remain a home for me because of the memories associated with all of you.

I would like to thank the Georgia Tech Pakistani community, especially my friends who came throughout all these years for Masters and PhDs: Waseem Abbas, Ali Ahmad Chugtai, Abdul Basit Memon, Muhammad Umer Tariq, Umair bin Altaf, Fawad Naizi, Haider Ali, Usman Gul, Farhan Aziz, Qazi Javed, Ahsan Qamar, Munzir Zaffar, Abdul Qadir, Taha Kasim, Abdul Majid Naveed, Hasan Masud, Hussain Raza, Muneeb Zia, Aneeq Zia, Ali Narang, Muhammad Abdullah, Syed Hassan Ahmad, Zahid Bhiwas, Muhammad Fuzail, Bilal Raja, Assad Hussnain, Ebrahim Zakaria, Waqas Majeed, Ismaeel Sadiq, Sahibzada Yousafzai, Ebrahim Zakariya, Usama Shahzad, Muhammad Rizwan, Aftab Ahmad, Qazi Javed, Irfan Abid, Ali Kazim, Fareed Jaffri, Talal Hasan Siddiqui, Hussain Zaheer, Muhammad Ali Antho, Syed Bilal Khalid, Haseeb Sheikh, Burhan Ahmad, Naveed Hasan, Adil Kamal Mir, Waqas Waheed, Haris bin Tariq, Usama bin Sikandar, Amir Ayub, Rehan Khalid, Muhammad Umer Qureshi, Sharjeel Khan, Syed Abdullah Nauroze, Ismaeel Kakakhel, Safee Shah, Saad Javed, Ahmad Nawaz Warrich, Azhar Khalique Shar, Fahad Razzaq Bhatti, Rana Bilal Iftikhar, Shahmeer Umer, Shafat Mushtaq, Hasan Waqar Gillani, Muhammad Mujeeb-ur-Rahman, Shareef Khalid, Abbas Gillani, Sahil Shah, Adil Shah, Zubair Irshad, Abdul Hamid, Annand Kumar, Arsalan Ali, Saad Zia, Waqas Sandhu, Mian Usman, Irtaza Haider, Raza Jafri, Shehzaan Farooqui, Nayyab Abdullah, Syed Haroon Hussain, and Arslan Shahzad.

I would like to thank the Pakistani ladies community at Georgia Tech, especially the wives of my friends for the hospitality and warmth they have shown towards the community throughout these years: Sadia Shakeel, Bushra Tassaduq, Abeera Sohail, Sidra Nizamuddin, Ifrah Saeed, Aaliya Shahzadi Hira Batool Rizvi, Marzia Rizvi, Ayesha Rasheed

Khan, Saima Yawar, Houma Raheel, Qandeel Almas, Amna Tariq, Farwa Akhtar, Tabish Jaleel Shaikh, Baria Sameen Manahill, Fizza Hassan Khan, Syeda Fatima Hafsa, Sahrish Jaleel Shaikh, Mishele Ijaz, Bushra Khalid, Rida Shazli, Muzna Shibli Farooqui, Rabeeya Jamshad, Sana Mazahir, Isha Lodhi, Mrs. Burhan Ahmad, Mrs. Abdullah Nauroze, Mrs. Irfan Abid, Mrs. Ismeel Sadiq, Mrs. Ismaeel Kakakhel, Mrs. Muneeb Zia, Mrs. Wasif Tanveer, Mrs. Bashir Akbar, Mrs. Ahsan Qamar, Mrs. Usman Gul, Mrs. Munzir Zaffar, Mrs. Umer Tariq, Mrs. Abdul Qadir, Mrs. Daniyal Hasan, Mrs. Amir Shafiq, Mrs. Safee Shah, Mrs. Ali Murtaza, Mrs. Omer Lateef, Mrs. Hamza Abbasi, Mrs. Saad bin Nasir, Mrs. Saad Javed, Mrs. Rizwan, Mrs. Fawad Naizi, Mrs. Qazi Javed, Mrs. Assad Hussnain, and Mrs. Etizaz H. Shah.

I would like to thank my friends from all around US with whom I travelled, who came to visit Atlanta, and allowed me to have a memorable time and great memories: Asad ur Rahman, Qazi Fazli Azeem, Raja Faran, Adnan Munawar, Khawaja Umair Najam, Anosh Mehdi, Zia-ur-Rahman, Adil Ismaeel (Addy Adil), Zulqarnain Haider, Shahzad Hameed, Mujahid Hanif, Habib Hussain, Muneeb Rathore, Rizwan Naru, Waqas Hasan, Aneeq Cheema, Talha Rahmani, Salman Manzoor, Muhammad Hasan, Tayyaba Razi, Ayesha Batool, Farah Azhar, Tehmina Pirzada, Amina Rizwan, Hera Naguib, Mariam Ishaq, Safyah Zafar Usmani, Natasha Iqbal Jozi, Hira Amna Saleem, Ayesha Aslam, Hira Nafess Shah, Soabah Waseem, Asma Saeed, Fatma Faruq, Madiha Ansari, Samiha Naseem, Eefa Tabsuum, and Rafia Farooqui.

I would like to thank the ”Atlanta Muhallah Kids” for making my time here memorable. I have seen many of you born, grow up and be a source of joy for your parents and for the rest of the community: Abdullah, Daniya, Musa, Mahad, Zeenia, Azlan, Yummna, Amna, Omer, Mariam, Arhab, Maryum, Mohammad, Horiya, Fazal, Innayat, Maria, Bareera, Abdullah, Eshaail, Enaya, Amber, and Aemen.

I would like to especially thank my first housemates Dr. Hasan Jaleel, Dr. Sajid Saleem, and Dr. Bashir Akbar for their love, care, support, guidance through my initial time in US

and Georgia Tech. I would like to thank Dr. Syed Minhaj Hassan and Dr. Saad bin Nasir their friendship. I will always cherish these memories. It has been a great company and an awesome time with all of them.

I would like to thank Mohsin Mukhtar, Rana Muhammad Umer, and Rameez Talat for being my initial ”partners in crime” in US. The memorable road trips, parties, dinners, courses, assignments, projects, in short numerous adventures we had together, will remain with me for the rest of my life.

To Syed Etizaz Hassan (Shah Jee), Awais Riaz, and Daniyal Hassan : Guys ! I will always cherish the time we had together. The moments of madness, the all nighter ”sughal and rang-bazi”, the gossips, the serious talks, Daniyal becoming a father, Shah Jee’s wedding, Awais’s never ending ”solo charismatic trips”, the cricket, the conference calls, in short, all the craziness. Thank you for these never ending awesome memories.

I would like to thank my Indian friends Anush Daruwala, Sagarika Mukesh, Toshak Singhal, and Souryadeep Bhattacharaya for a great company and friendship.

I would like to thank the US Fulbright Scholarship Program, Institute of International Education (IIE), United States Educational Foundation for Pakistan (USEFP), and the Higher Education Commission (HEC) of Pakistan for providing me an opportunity for higher education. I would like to especially thank the late US. Senator J. William Fulbright for initiating the Fulbright scholarship program and Dr. Atta-ur-Rahman of Pakistan for revitalizing the HEC and extensive efforts towards the higher education in Pakistan. I would also like to thank all the tax-payers in the United States and Pakistan contributing towards these higher education programs and opportunities. I would like to acknowledge my Fulbright and USEFP advisers Brian Diffely, Athena Lao, Betsy Barringer, and Rahat Karim for their support and help throughout the scholarship and PhD program.

I would especially like to thank the management and people associated with the Al-Farooq Islamic Center and Dar-ul-Noor Academy for their efforts and support for the Muslim community in Atlanta for all these years.

Last but not the least, I would like to thank my family members in Pakistan for their support and prayers throughout my journey. I am unable to thank them enough for what they have done for me especially, my father Abdul Majid Sheikh and my brother Hamid Iftikhar. I would like to thank my “Jigoo Boboo” for the unconditional love and support. I would like to thank my uncles Abdul Wahid Sheikh, Ayaz Imam, Ch. Muhammad Riaz, Shahid Imam, Zahid Imam, Abid Imam, Rashid Imam, Dr. Shahzad Hussain, Sajjad Imam, Col. Faisal Karim Shami, Azhar Gul, and Dr. Sajjad Shami. I would especially like to thank my aunt (phuphoo) Shahida Riaz for her prayers, emotional support, and motivation throughout my journey. I would also like to thank my other aunts Dr. Shamshad Wahid, Shamshad Ayaz, Asma Azhar, Sarwat Shami, Farah Shahid, Seema Zahid, Raheela Abid, Bina Rashid, Maleeha Shahzad, and Afshan Sajjad for their support and prayers throughout my PhD journey. I would also like to thank all my cousins and friends as well.

Ahmad Usman

Ramazan - 1439

TABLE OF CONTENTS

LIST OF TABLES

LIST OF FIGURES

SUMMARY

The objective of this research is to investigate and demonstrate compact lab-on-a-chip (LOC) sensor for the post translational modification (PTM) profiling of the proteins used as biomarkers, for early cancer detection. The LOC sensor comprises of an on-chip pre-concentration and filtering device to isolate the targeted low-abundance proteins form the complex input samples and an integrated photonic sensor microarray for profiling the molecular structures of the isolated protein epitopes. The motivation of this work is extracted from the inability of conventional affinity-based pre-concentration and separation techniques for elucidating PTMs of the proteins, and the unavailability of LOC sensors for this task. The multi-disciplinary research has been focused towards the integration of functional proteomics, microfluidics, and nanofabrication, employing principles of theoretical modeling and simulations, microfluidics, surface chemistry, and nano-optics for the realization of a novel integrated LOC platform for pre-concentration, filtration, and label-free detection of proteins and biomarkers.

CHAPTER 1
INTRODUCTION

1.1 Overview

The work presented in this dissertation is focused towards developing a compact Lab-On-Chip (LOC) sensor for profiling of the post translational modifications (PTMs) of proteins as a biomarker for early cancer detection. The proposed and developed LOC sensor comprises of a pre-concentration and filtering device to extract the low-abundant target protein (or proteins) from the complex input biological sample, and a sensor microarray to profile the molecular structure of the PTMs of the extracted proteins by targeting the desired set of the PTMs epitopes.

Cancer is one of the leading cause of death in the developed countries. In the recent years, many clinical approaches have been developed which have resulted in better prognosis, if the cancer has been detected in its early stages. Many of the Cancer cases are detected in their late stages, where the Cancer has already been spread via the metastasis. This corresponds to poor prognosis and is a leading cause of the Cancer related fatalities.

The existing clinically approved biomarkers for cancers are proteins that are produced through alternative pathways in the non-cancerous cells. The major limitation of these biomarkers is the inability to provide satisfactory sensitivity and specify for the early cancer detection. However, the production of these proteins in the cancerous cells has been done via pathways that result in aberrant changes in the molecular structure of these proteins, specifically to the attached glycoforms. These aberrations (glycosylation) are considered as the PTMs, occurring mainly because of the presence of the tumor or cancer related processes.

Prostate Cancer (PCa) is the second leading cause of deaths owing to the Cancer, in

men, in the United States [1]. Currently, the only PCa biomarker used by the urologists is the Prostate-Specific Antigen (PSA), along with the digital rectal examination (DRE). However, the specificity and reliability of PSA as a biomarker for PCa has been questioned [2],[3]. The PSA-based screening can lead to over-diagnosis and over-treatment, as the PSA is also produced by the benign prostate hyperplasia (BPH). Recently, the American Cancer Society (ACS) has recommended not to use the PSA screening for the PCa detection. Alternate biomarkers have been being considered, such as "Early PCa" antigens (EPCA) and EPCA-2, but the preliminary studies with these and other potential biomarkers, even in combination with the PSA, has not been impressive in offering a promising alternative [4],[2]. However, the PSA is a heavily glycosylated glycoprotein and few of the recent studies have evaluated various glycosylated forms of the PSA (termed as glycoforms) as a biomarkers for the PCa. The analysis of these glycoforms of the PSA from normal and from the prostate specific cell line (LNCaP) has revealed major differences in their glycan structures [5]. Therefore, the profiling of the PSA glycoforms can be used as an effective approach for early detection and quantification of the PCa.

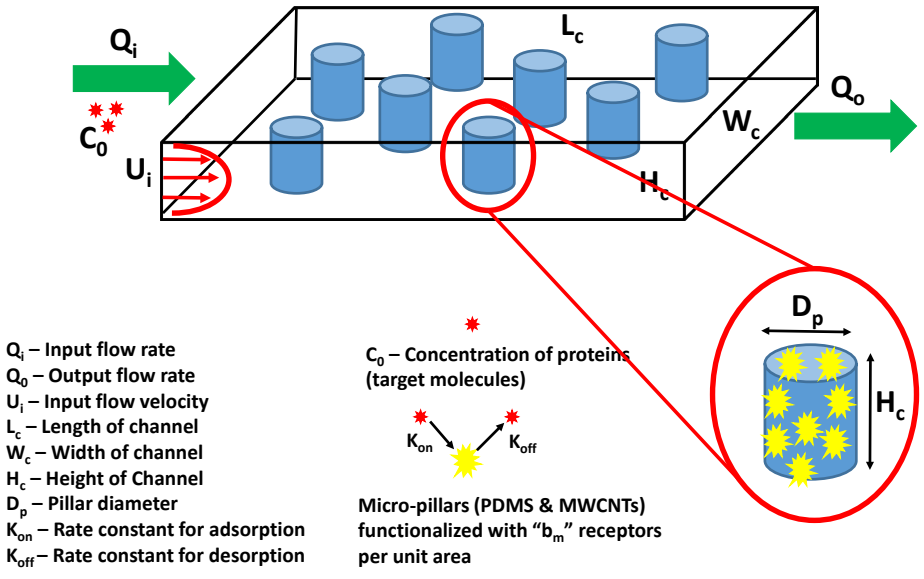

Figure 1.1: An illustration of a multiplexed silicon cavity microresonator (microring) based sensing platform

The motivation of this work has been extracted from the lack of ability of the conventional affinity-based pre-concentration and separation techniques for elucidating PTMs of proteins. Currently, a major technique for the analysis of different glycoforms present in a biomarker is the "mass spectroscopy" (MS). This technique employs isolation of biomarker proteins from the patient serum for quantification and analysis of the glycoforms. However, this technique is not accessible to many general purpose diagnostic laboratories and is impractical for the point-of-care (PoC) applications. The focus of the work is therefore, towards the integration of the functional proteomics, microfluidics, and nanofabrication techniques for the development of a novel integrated platform for pre-concentration, filtration, and label-free detection of proteins and biomarkers.

In this work, I have proposed and demonstrated a LOC sensing platform for profiling of the glycoforms of protein biomarkers based on integration of 1) a compact on-chip sample preconcentration and filtering module (Figure 1.1) that will isolate the target glycoprotein biomarkers form the complex biological sample (which includes many other analyte with similar glycoform structures), and 2) a lectin microarray based on highly-sensitive integrated photonic sensors (Figure 1.2) to profile the concentration of the biomarkers with different glycoforms in the pre-concentrated sample. The lectins have a specific ability to recognize certain carbohydrate moieties of the glycoconjugates, and can be used to specifically capture and identify the target glycoforms. The research conducted through-out this work has been highly multi-disciplinary that primarily included different theoretical modeling and simulations, nanofabrication, surface chemistry development, and characterization steps, needed to realize a proof of concept development for the envisioned LOC sensor.

1.2 Organization

Chapter 2 of the thesis presents a brief literature review, discussing the existing works and associated challenges to the biomolecular preconcentration devices, carbon nanotubes (CNTs) for biomolecular filtering, the need for glycoprofiling, in particular glycans as

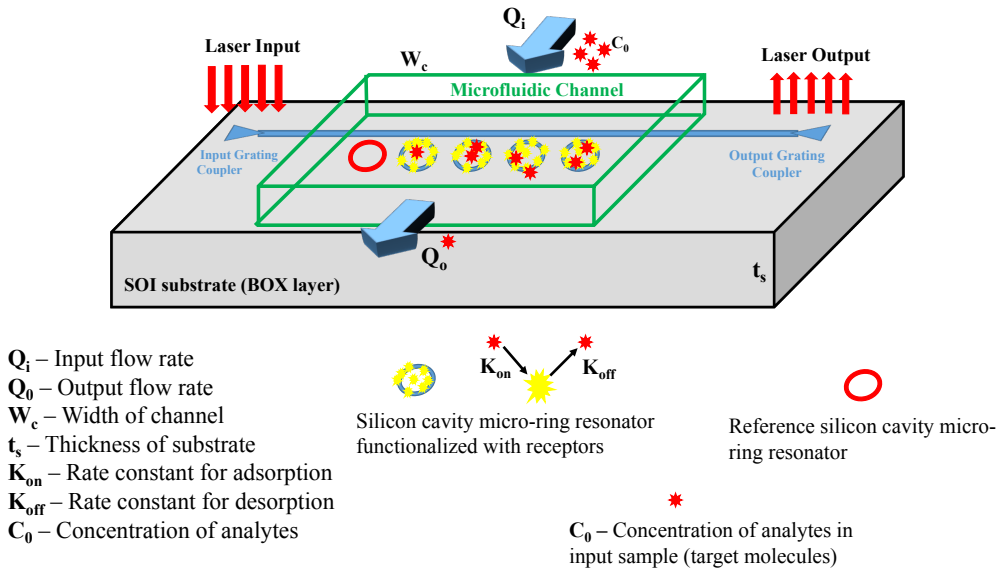

Figure 1.2: An illustration of a multiplexed silicon cavity microresonator (microring) based sensing platform

biomarkers, and optical LOC sensors with a focus towards the silicon microring resonator based platforms for biosensing applications. It also presents an overview on the existing works on various surface chemistries for different biocompatible surfaces primarily silicon, glass, polydimethylsiloxane (PDMS), and multiwall-CNTS (MWCNTs).

Chapter 3 discusses in detail the fabrication challenges I have encountered during the fabrication of PDMS based microfluidic devices. It discuses multiple approaches for fabrication of the microfluidic devices, along with the necessary modifications and optimizations required to achieve repeatable results using the available tools and recipes in the literature.

Chapter 4 presents detailed discussions on the optimized surface chemistries employed throughout the course of this thesis for silicon, glass, PDMS, and MWCNTs surface functionalization. It presents detailed protocols for surface functionalization and corresponding surface characterization results using X-ray photoelectron spectroscopy (XPS), Fourier-Transform Infrared (FTIR) spectroscopy, and fluorescence measurements.

Chapter 5 presents an approach for biomolecular (e.g., proteins, biomarkers) filtering, pre-concentration, and release on demand based on affinity-based separation approach. In this approach, the target biomolecules are captured and pre-concentrated on a surface i.e., PDMS micropillars, based on the binding of the biomolecules to their specific affinity epitopes. A photo-cleavable (PC) biotin linker has been utilized to achieve the desired biomolecular pre-concentration and release. The work also presents a detailed protocol for on-chip affinity-based capturing, pre-concentration, and release of PSA biomarker using the PC-biotin linkers, along with on-chip glycoprofiling capability for ultra-sensitive PSA detection.

Chapter 6 discusses the used of MWCNT forests and micropillars for enhanced biomolecular capturing, pre-concentration, and release applications. It presents a detailed analysis on growth, fabrication, and chemical functionalization of the MWCNTs, with a focus towards PSA biomolecular capturing, pre-concentration, release, and glycoprofiling.

Chapter 7 discusses the details for fabrication of highly sensitive, high-Q optical microresonators for enhance chemical and biomolecular detection applications. The chapter addresses the design challenges for highly sensitive, compact, and scalable optical microresonator based sensors, presenting a multiplexed and array based design approach for bulk and on-flow sensing applications. The chapter also presents an overall picture of highly sensitive and enhanced PSA sensing and glycoprofiling platform by incorporating the microfluidic pre-concentration devices (i.e., PDMS micropillar based platform, MWCNTS micropillars and forests based platform) and the microresonator platform.

Chapter 8 briefly presents the overall contributions of the work and discusses the future prospects related to the conducted research.

CHAPTER 2
A BRIEF OVERVIEW ON ISSUES AND CHALLENGES FOR THE RESEARCH EFFORT

2.1 The need for on-chip biomolecular pre-concentration

The nanotechnology has enabled early detection, diagnosis, prognosis and selection of therapeutic strategies for various diseases. The ability to analyze multiple and broad range of biomolecular samples in real time allows the nanotechnology to be the front runner in the biomedical research. Biomedical research has extensively benefited from the advances in nanoscale fabrication, surface chemistry and material interactions. These advancements have enabled the realization of micro and nanoscale biosensing platforms, which are capable of detecting numerous analytes such as sugars, proteins, DNA, enzymes, bacteria, and viruses, present in a biological sample, allowing both qualitative and quantitative analysis [6]. Moreover, the advancements in microfluidic chip technologies have enabled miniaturization of many biochemical techniques, resulting in faster and cheaper analysis using much smaller amount of biochemical reagents [7].

Towards the goal of "early disease detection", and particularly cancer detection, monitoring the concentration of biomarkers (proteins) in a biological sample is of utmost importance. The biomarker concentrations can be extremely small during the early stages of the disease and therefore, are very difficult to detect. Accurate measurements of concentration with limits down to "ng/ml" or "pg/ml", are required in most cases to differentiate between presence and absence of a disease. A typical sample of blood contains more than 10,000 different proteins with different orders of varying concentrations [8]. The analysis for a specific protein in such a high background noise results in decreased sensitivity, dynamic range, specificity and efficiency. Moreover, the proteins are extremely sensitive to

the ambient environment including temperature, pressure, humidity, pH, ionic strength, etc [9]. This makes the detection extremely cumbersome in low concentration and low quantity samples. The sensitivity, diversity, and complexity of the biological samples, along with the need to specifically determine an analyte (protein), have forced the researchers to explore and develop efficient biomolecular pre-treatment (separation, purification) and detection technologies. Various sample pre-treatment functions such as cleaning, filtration, mixing, heating, and concentration before the analysis, have been demonstrated on-chip [10], which are traditionally performed in off-chip environment.

Apart from the above mentioned challenges, there are numerous other aspects behind the importance of sample pre-concentration before its analysis. The most important aspect is the ability to detect trace or low abundant species, which is particularly important for the clinical diagnostics, forensics, environmental monitoring, and defense and safety applications [11]. Pre-concentration improves sensitivity of detection and reliability of analysis by significantly improving signal-to-noise ratio (SNR), especially when high performance optical detection is employed. Extremely small sample volumes are required of the order of nanoliters and picoliters, compared to milliliters of volumes required for routine off-chip sample analysis, resulting in reduced consumption of the biological samples and reagents [11].

On-chip sample pre-concentration methods are broadly classified into three techniques namely "surface binding technique", "electrokinetic equilibrium technique", and "nanoporous membrane technique" [11]. Surface binding techniques utilize hydrophobic, electrostatic, or affinity interactions between the analytes and the microchannel surface. Solid Phase Extraction (SPE) technique, affinity columns and affinity based adsorption on surfaces for concentration and solvent based surface modification for elution, lies in this domain [11]. Techniques such as field amplified sample stacking [12], isotachophoresis [13], isoelectric focusing [14], and electrokinetic sweeping [15], that employ multiple buffers with different conductivities to achieve desired sample pre-concentrations, are part of electrokinetic

equilibrium techniques. Nanoporous membrane techniques exploit size based separation employing nanoporous membranes or concentration polarization to achieve concentration of the analytes. Techniques such as dielectrophoresis [16] and ion concentration polarization [17] are considered extension of this technique.

In the realm of protein purification, proteins have been enriched on the basis of their solubility, size, charge, and specific binding affinity [18]. The biological samples are subjected to a series of separations based on different properties to yield a certain purity of a protein. Protein concentrations need to be determined at every stage and substantial quantities of the proteins, of the order of milligrams, are needed to be purified to completely elucidate their 3D properties [18]. Nanoporous membrane and electrokinetic equilibrium techniques have demonstrated high concentration factors [11]. However, these techniques require intricate buffer handling, are fabrication intensive, have complex working principle, and need highly skilled operators [19]. Protein precipitation is an issue resulting in clogging of the microfluidic chips and wastage of the expensive sample [19]. Moreover, they also require high electric fields per unit area of operation, resulting in localized heating (joule heating), sample evaporation, electrode malfunctioning, and denaturing of the sample [19].

Surface binding techniques, in particular solid phase extraction (SPE), immunoprecipitation [20], and affinity based separation methods have found much interest of the researchers for protein enrichment [11]. Numerous surface binding techniques have been explored, developed and employed for protein purification based on the "binding affinities" such as Biotin-Avidin (or Streptavidin), lectin-glycan, nucleotide-coenzyme, protein A/G, and immunoaffinity (antibodies-antigens) [21]. The Biotin-Avidin affinity based separation mechanism is of particular interest to the scientific community for its rapid bond formation, and for being the strongest known non-covalent affinity interaction ($K_d = 10^{-15}$) between a protein and a ligand [22]. However, harsh conditions, such as denaturing buffer [23], acid cleavage [24], or treatment with excess biotin [25], are needed for the release of

the captured proteins (i.e., breaking of the Biotin-Avidin bond is required). These methods can result in sample degradation, introduction of contaminants (due to the release of non-specifically bound proteins), elution of endogenous proteins (along with the desired protein), etc. [23].

To address these challenges, various "cleavable linkers", compatible with affinity probes have been developed such as disulfide [26] or diazobenzene [27], enzymatically cleavable peptides [28], and acid [29] and nucleophile [30] based cleavable linkers. These linkers introduce an additional component in the released biochemical mixture and add an additional chemical modification stage in the whole process [23]. Therefore, the desired ideal linker is supposed to be stable under various harsh chemical conditions, compatible with post-ligation analytical processes, and most importantly, circumvents the need for exogenous reagents. Recently, "photo-crosslinkers have shown promise because of their rapid photolysis property, which have led to development of photo-cleavable (PC) affinity tags for enrichment of proteins and biomolecules [31],[32]. These PC affinity tags allow on demand release of enriched proteins/biomolecules and have attracted respectable interest for biomolecular filtering, enrichment and quantification. An interesting demonstration is a microfluidic purification chip (MPC) developed for multiplexed detection and purification of two different cancer biomarkers in a whole blood sample [33]. The MPC captures the cancer biomarkers from the flowing solution using a silicon pillar based capturing chamber. Later, the captured cancer proteins are released for detection using electrical transducers [33].

2.2 Material aspects for realization of enhanced biomolecular capturing and preconcentration devices

Another important aspect for the realization of high performance LOC microfluidic preconcentration devices is the material compatibility. Polydimethylsiloxane (PDMS) is one of the most commonly used material for microfluidic applications [34]. It is a biocompati-

ble, transparent, and soft rubber-like polymer which can be easily patterned using the well-established soft lithography fabrication techniques [35]. It enables the current microfluidic platforms to have efficient fluid handling capability, fluid processing, and also allows small volumes of reagents to be used on-chip to perform rapid, low-cost, quantitative and clinical analysis involving different types of proteins and biomarkers for various on-chip diagnostic applications. One of the key advantages of PDMS enhanced microfluidic technologies is the ability to detect extremely low concentrations from small sample volumes (e.g., upto attomolar) [36]. The miniaturization and application specific tailoring of the PDMS based microfluidic chips results in enhanced reaction kinetics between the species, resulting in a capability for rapid detection of desired species (e.g., it takes less than 45 minutes to perform an on-chip ELISA compared to a 4 to 6 hour conventional ELISA procedure using 96 well plates) [37].

Extensive efforts have been made to optimize the design of the microfluidic devices employing chemical reaction kinetics and fluid mechanics, in conjunction with finite element modeling techniques[38], [39]. An elegant and detailed analysis of the modeling based approach can be found in [40]. Numerous surface chemistries (e.g., aldehydes, amines, azides, carboxy, thiol terminal groups, etc.) have been developed for PDMS based on-chip microfluidic immunoassays and immunoaffinity based biomolecular enrichment [41]. On-chip immunoprecipitation for protein purification using PDMS micro-columns [20], PDMS micropillar arrays for on-chip immunodiagnosis [42], and on-chip ELISA assay for immunosensing applications using PDMS microfluidic channels [43] has been demonstrated in the literature. Detailed reviews and comprehensive analysis of PDMS based immunoassays, affinity based protein immobilization and enrichment techniques, and the current state of the art can be found in [44] and [45].

Apart from the role of PDMS, LOC biomolecular separation and filtration has greatly benefited from the development of nanoporous materials. Efficient biomolecular separation using nanoporous materials requires controllable pore sizes, length and surface chemistry

[46]. The pores are required to have a uniform diameter distribution in order to achieve highly selective filtration. Also, high porosity is required to obtain desired analyte flux [47]. Porous designs allow fluid flow both around and through the porous elements, enhancing physical interactions between the particles in the flow and the functionalized porous surfaces [48]. In addition, the large surface-to-volume ratio of porous materials increases the functional surface area in a given volume and presents an opportunity to target and isolate multiple particle types using a single device [48]. Furthermore, integration of nanoporous materials in microfluidics enables access to a largely unexplored spectrum of smaller submicrometer species that the current LOC bio-MEMS platforms are trying to interact [49].

Commercially available nanoporous materials exhibit large size distributions and relatively large thicknesses, making them practically challenging to integrate these with on-chip microfabricated devices [49]. The inclusion of porous materials into microfluidic platforms has generally been limited to materials such as silicon, porous silicon, silicon nitride membranes, and polymer/silicon monoliths, whose degree of geometrical definability is not sufficient to enable accurate flow control inside microchannels [49]. This limits the porous technology as an alternate to solid affinity-based separation mechanisms, with their adoption limited to porous plugs or particle filtering membranes in on-chip microfluidic filtration applications [50].

Recently, carbon nanotubes (CNTs) have been considered as an alternative porous material for biomolecular separation and filtration applications. The CNTs are textured elements which can be grown vertically with extremely high porosity, resulting in dense forest shaped textured structures [51]. This allows them to be utilized for nanoscale separation [52], filtration and specific targeting of biomolecules [53], providing enhanced capture efficiencies and high throughputs [50]. Biomolecular protein analysis and cancer biomarker detection based on immunosensing and forest shaped single wall CNTs (SWCNTs) are shown in [54],[55], while multi-wall CNTs (MWCNTs) based sensors are demonstrated in [56]. The MWCNTs exhibits different advantages over SWCNTs such as ease of mass

production, lower cost, enhanced thermal and chemical stability [57]. Intrinsic properties of MWCNTs remain well preserved during surface functionalization as only the outer walls are exposed while inner walls remain the same, unlike in SWCNTs [57]. Surface functionalization of CNTs introduces new chemical functionalities that allow CNTs to be compatible with different applications such as organic solvent or water-solubilization, enhancement of chemical functionality, dispersion, and compatibility or lowering the toxicity of CNTs [58]. The basic idea behind the surface functionalization is to immobilize (and later release) proteins, peptides, enzymes or antigens, onto (and from) the CNTs (tips, inner and outer sidewalls) for different biological applications.

2.3 Challenges and limitations pertaining to cancer biomarker detection

After the pre-concentration and release of the biomolecular sample, detection and quantification of the desired analyte's (biomarker) presence is required on a LOC platform. Affinity-based immunoassays techniques are conventionally applied for quantitative and qualitative analysis. The analyte from the sample is captured directly over a surface (or an antibody modified surface) and then detected using an enzyme linked antibodies (e.g., ELISA) which are specific to the analyte. The procedure is simple and easy to implement and has been miniaturized for LOC applications. However, it lacks the ability to elucidate post-translational modification (PTM) of analytes especially proteins [59], which is an important aspect in avoiding false-positives in case of disease and especially cancer detection.

PTMs are chemical modifications that play a key role in functional proteomics. It increases the functional diversity of the proteome by covalent addition of functional groups or proteins, proteolytic cleavage of regulatory subunits or degradation of entire proteins. Identification and understanding of PTMs is critical in the early disease detection and prevention [60]. "Glycosylation" (Carbohydrate or glycan modification of proteins) is a type of PTM that plays an important role in the movement and recognition of cells from the immune system. It has been considered responsible for various physiological processes such as tumor

growth, cancer inflamation, infections by viral and bacterial pathogens and immunological disorders [61]. Moreover, it has also been considered as the most prevalent PTM, occurring in almost 50% of the proteins [62]. Interestingly, the biomarkers approved for clinical use for cancer detection by US - Food and Drug Administration (FDA) namely, AFP (liver cancer), CA125 and HE4 (ovarian cancer), thyroglobulin (thyroid cancer), PSA (prostate cancer), CEA (colorectal cancer), HER2/NEU, and CA15-3/CA27-29 (breast cancer) are all glycosylated [63]. These aspects have driven the interest of the scientific community towards the structural analysis of glycans (i.e., "glycoprofiling"), despite the ubiquitous nature, structural diversity and heterogeneity of the glycans [64].

Techniques such as mass spectrometry (MS), high performance liquid chromatography (HPLC), western blotting, capillary electrophoresis (CE), and fluorescence based glycan microarrays have been extensively employed for glycan profiling [65], [66]. These techniques involve labeling and subsequent release of the glycans from their core proteins, thus are time consuming, laborious, costly and complicated. To address these issues, glycan specific antibodies and glycan binding proteins (i.e., lectins) have been considered as valuable tools for glycoprofiling [67]. In particular, lectins are carbohydrate binding proteins found in many organisms from bacteria to mammals (most available lectins for research are derived from plants [64]). In 2005, a novel lectin microarray sensing technology was demonstrated for high throughput, rapid, sensitive, and low cost analysis of glycans [68]. Glycan epitopes from various samples including glycoproteins [69], cellular membranes [70], whole mammalian cells [71], pathogenic bacteria [72], and viruses [73] have been profiled using this mechanism. These works employ fluorescent labels to distinguish glycan-lectin interactions, mostly employing modified glass slides. Covalent immobilization of glycans over the lectin arrays have been achieved using surface chemistries such as NHS-esters and amines, thiols and maleimides, and amines and epoxides [64].

Controlled immobilization of biomolecules on solid surfaces is an extremely important aspect of any biological sensor design and effective realization. This area has been

undergoing extensive research owing to its importance in the biosensing platform developments for numerous diagnostic applications [74]. The biosensing surfaces are chemically modified i.e., functionalized for better control, organization, orientation, functionality, and optimization of the immobilized species [74]. Intensive efforts has been made in the recent years for the development of various immobilization techniques [75],[76]. It has been demonstrated that the retention of biological activity of the adsorbed species via selective immobilization and orientation is critical for highly selective and sensitive biomolecular and disease detection applications [77],[78],[79].

2.4 Silicon on-chip integrated optical microresonators for sensing

Silicon has been the material of choice for the advanced biosensing applications owing to the ease of lab-to-product capability and a well established manufacturing and packaging supply chain. It develops an amorphous native oxide layer upon exposure to air and moisture, and the overall surface has a dominant hydrophobic tendency [80]. This results in complexities in having uniform and homogeneous immobilization of biomolecules on silicon surface [75]. Various surface modification strategies for silicon has been described in [75],[76].

The LOC demonstrations are incomplete without incorporation of sensing transducers. Numerous transduction mechanisms such as optical, electrical, mechanical, chemical, electro-chemical, heat, and mass have been employed by the researchers for realization of ultra-sensitive biosensors [81],[82]. Recently, integrated silicon nanophotonics has enabled highly-sensitive, low-cost, compact, and densely integrated biosensing devices [83],[84], [85], [86]. In particular, different resonance-based sensing devices (resonators) have been proposed on such as microrings [87], microdisks [88],[89], microtoroids [90],[91],[92], microspheres [93], microdoughnuts [94],[95], racetrack [96], slot waveguides [97], [98], and Bragg gratings [99]. Different material platforms have been used for the realization of these resonators such as silicon [88], silicon nitride [89], silicon oxide [100], alu-

minum nitride [101], indium phosphide [102], porous silicon [103],[104], and polymers [105]. Among these device configurations and materials, integrated silicon microring resonators have gained the most interest in the optical community for biosensing applications [106],[107],[108],[109].

The silicon microring resonators are planar in configuration, operate in single radial mode (TE or TM) with high Q-factors and allow high SNRs. This allows realization of extremely dense and highly multiplexed sensor platforms with ultra-fine spectral resolutions. Moreover, the ease of fabrication of planar devices in silicon and CMOS process compatibility not only enables complete System-on-a-Package (SOP) realization for biosensing applications, but also allows much quicker lab-to-market transition of these devices. The challenge lies in the small sensing area of these resonators for analyte adsorption compared to the overall footprint. This results in small optical field overlap between the microresonator and the analyte [103], thereby resulting a in Poisson-limited sensitivity for detection of larger biomolecules [110]. Moreover, the temperature induced drifts and variations in silicon microresonators, if not properly addressed, result in inaccurate measurements [111].

Numerous works on biological sensing applications using silicon microring resonators have been reported in the literature. A silicon microring array based platform for performing rapid, multiplexed, real time binding assays has been demonstrated in [112]. This work demonstrated RIU sensitivity of 7.6×10^{-7} with sensor to sensor variability of 3.9%. Another work demonstrated growth of alternate biomolecular layers of streptavidin and biotinylated antibodies and measurement of mass of radioactively labelled protein using silicon ring resonators. LOD per unit area of $1.5 \pm 0.7 pg/mm^2$ and an absolute mass detection limit of $125ag$ is achieved [113]. Similarly, label-free quantification of cancer biomarkers (carcinoembryonic antigen CEA) in different biological solutions is demonstrated using silicon photonic microring resonators. Concentrations of CEA from 20 to $70ng/ml$ were detected in samples with respectable repeatability [84]. An extension of the mentioned work demonstrated simultaneously multiplexed quantification of five different

proteins namely prostate specific antigen (PSA), α - fetoprotein (AFP), carcinoembryonic antigen (CEA), tumor necrosis factor - α (TNF-α), and interleukin-8 (IL-8) in biological samples with clinically established detection limits, using silicon microring resonators [83]. Similarly, a sandwich assay based approach has been used to demonstrate quantitative detection of human cytokine interleukin-2 (IL-2) and temporal secretion profile of IL-2 from Jurkat T lymphocytes in serum solution with a LOD of $100pg/ml$ [85]. In these demonstrations, the devices were either commercially obtained or no information about fabrication was provided in the literature.

A detailed comparison of performance of silicon based integrated photonic resonators for biosensing applications including microdisks, microrings, and Bragg gratings has been demonstrated in [114], [115]. These works not only demonstrate the capturing of biotinylated Bovine Serum Albumin (BSA) using biotin-streptavidin chemistry, but also provide a detailed account of fabrication of the resonator devices using SOI as sample substrate, along with electron-beam (e-beam) and deep UV (λ = 193 nm) lithographic techniques. These works also demonstrate highly sensitive detection capability of the TM resonance mode compared to the TE resonance mode of the silicon microring resonators, employing a $1550nm$ laser. It has been demonstrated that the operation of these devices using $1550nm$ TM polarization light results in upto three times more sensitivity compared to operation with TE polarization light [115].

Apart from the silicon based integrated microring resonators, vertically coupled glass microring resonator with Q-factor of 12k and LOD of 1.8×10^{-5} RIU has been reported for lectin detection with excellent repeatability [116]. One of the earliest demonstrations of protein detection using silicon nitride microring resonators showed LOD of around $6.8ng/ml$ for Avidin [117]. Multiplexed detection of lectins using glycan covered silicon nitride microring resonators at visible wavelengths has been recently demonstrated [86]. Aleuria Aurantia Lectin (AAL) and Sambucus Nigra Lectin (SNA) were detected with LOD of $2 \times 10^{-6} RIU$ and surface absorbed mass of $1pg/mm^2$ [86]. A similar demon-

stration has been shown for the detection of Cholera Toxin Subunit B (CTB) using glycan coated silicon nitride microring resonator platform [118]. Polymer based microring resonators have also been employed for biomolecular sensing applications. Detection of Glucouse, Biotin, Biotin-BSA and Streptavdin has been demonstrated with Q-factors of 20k and mass LOD reaching $250pg/mm^2$ [119]. Glucose sensing has been demonstrated using SU-8 based microring resonators with a sensitivity of $115 \pm 8nm/RIU$ and a Q-factor of 1.5×10^4 [120].

In the design of high-Q resonators, the coupling between the resonators and the common waveguide is a design challenge faced by the researchers. The coupling gap is optimized by adjusting the gap between the waveguide and the microresonator to achieve a close to critical coupling regime, which maximizes the device sensitivity [121]. The critical coupling has been preferred between the microring resonators and the input waveguide as it allows maximum extinction ratio and higher SNR for the detection of resonance wavelength shifts for sensing purposes [86]. It has been observed and demonstrated that reducing the resonator width extends the resonator mode energy outwards, exponentially enhancing the field overlap between the resonator and the input waveguide [121]. This not only enhances the coupling between the resonator and the input waveguide, but also results in enhanced light matter interactions favorable for highly sensitive sensing applications [122]. Moreover, for highly sensitive sensing applications, single mode operation is desired to avoid spectral overlap with other polarization modes that are allowed in the waveguide and can couple with the resonators [103].

The temperature induced resonance variations is another challenge encountered in the design of silicon optical microresonators [111]. The temperature can be actively controlled, stabilized, and compensated using expensive temperature stabilizing equipment, which adds to the cost and size of the equipment [111]. The temperature variations can be compensated in planar optical sensors using athermal design of core and cladding i.e., using materials with thermo-optic (TO) constants having opposite signs. This limits the options

for sensing platforms as limited number of such material combinations are available, especially in case of sensor platforms for biosensing applications [111]. Another mechanism is to use on-chip reference resonators.

Another challenge in silicon nanophotonics lies in lighting up these microresonator devices i.e., coupling light in these integrated on-chip optical platforms to generate enhanced light-matter interaction for advanced biosensing applications. Conventional coupling techniques such as prism based coupling [123] and end-fire coupling [124],[125] are prone to misalignment, have complex operating mechanism [124], require extended fiber tapering [124], and are polarization insensitive [124] especially when employed for exciting on-chip nanophotonic components. To address these challenges, on-chip grating couplers are realized which allow relaxed fiber-coupler alignment, decreased CMOS real-estate, polarization dependent operation, and ease of fabrication [124],[126]. The grating couplers enable vertical coupling capability, allowing flexibility in placement of different optical components on the chip [124],[126]. These couplers also increase the density of the on-chip optical interfaces and free the edges of the chip for realization of different on-chip electrical and optical features [126]. Moreover, these couplers are CMOS compatible and enable ease of wafer-scale testing of the fabricated devices thus, decreases the overall packaging cost and allow complete system-on-package (SOP) realization.

Key challenges in the grating coupler design includes back reflection, fiber-coupler mode matching, directionality, and coupler coupling efficiency. Several designs of high efficiency grating couplers have been presented in the literature to address these issues. These include fabrication of apodized grating [127], sub-wavelength gratings [128], partially etched grating [129], and anti-reflection mirrors [130]. These modifications result in exhaustive simulations and design optimizations, increased fabrication complexity, and overall cost of the devices. Moreover, the literature is more focused towards design of TE polarized input/output (I/O) grating couplers for high performance communication and optical computing applications where coupling efficiency is an important aspect, while less

attention has been given to TM polarized I/O grating (highly evanescent nature of TM polarized light results in higher losses) [115]. In the realm of biosensing applications, the aspect of coupling efficiency is relaxed compared to the high performance on-chip optical communication and computing applications [108],[131]. However, the overall cost of the device is of key importance for the realization of disposable point-of-care (POC) on-chip optical biosensing platforms.

CHAPTER 3
FABRICATION OF MICROFLUIDIC DEVICES

3.1 Introduction

Polydimethylsiloxane (PDMS) has been one of the most extensively used silicon-based organic polymer for microfluidic applications. Its advantages of include ease of device fabrication (unusual rheological (or flow) properties), biocompatibility, optically transparent, inert, non-toxic, non-flammable, low shrinkage, and low cost [132]. Numerous works have been reported in the literature employing PDMS for microfluidic device fabrications [133],[134],[135]. The fabrication process flow seems to be a simple affair as a huge majority of works report similar fabrication methodologies. However, to achieve good repeatable results, a number of modifications and optimizations have to be considered during fabrication.

SU8 is a viscous, epoxy-based negative photoresist which has been originally developed as a photoresist for the microelectronics industry to provide a high-resolution mask for the fabrication of the semiconductor devices [136]. It is now primarily employed in the fabrication process of microfluidic devices using the soft-lithography process [35], nanoimprint lithography [137], and microelectromechanical devices [138].

In this chapter, I have presented a detailed process flow, associated challenges, and remedies for the microfluidic device fabrications employing the widely employed soft lithography technique.

3.2 Fabrication of master molds

3.2.1 Printed Circuit Board (PCB) milling process

A printed circuit board (PCB) milling process is a process of removing areas of copper from a sheet of PCB material to recreate the desired planar layout pattern such as signal traces, vias, microwave and millimeter devices, etc. This process can also be used to generate master molds for fabrication of microfluidic devices. I have used Rogers RO 4003C boards with $17\mu m$ and $35\mu m$ electrodepsosited copper for the fabrication of master molds. LPKF rapid prototyping machine has been used for the PCB milling process, while the devices layouts has been made using EagleCAD software. Figure 3.1 (a) shows the fabricated microfluidic devices using the PCB board milling process.

The minimum feature size realizable in the XY direction is 8 to 10 mils (i.e., $\sim 200\mu m$) while the Z direction is limited by the available copper thickness (i.e., $17\mu m$ and $35\mu m$). This renders the technique less suitable for a wide range of microfluidic applications, especially where extremely small feature sizes and volumes are required. The overall performance of the PCB board based master molds when compared with the durability, robustness, reusability, and repeatablity of other lithography based techniques, is far better.

3.2.2 SU8 polymer based master molds

I employed the conventional soft-lithography process for the fabrication of microfluidic devices. I have used SU8 epoxy-based negative photoresists i.e., SU8-2015, SU8-2035, and SU8-2050, along with both glass and silicon as carrier substrates for the fabrication of the master molds. I have used SU8 to a thickness of $15\mu m$, $35\mu m$, and $50\mu m$ using SU8-2015, SU8-2035, and SU8-2050 for the fabrication of the microfluidic devices, respectively. I have used AutoCAD software for the microfluidic device layout/pattern design. I have the layouts printed over the transparency sheets (prints obtained from CAD/Art Services, US) to be utilized as an optical mask. The minimum critical dimension of the transparency

mask is $10\mu m$.

Optical lithography based fabrication

The SU8 photoresist is spin coated over the silicon/glass to achieve a uniform desired thickness. The spin coated wafer is then soft baked and cooled down. The device layout pattern is then defined by exposing the SU8 in the MA-6 mask aligner setup using UV light (i-line, $\lambda = 365nm$). The transparency sheets are utilized as optical masks for defining the desired microfluidic device features. A post exposure bake is then performed, followed by the development of the wafer using the SU8 developer. The developed wafer is then washed using IPA, dried using nitrogen gas, and inspected using a microscope and a profilometer.

Maskless lithography based fabrication

The SU8 photoresist is spin coated over the silicon/glass to achieve a uniform desired thickness. The spin coated wafer is then soft baked and cooled down. The device layout pattern is then defined by exposing the SU8 in the Heidelberg MLA-150 maskless aligner setup using the $\lambda = 365nm$ laser. A post exposure bake is then performed, followed by the development of the wafer using the SU8 developer. The developed wafer is then washed using IPA, dried using nitrogen gas, and inspected using a microscope and a profilometer.

***Note:** The MLA-150 setup is a direct laser writing setup and requires no optical masks for the exposure. Moreover, the minimum feature size that can be realized using this setup is $\sim 1\mu m$. This results in improved device features and an overall decrease in cost of fabrication.

The figure 3.1 shows three different types of master molds fabricated for microfluidic device realizations, (a) PCB milling process, (b) SU8 over glass, and (c) SU8 over Silicon.

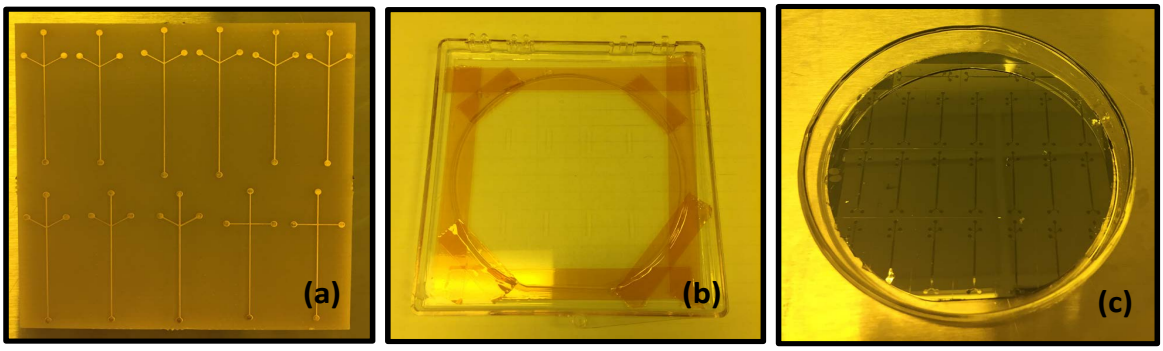

Figure 3.1: The figure shows three different types of master molds fabricated for microfluidic device realizations. (a) PCB milling process, (b) SU8 over glass, and (c) SU8 over silicon.

Table 3.1: SU8 processing details for master mold fabrication

SU8 Type	**Spin Details**		**Soft Bake Time (sec)**		**Thickness** (μm)	**Post Exposure Bake**		**Development Time (min)**	**Hard Bake Time (min)**
	Speed (rpm)	**Time (sec)**	**60°C**	**90°C**		**60°C**	**90°C**		
2015	3000	30	3	5	15	3	5	5	60
2035	1650	30	6	9	50	6	9	10	60
2035	3000	35	5	7	35	5	7	6	60
2050	3000	30	6	9	50	6	9	10	60

3.3 SU8 Recipes

The table 3.1 shows the details of the recipes used for fabrication of SU8-based master molds for microfluidic device fabrications. Three different SU8 photoresists from SU8 2000 series has been utilized for the fabrication of the devices.

The table 3.2 shows the comparison between the recipes for processing of SU8 photoresist for the fabrication of microfluidic devices using the conventional mask aligner setups and the recently introduced Heidelberg MLA-150 maskless aligner system for advanced lithography applications.

Table 3.2: Exposure details for SU8 processing using MLA-150 maskless aligner and MA-6 mask aligner setups. The UV-lamp (i-line, $\lambda = 365nm$) intensity is $10mW/cm^2$.

SU8 Type	**Thickness** (μm)	**Exposure Dose** (mJ/cm^2)		**Exposure Time (min) (for 4' wafer exposure)**	
		MLA - 150	**MA - 6**	**MLA - 150**	**MA - 6**
2015	15	500	120	26	0.2
2035	35	525	160	38	0.266
2035	50	550	180	45	0.3
2050	50	550	200	45	0.3333

3.4 Silanization of the master mold

Thermal curing of the PDMS results in its sticking to the silicon or glass substrate of the master molds. In order to avoid the sticking, silanization of the molds is performed. I have utilized (3-Mercaptopropyl)trimethoxysilane for the silanization of SU8-based master molds and employed the chemical vapor deposition (CVD) mechanism to silanize the master molds. $1ml$ of the silane solution is pipetted out in a disposable aluminum dish and placed in the vacuum desiccator chamber with the SU8-based master molds for 12 hours. After 12 hours, the molds are taken out and baked in oven for 15 minutes at 100°C to have a uniform layer of silane. The figure 3.2 shows SU8-based master molds on silicon and glass wafers, inside a customized vacuum desiccator chamber for chemical vapor deposition (CVD) based silanization.

3.5 Preparing PDMS for microfluidic devices

Sylgard 184 from Dow Corning Corporation is the most widely used version of the PDMS polymer especially in the United States. The Sylgard 184 elastomer is a polymer base that comes with a curing agent in a form of a kit, especially tailored for microfluidic applications. The Sylgard 184 elastomer base and the curing agent are added together and thoroughly mixed in 10:1 (weight ratio), respectively, to form the PDMS polymer that is later used for microfluidic device fabrications. The figure 3.3 shows the Sylgard 184 base,

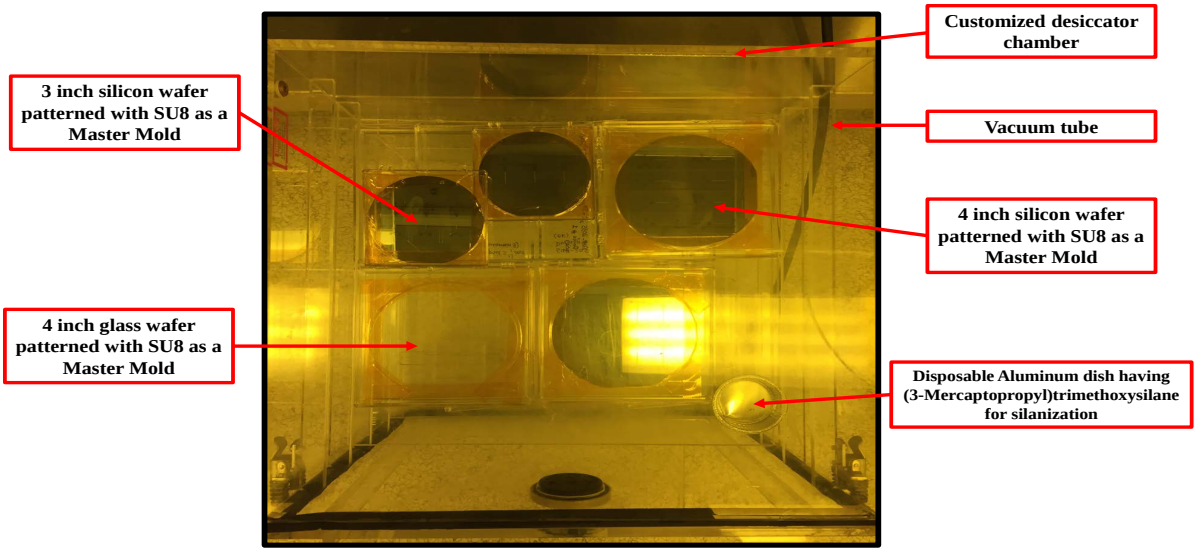

Figure 3.2: The figure shows SU8-based master molds on silicon and glass wafers, inside a customized vacuum desiccator chamber for chemical vapor deposition (CVD) based silanization.

curing agent, and a container having both of them mixed together in a ratio mentioned earlier.

3.6 Degassing, casting, and curing of PDMS

Microfluidic device fabrication involves casting of the prepared PDMS over the master mold (placed in heat tolerant container), followed by a thermal curing step. It has been observed that during the mixing of the Sylgard base and the curing agent, bubbles are formed in the PDMS. These bubbles should be removed to have a clear, transparent, and conformal casting of PDMS over the master mold. One of the most commonly employed mechanism to remove the air bubbles is to use a vacuum desiccator. The PDMS is poured over the master mold and is then placed in the desiccator under vacuum to remove the trapped air bubbles. Another mechanism involves rigorous mixing of the PDMS mixture till the air bubbles are removed, while some methods involves leaving the mixture for a few hours till a clear transparent PDMS mixture has been obtained. However, the biggest challenge with

Figure 3.3: The figure shows (a) Sylgard 184 elastomer base, (b) curing agent, and (c) elastomer base and curing agent mixed together in 10:1 (weight ratio), respectively

these mechanisms is the time involved in preparing the desired PDMS sample. Although, the vacuum desiccator methods works appreciably well for most of the applications, it lacks consistency when replication of high aspect ratio structures is desired. In such structures, the air bubbles get trapped in the features and are extremely difficult to be removed using the vacuum desiccator. Moreover, these trapped bubbles rises to the surface during the thermal curing process, thus spoiling the sample. It has been observed that longer desiccator times and through mixing of the solution has resulted in better and repeatable results, but at the expense of longer processing durations. In my work, I have designed PDMS micropillar structures with aspect ratio reaching maximum upto 1:2.5, and have faced similar challenge for these structures. The figure 3.4 shows the appearance of the trapped air bubbles in the thermally cured PDMS, thoroughly mixed, and degassed for 6 hours using vacuum desiccator.

To address this degassing challenge, I completely removed the air bubbles from the PDMS before pouring it over the master mold. I poured the initially mixed PDMS (having air bubbles in it) into a $50ml$ conical centrifuge tubes and employed a high speed centrifuge

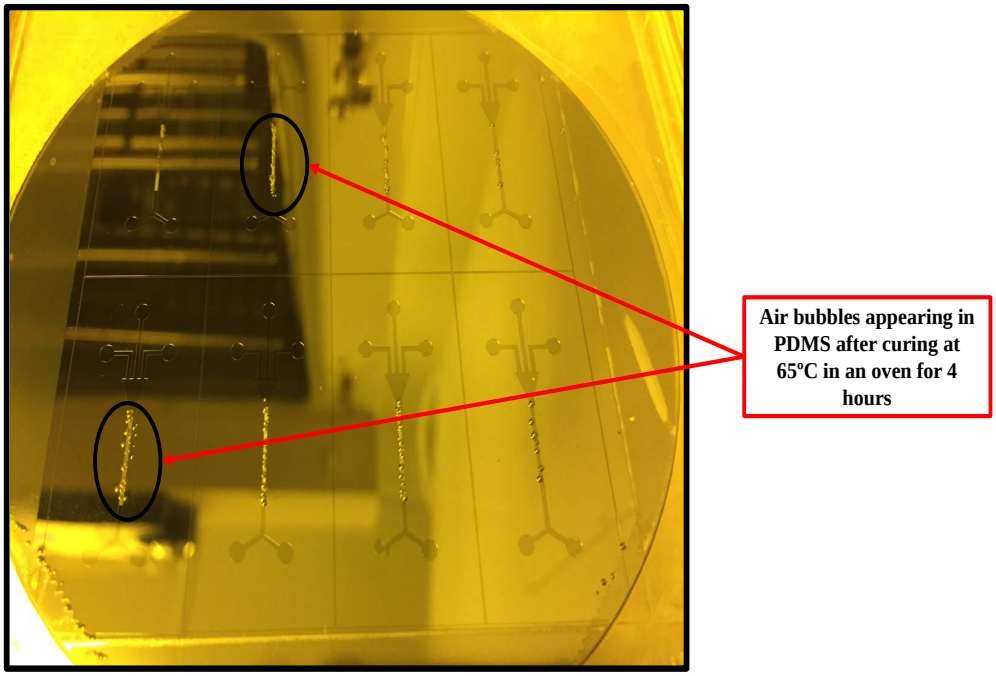

Figure 3.4: The figure shows trapped air bubbles in thermally cured PDMS, thoroughly mixed, and degassed using vacuum desiccator for 6 hours while replication of high aspect ratio structures

device at $3000rpm$ with $2500g$ for 30 seconds. Clear PDMS mixture has been obtained and is then poured over the master mold for device casting. It should be noted that the degassed PDMS should be poured over the mold as soon as possible to avoid hardening of the PDMS. The figure 3.5 (a) shows the PDMS mixture after initial mixing of the Sylgard base and the curing agent, (b) shows the $50ml$ conical centrifuge tubes placed in the centrifuge device, (c) shows the clear PDMS solution (no air bubbles) obtained after centrifuging 30 seconds, and (d) shows the setting of the centrifuge device.

Once the degassed PDMS is poured over the mold, it is then placed in a vacuum desiccator for 30 to 60 minutes to remove the remaining trapped air bubbles (the desiccation time depends upon the size of the sample and the available strength of the vacuum). Once a clear PDMS sample over the mold has been obtained, it is then placed in a oven at $65°$C for 6 to 8 hours for the thermal curing. The cured PDMS is then stripped off the master mold

using a razor blade. A transparent tape is used to cover the device side and punch through holes are made using a biopsy punch for the fluid inlet and outlets. The figure 3.6 shows thermally cured PDMS (without any air bubbles) after 6 hours of thermal curing at $65°C$ in a vacuum oven. The PDMS is ready to be stripped-off for bonding with glass or silicon substrate for device realization.

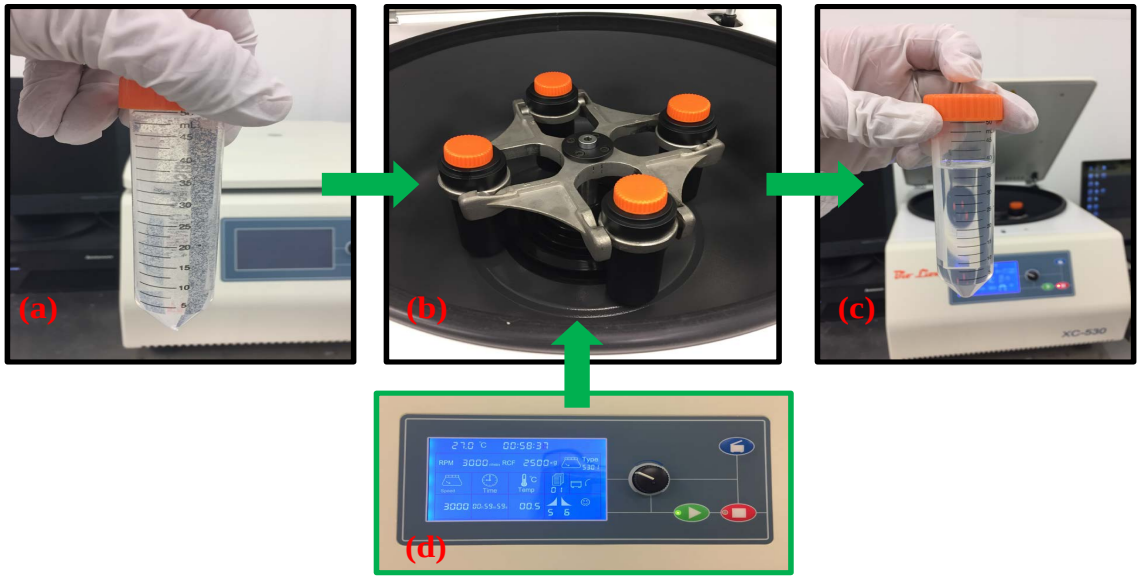

Figure 3.5: The figure shows (a) the PDMS mixture after initial mixing of the Sylgard base and the curing agent, (b) shows the 50ml conical centrifuge tubes placed in the centrifuge device, (c) shows the clear PDMS solution (no air bubbles) obtained after centrifuging 30 seconds, and (d) shows the setting of the centrifuge device

3.7 Bonding, Interfacing, and Integration of PDMS

The PDMS is strongly hydrophobic in nature. This property does not allow it to stick to any surface easily. To bind the PDMS to the glass (silicon oxide) and silicon surfaces, the most commonly used mechanism is to expose the PDMS mold and the substrates (i.e., Glass, Silicon) to oxygen plasma for 10 to 15 minutes. This mechanism increases the hydrophilicity of the surfaces by activating the -OH radicals on the surfaces. The surfaces are then pressed together after the exposure to facilitate bonding. It should be noted that the surfaces should be pressed together immediately after the plasma treatment. A drop of

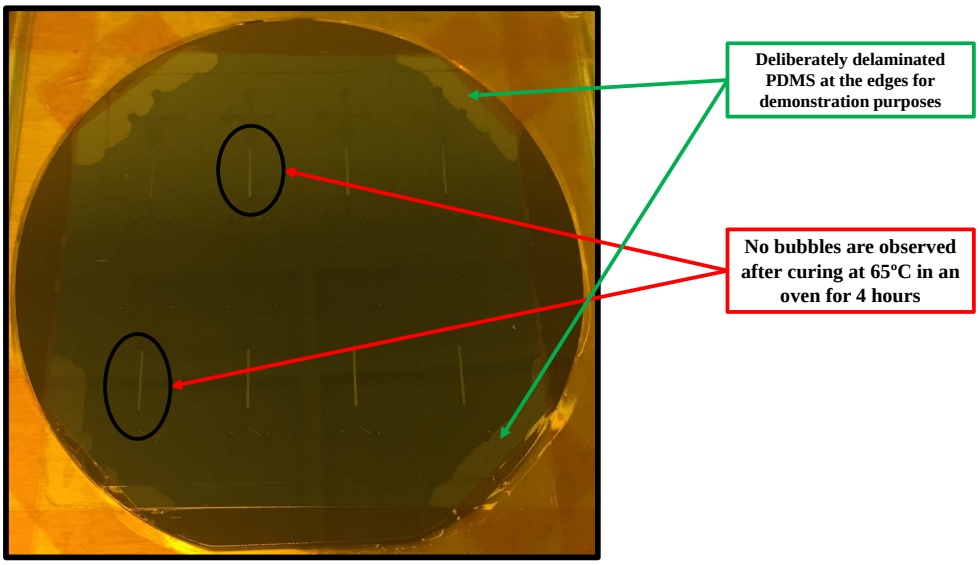

Figure 3.6: The figure shows thermally cured PDMS (without any air bubbles) after 6 hours of thermal curing at $65°C$ in a vacuum oven. The PDMS is ready to be stripped-off for bonding with glass or Silicon substrate for device realization.

methanol or water can be used between the surfaces, along with a microscope to aid for alignment.

In my work, I utilized an Ultra-Violet Ozone Cleaning System (UVOCS) for generating the -OH radicals on the surfaces to facilitate the bonding. The PDMS surface, glass slides, and silicon samples are treated in the UVOCS system for 15 minutes. A droplet of water (or methanol) is then placed on the treated surfaces followed by immediate pressing of them against the other (i.e., PDMS with glass or PDMS with silicon). The pressed surface are then baked on a hotplate for 30 minutes at $90°$C to have a complete bonding.

Once the bonding process is complete, I connected the inlet and outlet tubing to the respective punch through holes in the bonded devices. I have used $1ml$ syringes and Harvard PHD 2000 infusion flow pump for flowing my samples into the microfluidic devices. The flow rates have been adjusted with the flow pump. It should be noted that the flow rates can be adjusted by varying the size (diameter) of the syringes. The flow pump also contains an

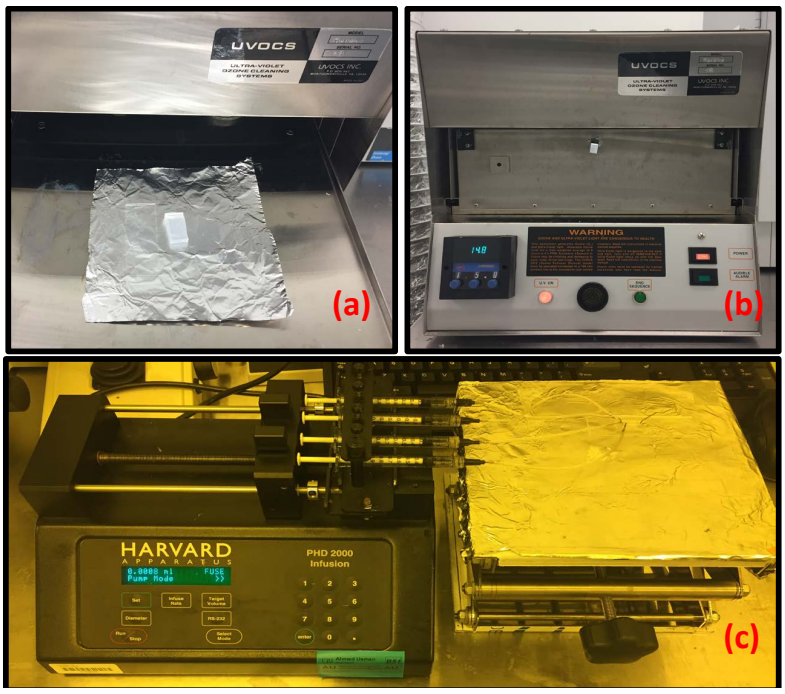

Figure 3.7: The figure shows (a) a glass slide and PDMS device placed in a UVOCS system for activation before bonding, (b) an operating UVOCS system (set for 15 minute exposure), and (c) a complete microfluidic device setup with a PDMS device bonded to a glass slide having its inlets connected to a Harvard 2000 infusion pump and outlets for waste sample

in-built directory for flow rate variation for various syringe sizes. This allows the user to adjust the flow rate accordingly. I have varied the flow rates from $0.1\mu l/min$ to $35\mu l/min$ for testing the bonding strength of the devices. The devices worked perfectly fine without any leakage or delamination of the devices.

The figure 3.7 shows (a) a glass slide and PDMS device placed in a UVOCS system for activation before bonding, (b) an operating UVOCS system (set for 15 minute exposure), and (c) a complete microfluidic device setup with a PDMS device bonded to a glass slide having its inlets connected to a Harvard PHD 2000 infusion pump and outlets for waste sample.

CHAPTER 4

SURFACE MODIFICATIONS AND SURFACE CHEMISTRY

4.1 Introduction

Controlled immobilization of biomolecules such as proteins, DNA, RNA, lipids, bacteria, and biomarkers, on solid surfaces has been an extensive subject of research owing to its importance in the biosensing platform developments for different disease diagnostics [74]. The biosensing surfaces are chemically modified i.e., functionalized for better control, organization, orientation, functionality, and optimization of the immobilized species [74]. Intensive efforts have been made in the recent years for the development of various immobilization techniques [75],[76]. It has been demonstrated that the retention of biological activity of the adsorbed species via selective immobilization and orientation is critical for highly selective and sensitive biomolecular and disease detection applications [77],[78],[79].

Silicon has been the material of choice for the advanced biosensing applications owing to the ease of lab-to-product capability and a well established manufacturing and packaging supply chain. Silicon develops an amorphous native oxide layer upon exposure to air and moisture, and the overall surface has a dominant hydrophobic tendency [80]. This results in non-uniform and in-homogeneous immobilization of biomolecules on silicon surface [75],[76].

Glass (i.e., silicon oxide) has also been extensively employed for various biomolecular diagnostic applications. It has been widely used for the development of microchips, microarrays, biochips, and microfluidic devices [139],[140]. Glass, as a material is biocompatible, rigid, flat, nonporous, easy to handle, extremely cheap, has a wide spread supply chain, provides low native fluorescence, is resistant to high temperatures and organic sol-

vents, transparent in nature, and provides a hydrophobic surface which is highly amenable to surface modifications [76]. Numerous surface modifications techniques for glass has been presented in the literature [76],[141].

Polydimethylsiloxane (PDMS) is one of the most commonly used material for microfluidic applications [34]. It is a biocompatible, transparent, and soft rubber-like polymer which can be easily patterned using the well-established soft lithography fabrication techniques [35]. It enables the current microfluidic platforms to have efficient fluid handling capability, fluid processing, and also allows small volumes of reagents to be used on-chip to perform rapid, low-cost, quantitative and clinical analysis involving different types of proteins and biomarkers for various on-chip diagnostic applications. One of the key advantages of PDMS enhanced microfluidic technologies is the ability to detect extremely low concentrations from small sample volumes (e.g., upto attomolar) [36].

Carbon nanotubes (CNTs) presents with high surface ratios and chemical stability, indicating their promise as ideal scaffolds for immobilization of biomolecules [142], [143]. SWCNTs and MWCNTs can be easily functionalized and are extensively utilized for homogeneous bioassays. Moreover, their compatibility with the nanofabrication processes allows them to be employed as building blocks for the next generation of micro and nano sensing platforms for POC sensing applications [56]. Some of the recent advances in CNT based immunosensors has been presented in [144].

In this chapter, I present detailed analysis for the surface modifications of silicon, glass, PDMS, and MWCNT samples for biomolecular immobilization applications.

4.2 Chemicals and Materials

The silane reagents (3-aminopropyl) triethoxysilane (APTES) and (3-Glycidyloxypropyl) trimethoxysilane (GPTMS or GLYMO), and Anhydrous 2-Propanol solution ($\geq 99\%$ pure) has been obtained from Sigma-Aldrich. Avidin (egg white) and Phosphate Buffer Saline (1X-PBS, pH 7.4) has been purchased from Thermofisher Scientific, US. ATTO - 520 fluo-

rescence tagged biotin has been purchased from Sigma-Aldrich. N-Hydroxysuccinimide (NHS), N-(3-Dimethylaminopropyl)-N-ethylcarbodiimide hydrochloride (EDC), Bovine Serum Albumin (BSA), and Tween 20 has been purchased from Sigma-Aldrich. Rabbit IgG serum (produced from rabbit serum, lyophilized powder) and FITC tagged anti-IgG secondary antibodies (anti-rabbit IgGs produced in goat) has been purchased from Sigma-Aldrich, US. SU-8 2015 and SU8 developer has been purchased from MicroChem, US. Sylgard 184 (PDMS by Dow Corning Corporation) and the curing agent has been purchased from Ellsworth Adhesives, US. Silicon and fused silica glass wafers has been procured from WaferPro, US. All other equipment and cleaning solutions has been provided at the IEN cleanroom utilities present at the Georgia Institute of Technology, Atlanta, US.

4.3 Sample Preparation

4.3.1 Silicon and Glass Sample

The 4 inch silicon and glass wafers have been diced into 1cm by 1cm sample using the ADT 7100 Dicing Saw. The diced samples are copiously cleaned using acetone, methanol, and DI-water. The samples are then dried using nitrogen gas, followed by Piranha (4:1 of H_2SO_4:H_2O_2) cleaning at 80°C for 30 minutes. The cleaned samples are again dried using the nitrogen gas and placed in the UV-Ozone Cleaning System (UVOCS) for 15 minutes. The UVOCS cleaning mechanism controls the hydrophilicity of the samples by generating the -OH bonds at the surface. The samples are then rinsed with DI-water, dried using nitrogen gas, and placed over the hotplate at 110°C for 5 minutes to completely remove any moisture content. The dehydration baking step is extremely important as the silane reagents reacts with the moisture (water) and hydrolyze over the sample resulting in the loss of reactivity [145].

4.3.2 PDMS Sample

Sylgard 184 base and the curing agent are thoroughly mixed in 10:1 (volume ratio). The mixture is then poured in a plastic petri dish and degassed using vacuum desiccator for 6 hours. Once degassed, the PDMS is placed in an oven at 65°C for 4 hours for curing. The cured PDMS mold is peeled off the petri dish and cut into small pieces using a razor blade. It is then cleaned using IPA and dried using nitrogen gas. The PDMS samples are then immersed in 5:1:1 solution of $H_2O : HCl : H_2O_2$ for 15 minutes at 70°C. The samples are then taken out, washed using DI-water, and dried using nitrogen gas. The dried samples are then cured at 100°C for 10 minutes using a hotplate. The cured samples are then placed in UVOCS system for 15 minutes. This process oxidizes the PDMS generating Si-OH bonds at the surface [146]. The process has also shown compatibility with PDMS bonded on silicon and glass substrates at room temperature.

4.3.3 MWCNTs Sample

The 4 inch silicon has been diced into 1cm by 1cm sample using the ADT 7100 Dicing Saw. The diced silicon samples are copiously cleaned using acetone, methanol, and DI-water. The samples are then dried using nitrogen gas, followed by Piranha (4:1 of H_2SO_4:H_2O_2) cleaning at 80°C for 30 minutes. A $200nm$ layer of silicon oxide SiO_2 is deposited over the clean and dried silicon sample, followed by evaporation of $10nm$ of Aluminum oxide (Al_2O_3) and $1.1nm$ of Iron (Fe) catalyst layers, using the e-beam evaporator tool (Denton e-beam evaporator). The SiO_2 layer acts as an insulation layer and also allows adhesion of the Al_2O_3 to silicon sample surface. The Fe acts as a catalyst by forming nanoparticle enhanced nano-islands at high temperatures over the porous Al_2O_3, for the growth of vertically aligned MWCNTs [142].

The MWCNTs has been grown using the root growth mechanism, employing the low pressure chemical vapor deposition (LPCVD) process in the Axitron Black Magic reactor [147]. Acetylene (C_2H_2) gas has been used as a precursor, in the presence of nitrogen

(N_2) and hydrogen (H_2) gas. The N_2 and H_2 are maintained in the chamber at a flow rate of $1000sccm$ and $100sccm$, respectively, while the temperature of the reactor has been gradually increased. The C_2H_2 gas is allowed to flow in the reactor at $820°C$ at a pressure of $720mbar$, having a flow rate of $160sccm$. The mixture of gases is then maintained for the growth duration. Finally, the C_2H_2 and H_2 gases are discontinued, while the N_2 gas is flown for 5 to 10 minutes to gradually cool the reactor and displace the remaining gases in the reactor. The samples are then removed from the chamber and inspected using SEM for the MWCNT forest growth.

4.4 Silanization

The most commonly utilized surface modification technique is the use of organo-functional "alkoxysilanes" as a coupling agent for immobilization of the organic molecules to the silicon, glass, PDMS, and MWCNT surfaces. Theses silanes are deposited over the samples such as silicon or glass, in the form of thin layers using different mechanisms such as immersion coating [148], drop casting [149], spin coating [76], and chemical vapor deposition [150]. Silane solutions are employed for these mechanisms, which are prepared by dissolving the silanes in the silane coupling reagents such as aqueous solvents [151],[152], organic solvents [153],[154], and in some cases a mixture of aqueous/organic solvents and water [103].

The (3-Aminopropyl) triethoxysilane (APTES) is the most commonly utilized organo-functional alkoxysilane for surface (Silicon, Glass, PDMS, MWCNTs) modifications. The surface modification process involves formation of covalent Si-O-Si bonds formation between the silanol groups (present on the oxidized silicon surface) and the hydrolyzed organo-silane molecules, resulting in an amine-terminated ($-NH_2$) film over the silicon surface [155]. The presence of amine i.e., $-NH_2$ groups on the surface allows proteins or other biomolecules to be immobilized in a simple manner. Similarly, another organo-alkyoxysilane known as (3-Glycidyloxypropyl) trimethoxysilane (GPTMS, GPTS,

or GLYMO) has also been used for surface modifications. This silane results in similar Si-O-Si bond formation but resulting in epoxide (i.e., epoxy group) terminated film over the sample surface [156],[157].

One of major problems associated with organo-functional alkyoxysilane based silanization is the co-polymerization in the presence of traces of water, forming aggregates and disordered mulitlayer layers on the substrate [155]. In the absence of moisture(or low water content), grafting could occur owing to the direct nucleophilic attack of the surface groups (silanols) on the silane molecules [155]. It has been observed that the use of organic solvents for the preparation of the silane solutions helps in reducing the formation of the inhomogeneous, unstable, and disordered multilayers [145],[158]. Moreover, the intermediary hydrolysis can be controlled by activating the -OH radicals on the surface of the silicon sample before immersion in the silane solutions [76],[159]. There are various other factors that affect the silanization process such as the concentration of the silane [148],[160], silanization time [161], moisture (humidity) [155], curing temperature [154], temperature and volume of the solution [162], size and pressure of immersion chamber [150].

It has been observed that the immersion based silanization process is extensively employed by the researchers to generate silane functionalized samples. The repeatability of the process is another challenge, especially when generating monolayer thickness [154],[161]. The thickness of silanization layer plays a key role in sensitivity and molecular immobilization efficiency for biosensor [78],[116],[163], and hence repeatable control over the silanization thickness and density (i.e., monolayer deposition of APTES or GPTMS) is extremely important [148].

I present an optimized silanization protocol for the generation of amine terminated (using APTES silane) surfaces over the silicon, glass, PDMS, and MWCNT samples, and epoxy terminated (using GPTMS silane) surfaces over the silicon, glass, and PDMS samples.

4.4.1 Silanization Techniques

(1) Spin coating of silanes

Three different solutions for APTES and GMPTS have been prepared with concentrations of 1%, 5%, and 10% (v/v), using anhydrous 2-Propanol solvent (anhydrous Ethanol, anhydrous Methanol, and Toluene can also be used). The solutions are properly mixed together using a vortexer (Thermo Scientific) at 1500rpm for 30 seconds. The SCS G3P8 spin coater setup has been used to spin coat the prepared solutions over the cleaned and dehydrated silicon and glass samples. The samples are placed in the setup and three drops of the solution are dropped over them using a pipette. Four different spin speeds i.e., 2000rpm, 2500rpm, 3000rpm, and 4000rpm are utilized to evaluate the silanization performance. Each sample has been spinned for 30 seconds. Once the spin coating is complete, the samples are rinsed with 2-Propanol and baked for 100°C for 15 minutes over a hotplate to achieve uniform immobilization of APTES or GMPTS over the sample surface. Tables 4.1 and 4.2 shows the variation of the thickness of APTES silane and GMPTS silane (in 2-Propanol) over silicon samples for different spin speeds, respectively.

(2) Immersion based coating of silanes

After preparation and hydrophilization of the samples, the samples are immersed in 1%, 5%, 10% solution (v/v) of APTES and GMPTS in anhydrous 2-Propanol for 15 minutes, 30 minutes, 1 hour, and 2 hours. After the desired time, the samples are taken out, rinsed with anhydrous 2-Propanol, and dried using nitrogen gas. The dried samples are then cured for 15 minutes at 100°C on a hotplate for 15 minutes to achieve uniform immobilization of APTES or GMPTS over the sample surface. Tables 4.3 and 4.4 shows the variation of the thickness of APTES silane and GMPTS silane over the silicon samples for different immersion times, respectively.

Table 4.1: Variation of thickness of APTES silane (in 2-Propanol) over silicon samples for different spin speeds

Spin Speed (rpm)	**Thickness of silane over silicon sample (nm)**		
	1% APTES	**5% APTES**	**10% APTES**
2000	80.72	102.45	112.15
2500	53.56	83.62	104.83
3000	31.27	57.89	82.01
4000	18.17	37.51	54.46

Table 4.2: Variation of thickness of GMPTS silane (in 2-Propanol) over silicon samples for different spin speeds

Spin Speed (rpm)	**Thickness of silane over silicon sample (nm)**		
	1% GMPTS	**5% GMPTS**	**10% GMPTS**
2000	1.74	2.79	3.57
2500	1.53	2.58	3.25
3000	1.41	2.43	3.08
4000	1.36	2.25	2.94

4.4.2 Silanization of Silicon Sample

The silicon samples have been silanized with APTES and GMPTS using both of the above mentioned silanization techniques. The attachment of silanes over the samples has been been monitored using the ellipsometery, FTIR, and XPS characterization techniques (details of the techniques explained earlier).

4.4.3 Silanization of Glass Sample

The glass samples have been silanized with APTES and GMPTS using both of the above mentioned silanization techniques. The attachment of silanes over the glass samples has been been monitored using the ellipsometery, FTIR, and XPS characterization techniques.

Table 4.3: Variation of thickness of APTES silane (in 2-Propanol) over silicon samples for different immersion times

Immersion Time (minutes)	**Thickness of silane over silicon sample (nm)**		
	1% APTES	**5% APTES**	**10% APTES**
15	14.27	42.71	68.16
30	70.82	123.14	183.49
60	132.75	207.42	287.31

Table 4.4: Variation of thickness of GMPTS silane (in 2-Propanol) over silicon samples for different immersion times

Immersion Time (minutes)	**Thickness of silane over silicon sample (nm)**		
	1% GMPTS	**5% GMPTS**	**10% GMPTS**
15	1.57	2.43	2.97
30	2.17	3.27	4.32
60	2.57	4.15	5.86

4.4.4 Silanization of PDMS Sample

The PDMS samples have been silanized with APTES and GMPTS using the immersion based silanization technique. The attachment of silanes over the PDMS samples has been been monitored using the FTIR and XPS characterization techniques.

4.4.5 Silanization of MWCNT Sample

The MWCNT samples have been silanized with APTES and GMPTS using the immersion-based silanization techniques. The attachment of silanes over the samples has been been monitored using the FTIR and XPS characterization techniques.

4.5 Glutaraldehyde based modification of silanized samples

A solution of 2.5% glutaraldehyde (GA) in 1X-PBS (v/v) has been prepared. The silanized samples of silicon, glass, PDMS, and MWCNTs are immersed in the glutaraldehyde solu-

tion for 30 minutes at room temperature in separate petri dishes using 5 to $10ml$ of solution for each sample. The samples are then taken out, rinsed using 1X-PBS solution, dried using nitrogen gas, and then characterized using FTIR and XPS characterization techniques.

4.6 Biomolecular immobilization over the samples

Numerous biomolecular immobilization protocols have been presented in the literature [76]. I investigated two different protocols for generating the Avidin functionalized surfaces over the APTES silanized samples.

4.6.1 Avidin immobilization over APTES modified surfaces

The first protocol involves activation of the silanized surfaces using the EDC/NHS protocol, resulting in a carbodiimide/ester functionalized surface [76]. The second protocol involves functionalization of the silainized surfaces with glutaraldehyde (GA) to form aldehyde-functionalized surfaces [76]. A $100\mu g/ml$ of Avidin solution in 1X-PBS has been used for the analysis.

Protocol (1) - Carbodiimide/Ester functionalized surface

Avidin solution is mixed with 0.04M N-Hydroxysuccinimide (NHS) and 0.06M N-(3-Dimethylaminopropyl)-N-ethylcarbodiimide hydrochloride (EDC) in 1X-PBS (or MES buffer (pH 5.3)). The APTES coated samples are then incubated in the solution having Avidin at room temperature for 1 hour to have a uniform Avidin adsorption over the surface. The samples are then rinsed using 1X-PBS solution to remove the unattached Avidin, dried using nitrogen gas, and taken for characterization.

Protocol (2) - Aldehyde-functionalized surface

The GA-APTES modified samples are immersed in the Avidin solution at room temperature for 1 hour to have a uniform Avidin adsorption over the surface. The samples are then

rinsed using 1X-PBS solution to removed the unattached Avidin, dried using nitrogen gas, and then taken for characterization.

Analysis of the Avidin immobilization protocols

The first protocol is based on the conversion of a carboxylic acid group into an NHS-ester by exposing the self assembled monolayer (SAM) of the APTES silane using a solution of EDC/NHS. This mechanism has been extensively used in the literature for generation of protein biochips [76]. The active ester undergoes a nucleophilic attack by an amine group, leading to the formation of an amide bond linking the protein to the assembled monolayer of the silane on the substrate. One of the major challenges associated with this mechanism is the susceptibility of the active ester to hydrolysis [164]. Generally, this activation is carried out in aqueous solutions where hydrolysis becomes a seriously competing reaction. Mechanism such as anhydrous environments, pH controlled buffer, etc. has been presented in the literature to overcome this issue [76],[164]. I employed MES buffer solution (pH 5.4) along with the 1X-PBS solution (pH 7.4) to enhance the reaction's favorable conditions. Repeatable results has been achieved at the cost of extensive care to avoid the competing hydrolysis reaction of the NHS-ester. It is recommended to prepare the EDC/NHS/Avidin solution immediately before the the functionalization and testing of the samples.

The second protocol is based on the activation of the amine functionalized SAM of APTES to form an aldehyde functionalized surface using the glutaraldehyde solution. Glutaraldehyde is a readily available, low cost biomolecular reagent, having a bifunctional molecule that contains two aldehyde groups separated by a short alkyl chain. One of the molecules reacts with the amine functionalized surface to form an imine bond, yielding an aldehyde functionalized surface. This approach results in a much easier and swift approach towards generation of protein (Avidin) surfaces. The approach is not prone to the competing reactions such as hydrolysis of the NHS-esters and does not require handling and processing with intricate buffers for surface functionalization. Moreover, these aldehyde

functionalized chips can be stored for later usage, unlike the EDC/NHS activated surfaces, which have to immediately utilized once activated. Therefore, the glutaraldehyde based surface functionalization scheme has been selected for the experiments.

4.6.2 Avidin-Biotin Immobilization

ATTO 520 Biotin fluorescent tag is used to detect the Avidin adsorption over the surface of the samples. The samples are immersed in 100 $\mu g/ml$ of the ATTO 520 biotin solution for 1.5 hours and then taken out for fluorescence measurements.

4.7 In-Situ Surface Modification of PDMS-based microfluidic chip

4.7.1 Microfluidic Device Fabrication

The fabrication of the PDMS microfluidic devices has been explained in detail in Chapter 3. Briefly, the SU-8 2035 negative photoresist is spin coated over the silicon wafers to achieve a uniform thickness of $50\mu m$. The spin coated wafer is then soft baked for 6 minutes at 65°C and 9 minutes at 90°C. The microfluidic channel's pattern is then defined by exposing the SU-8 using the MA-6 mask aligner setup with UV light (i-line, λ = 365nm) and a transparency mask. A post exposure bake for 6 minutes at 65°C and 9 minutes at 90°C is performed. The wafer is then developed in SU-8 developer (purchased from MicroChem, US) for 10 minutes, washed using IPA, dried using nitrogen gas, and inspected using a microscope and a profilometer. Once the master mold is made, it is silanized using (3-Mercaptopropyl)trimethoxysilane in a vacuum desiccator for 12 hours.

Sylgard 184 base and the curing agent are thoroughly mixed in 10:1 ratio, respectively. The mixture is then poured over the silanized master template in a plastic petri dish and degassed using vacuum desiccator for 6 hours. Once degassed, the PDMS is placed in an oven at 65°C for 4 hours for curing. The cured PDMS mold is peeled off the master mold using a razor blade and punch through holes are made for the fluid inlet. The PDMS mold is then cleaned using IPA, dried using nitrogen gas, and placed in the UVCOS (UV-Ozone

cleaning system) system for 10 minutes along with the silicon (or glass) substrate. After 10 minutes, the PDMS is taken out and carefully placed on the substrate, slightly pressed, and heated for 30 minutes on a hotplate at 65°C to ensure bonding. Once the bonding is complete, tubing, and connectors are attached to have inlet and outlet for the microfluidic chip.

The microfluidic chips are tested for flow leakage and clogging after the bonding process. Phosphate Buffer Saline (1X-PBS) solution (pH 7.4) has been flown at different flow rates and perfect flows of PBS without any leakage and clogging has been observed in the microfluidic chip. The microfluidic chip consists of a simple $50\mu m$ deep rectangular chamber with a width and length of $500\mu m$ and $1cm$, respectively. A flow of $10\mu l/min$ flow has been used throughout the experiments, unless stated otherwise.

4.7.2 In-situ surface oxidation

The microfluidic chip is initially purged with the 1X-PBS solution (pH 7.4) to remove the trapped air bubbles. Once the air is removed, an in-situ solution-based oxidation of the PDMS microfluidic chip has been performed. An oxidizing solution containing hydrogen peroxide (H_2O_2), hydrochloric acid (HCl), and water (H_2O) (in a volume ratio 1:1:5) is flowed for 10 minutes. The microfluidic chip is then purged with 1X-PBS solution, resulting in a hydrophilic silanol-covered PDMS surface.

4.7.3 In-situ silanization with APTES

The silanol-covered hydrophilic PDMS surfaces of the microfluidic chip are then treated with a silanization solution of 5% APTES ($C_9H_{23}NO_3Si$) in 2-Propanol (in a volume ratio) for 15 minutes, followed by a 2-Propanol rinse to remove the unreacted APTES. The microfluidic chip is then baked at 80°C for 30 minutes in an oven, followed by rinsing with 1X-PBS solution for 5 minutes. This results in an amino grafted PDMS and silicon/glass surfaces.

4.7.4 In-Situ silanization with GPTMS

The silanol-covered hydrophilic PDMS surfaces of the microfluidic chip are then treated with a silanization solution of 5% GPTMS ($C_9H_{23}NO_3Si$) in 2-Propanol (in a volume ratio) for 15 minutes, followed by a 2-Propanol rinse to remove the unreacted GPTMS. The microfluidic chip is then baked at 80°C for 30 minutes in an oven, followed by rinsing with 1X-PBS solution for 5 minutes. This results in an epoxy grafted PDMS and silicon/glass surfaces.

4.7.5 In-situ generation of aldehyde surface

A 2.5% glutaraldehyde ($C_5H_8O_2$) solution in 1X-PBS (in volume ratio) is flowed through the amino grafted microfluidic chip's surface for 15 minutes to generate aldehyde functionalized surfaces. this is followed by a 30 minutes of incubation at room temperature. The microfluidic chip is then rinsed with 1X-PBS solution for 5 minutes to remove the unreacted glutaraldehyde solution.

4.7.6 In-situ protein capturing on APTES modified surface

Avidin is a tetrameric biotin-binding protein with an estimate size of 66 - 69 kDa. FITC tagged Avidin protein has been used to monitor the attachment of Avidin to the aldehyde modified surfaces. A $10\mu g/ml$ of FITC Avidin solution in 1X-PBS has been prepared and is flowed through the microfluidic chips for 30 minutes. The microfluidic chip is then incubated at room temperature for 30 minutes to have a uniform Avidin adsorption over the surfaces of the microfluidic chip. The microfluidic chip is then rinsed using 1X-PBS solution to removed the unreacted FITC tagged Avidin.

4.7.7 In-situ lectin attachment on GPTMS modified surface

FITC tagged MAA-II Lectin has been used to to monitor the attachment of Lectin to the epoxy functionalized surfaces. A $100\mu g/ml$ of FITC MAA-II Lectin solution in 1X-PBS

has been prepared and is flowed through the microfluidic chip for 30 minutes. The microfluidic chip is then incubated at room temperature for 30 minutes to have a uniform Lectin adsorption over its surfaces. The microfluidic chip is then rinsed using 1X-PBS solution to removed the unreacted lectin and the fluorescence is measured.

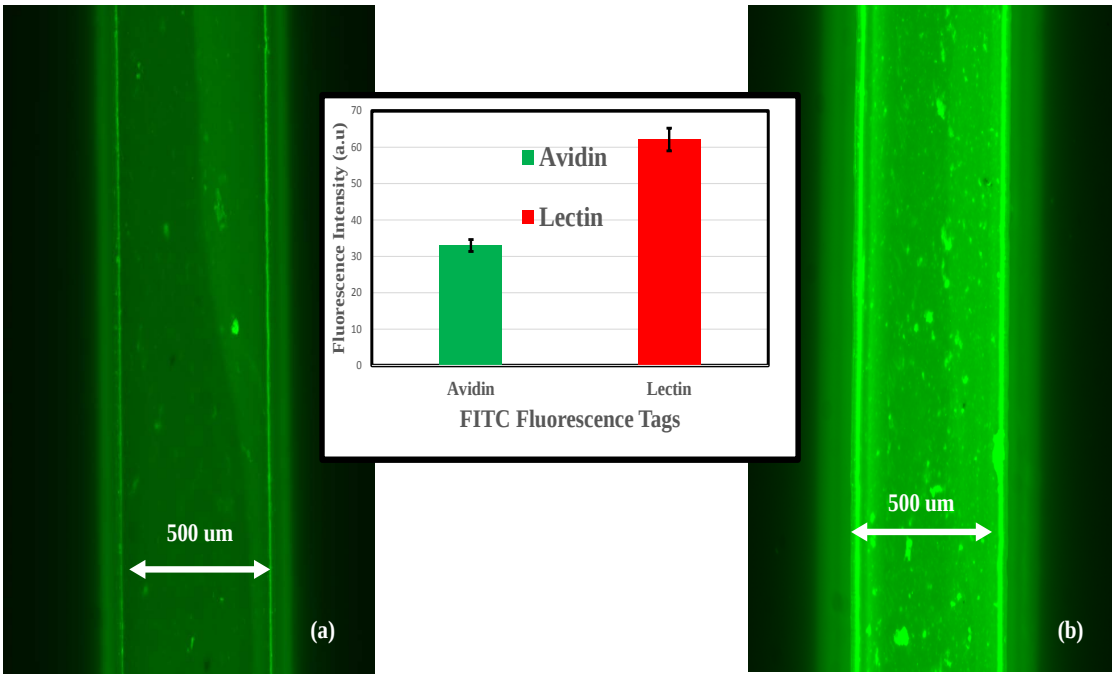

Figure 4.1: Fluorescence optical images obtained for $500\mu m$ wide and $50\mu m$ deep microchannels with (a) 10 $\mu g/ml$ FITC-Avidin coating and (b) 100 $\mu g/ml$ FITC-Maackia Amurensis (MAA) Lectin. The inset bar graph shows the obtained fluorescence intensities using the ImageJ software. Similar exposure settings has been used to obtain both of the images.

4.7.8 In-situ IgG protein attachment and detachment demonstration

I have used IgG antigen (produced from rabbit serum, lyophilized power) and biotinylated it with a photocleavable biotin linker (i.e., PC-biotin-PEG3-NHS-ester). The IgG antigen (2mg) is dissolved in 1 ml of 1X-PBS solution and 1 mg of PC-biotin-PEG3-NHS-ester is dissolved in 119 μl of N,N-Dimethylformamide (DMF) just before use. 26.6 μl of the solution is then added to the $2mg/ml$ solution of the biotinylated-IgG serum , followed by

incubation on ice for 2 to 3 hours. After the incubation, the excess PC-biotin-PEG3-NHS ester is removed using 0.5 ml micro-concentrator vials (Amicon $0.5ml$ Ultra, purchased from Sigma Aldrich, US) using a microcentrifuge device (1000g, 100 kDa MW cutoff, 30 minutes).

The biotinylated-PC-IgG serum solution is diluted to a concentration of 0.5 mg/ml using 1X-PBS solution and is then flowed in the microfluidic chip for 5 minutes. The chip is then incubated at room temperature for 30 minutes. The process is repeated three times to have a uniform adsorption of biotinylated-PC IgG protein across the PDMS capture chamber. The unabsorbed sample is removed using 1X-PBS rinse. Blocking solution of BSA (Bovine Serum Albumin) in 1X-PBS $(1\%(w/v))$ is then flowed for 5 minutes and the chip is incubated for 30 minutes at room temperature to prevent the non-specific adsorption.

The efficacy of this functionalization protocol (i.e., attachment and release of the IgG protein) is evaluated using FITC tagged anti-IgG secondary antibodies (anti-rabbit IgGs produced in goat). A solution of the secondary anti-bodies is made in 1X-PBS with a concentration of $100\mu g/ml$ and is flowed in the microfluidic chip for 10 minutes. The chip is then incubated at room temperature for 30 minutes (in dark environment wrapped in aluminum foil). The chip is rinsed with 1X-PBS for 5 minutes and imaged for fluorescence measurements. Once the fluorescence is observed, the chip is placed under a UV lamp (MJB4 Mask Aligner Lamp, $11.1mW/cm^2$ intensity, distance of 5cm) for 10 minutes. After the exposure, the chip is rinsed using 1X-PBS solution for 10 minutes and the fluorescence is measured again.

4.8 Characterization Techniques

4.8.1 Spectroscopic Ellipsometry Measurements

The variable angle spectroscopic ellipsometry (VASE) characterization of the samples has been performed using Woollam M2000 Ellipsometer setup (J. A. Woollam Co., Lincoln, NE, USA). The spectroscopic data was obtained from 370 nm to 1690 nm at three different

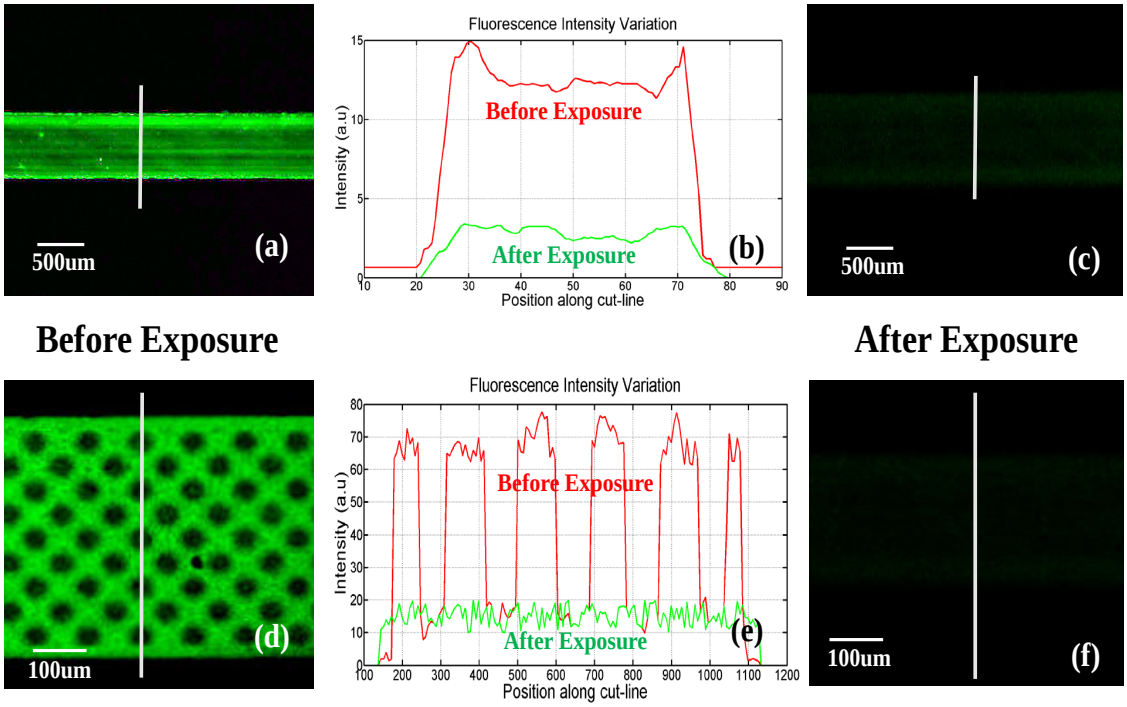

Figure 4.2: Fluorescence optical micrograph for IgG - anti IgG (FITC) functional microfluidic chip (a) Pre-UV exposure fluorescence image in a straight microfluidic channel (b) Pixel intensity variation across the cut-line (white line in (a) obtained using ImageJ software) (c) Post-UV exposure fluorescence image in the straight microfluidic channel (d) Pre-UV exposure fluorescence image in the micropillar based microfluidic capture chamber (e) Pixel intensity variation across the cut-line (white line in (d) obtained ImageJ software) (f) Post-UV exposure fluorescence image in the micropillar based microfluidic capture chamber. The fluorescence reading has been obtained at different exposure settings.

angles of 60°, 65°, and 70°. Five different points on the sample has been measured and the best fit analysis for the obtained data has been performed using the Cauchy dispersion model [165]. The thickness and refractive index measurements for each layer has been obtained from the observed data.

4.8.2 Fourier Transform Infra-Red (FTIR) Spectroscopy

The FTIR spectrum of the samples has been observed using Nicolet iS50 FT-IR (Thermo Scientific, USA) setup. The built-in mid and far IR capable diamond stage has been used to observe the spectrum for each of the silanized samples. The observations has been obtained

at $4cm^{-1}$ resolution for background (no sample) and with the sample, using 200 repetitive scans to minimize the signal to noise ratio. A complete spectrum for each sample was obtained from $500cm^{-1}$ to $3500cm^{-1}$.

4.8.3 X-Ray photoelectron spectroscopy (XPS)

The chemical composition of each sample after each coating step has been performed using X-Ray photoelectron spectroscopy (XPS) analysis using K-Alpha X-ray photoelectron spectrometer (Thermo Fisher Scientific, Inc., US). A survey spectrum has been collected from 0 to 1100 eV, with each scan (10 scans in total for survey spectrum) having a pass energy of 160 eV, dwell time of 50 ms and a 400 μm spot size for each of the sample. Individual spectrum for silicon, carbon, nitrogen, and oxygen has also been collected with each scan having a pass energy of 50 eV and a dwell time of 50 ms to perform the elemental analysis. 10 scans has been performed for each of the elements to have better signal to noise performance.

4.8.4 Fluorescence Microscopy

Zeiss 710 NLO confocal microscope and Zeiss axio-observer Z1 Fluorescent Microscope has been used to observed the fluorescence measurements from the sample. ATTO 520 fluorescence tagged biotin, FITC tagged Avidin, FITC tagged secondary IgG antibodies, and FITC tagged MAA-II lectins have been employed as fluorescence tagged biomolecules to monitor the surface coating. The ATTO 520 tag works best for an excitation wavelength of 520 nm, resulting in an emission of 540 nm, while the FITC tag works best for an excitation wavelength of 490nm, resulting in an emission of 525nm. These both tags can be easily observed using the Zeiss confocal and axio-observer systems.

4.9 FTIR Characterization Results

4.9.1 Analysis for Silicon and PDMS Samples

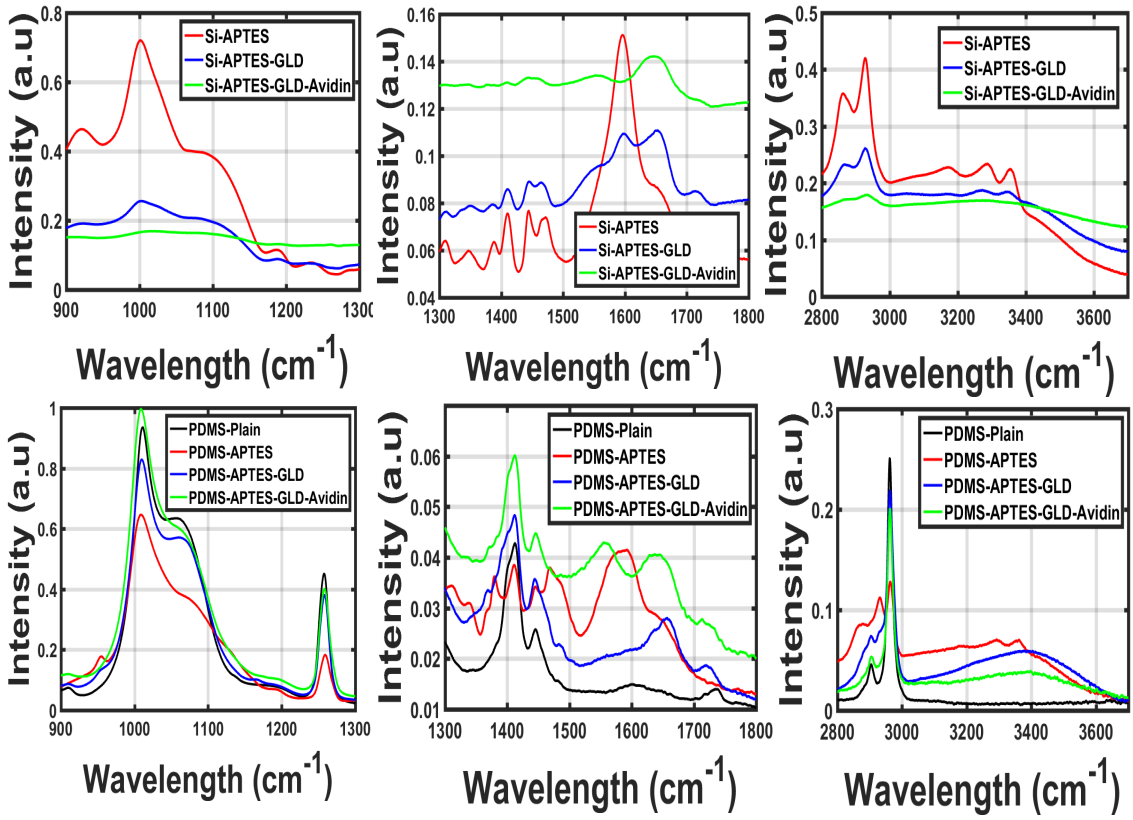

Figure 4.3: The figure shows FTIR spectra for APTES, GLD, Avidin coated silicon sample in the range of (a) 900 to 1300 cm^{-1} (b) 1300 to 1800 cm^{-1}, and (c) 2800 to 3500 cm^{-1}. FTIR spectra of APTES, GLD, Avidin coated PDMS sample in the range of (d) 900 to 1300 cm^{-1} (e) 1300 to 1800 cm^{-1}, and (f) 2800 to 3500 cm^{-1}.

Complete FTIR spectrum for the APTES, glutaraldehyde, and Avidin attachment over a silicon and PDMS surface has been collected from 550 to 5000 cm^{-1}. Three different wavelength ranges i.e., 900 to 1300 cm^{-1}, 1300 to 1800 cm^{-1}, and 2800 to 3500 cm^{-1} has been selected for observation of the surface functionalization of silicon and PDMS surface. Figures 4.3(a), 4.3(b), and 4.3(c) shows the FTIR spectrum observed for functionalization of a silicon sample while the figures 4.3(d), 4.3(e), and 4.3(f) shows the FTIR spectrum observed for functionalization of a PDMS sample, for different ranges of wavelength as

mentioned, respectively.

Figure 4.3(a) and 4.3(d) shows the spectrum observed in the range of 900 to 1300 cm^{-1} for both silicon and PDMS samples, respectively. Longitudinal optical mode (LO mode) has been observed in the silicon sample around 1230 to 1235 cm^{-1} owing to the presence of the thin, reflective native oxide over the silicon surface, whereas, no such mode can been seen for the PDMS sample. Vibrational modes around 960, 1080, and 1195 cm^{-1} has been observed and are considered to arise from unhydrolyzed ethoxy moieties in APTES ($-OCH_2CH_3$). The extremely low intensity of these peaks indicate very low amount of condensation of APTES resulting in thin layer of APTES over the silicon and PDMS surface. The peaks at 1045 cm^{-1} and 1125 cm^{-1} are attributed for the presence of Si-O-Si and Si-O moieties, respectively. The low intensity of these peaks also correspond to the extremely small thickness of the APTES adsorbed layer over the silicon and PDMS samples.

Figure 4.3(b) and 4.3(e) shows the spectrum observed in the range of 1300 to 1800 cm^{-1} for both silicon and PDMS samples, respectively. Peaks observed around 1655 cm^{-1} reveals the presence of a vibration mode owing to the imine group. Peaks corresponding to 1330, 1480, and 1590 cm^{-1} are considered to be the vibrational modes from the bicarbonate amino groups of the physiosorbed or condensed APTES films over the surface of silicon and PDMS, respectively. The symmetric and asymmetric deformation modes of the $-CH_3$ group from ethoxy moieties of APTES has been observed around 1390 and 1440 cm^{-1}, respectively. The presence of these two modes indicates the existence of ethoxy groups in APTES, presumably due to incomplete siloxane condensation. The bending mode of the methylene group $-CH_2$ adjacent to the silicon in APTES has been observed with a peak around 1410 cm^{-1}. The surfaces are treated with glutaraldehyde solution after silanization. The FTIR spectra indicates the reactions between the glutaraldehyde and silane functional group. A relative increase in the visibility of imine (-C=N-) band i.e., 1620 - 1660 cm^{-1} has been observed while the intensity of the dominant amine (-NH_2) band at 1580 cm^{-1}

has been decreased after the reaction with glutaraldehyde. This imine group is expected to be formed by the Schiff base reaction where a nucleophilic reaction takes place between the amine group (from silanes) and the aldehyde group (from the glutaraldehyde). A vibrational peak at 1720 cm^{-1} has been detected which is the characteristic of C=0 groups present in the aldehydes. The glutaraldehyde treatment is followed by Avidin treatment of the samples. The appearance of distinct amide I peak at around 1650 cm^{-1} is a characteristic of Avidin. This peak is a an indicator of a predominately β-sheet and extended sheet structure of the Avidin protein. Amide II peak at 1450 cm^{-1} has also been observed for the Avidin treated samples.

Figure 4.3(c) and 4.3(f) shows the spectrum observed in the range of 2800 to 3500 cm^{-1} for both silicon and PDMS samples, respectively. Similar trends has been observed for the both samples. Peaks observed between 2800 and 3000 cm^{-1} originate from the stretching of the -CH modes of the APTES and ethoxy groups whereas, symmetric and asymmetric -NH mode stretching, owing the presence of amino groups in the APTES has been observed around 3250 to 3350 cm^{-1}. No broad peak around 3300 cm^{-1} has been observed showing negligible presence of -OH bonds i.e., trapped water or moisture in the cured APTES film over the silicon, as well as the PDMS sample. The -NH and -CH mode stretching has also been observed for the glutaraldehyde and Avidin treated samples. Moreover, widening of peaks around 3300 cm^{-1} for both glutaraldehyde and Avidin treated samples also indicates the presence of -OH bonds. This widening of -CH, -NH, and -OH peaks is more predominant for the silicon samples compared to the PDMS samples.

4.9.2 Analysis for Glass Samples

Complete FTIR spectrum for the APTES, glutaraldehyde, and Avidin attachment over a glass surface has been collected from 550 to 5000 cm^{-1}. Three different wavelength ranges i.e., 800 to 1300 cm^{-1}, 1300 to 1800 cm^{-1}, and 2400 to 3600 cm^{-1} has been selected for observation of the surface functionalization of the glass surface. Figures 4.4(a), 4.4(b), and

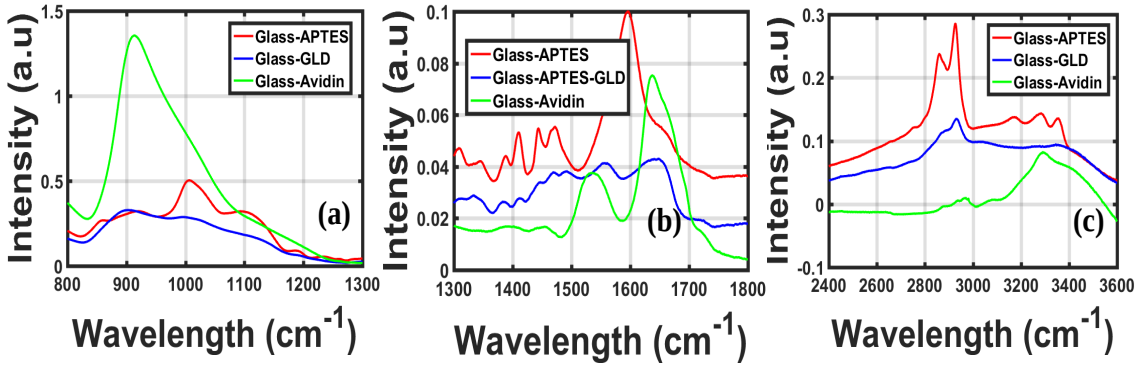

Figure 4.4: The figure shows FTIR spectra for APTES, GLD, Avidin coated glass sample in the range of (a) 900 to 1300 cm^{-1} (b) 1300 to 1800 cm^{-1}, and (c) 2400 to 3600 cm^{-1}.

4.4(c) shows the FTIR spectrum observed for functionalization of the glass sample.

Figure 4.4(a) shows the spectrum observed in the range of 800 to 1300 cm^{-1} for the glass sample. Vibrational modes around 960, 1080, and 1195 cm^{-1} has been observed and are considered to arise from unhydrolyzed ethoxy moieties in APTES ($-OCH_2CH_3$). The extremely low intensity of these peaks indicate very low amount of condensation of APTES resulting in thin layer of APTES over the silicon and PDMS surface. The peaks at 1045 cm^{-1} and 1125 cm^{-1} are attributed for the presence of Si-O-Si and Si-O moieties, respectively. The low intensity of these peaks also correspond to the extremely small thickness of the APTES adsorbed layer over the silicon and PDMS samples. The APTES surfaces treated with glutaraldehyde show flattened responses as the glutaraldehyde treatment removes the unadsorbed and condensed APTES from the surface, generating an aldehyde modified surface.

Figure 4.4(b) shows the spectrum observed in the range of 1300 to 1800 cm^{-1} for the

glass sample. Peaks observed around 1655 cm^{-1} reveals the presence of a vibration mode owing to the imine group. Peaks corresponding to 1330, 1480, and 1590 cm^{-1} are considered to be the vibrational modes from the bicarbonate amino groups of the physiosorbed or condensed APTES films over the glass surface. The symmetric and asymmetric deformation modes of the $-CH_3$ group from ethoxy moieties of APTES has been observed around 1390 and 1440 cm^{-1}, respectively. The presence of these two modes indicates the existence of ethoxy groups in APTES, presumably due to incomplete siloxane condensation. The bending mode of the methylene group $-CH_2$ adjacent to the silicon in APTES has been observed with a peak around 1410 cm^{-1}. The surfaces are treated with glutaraldehyde solution after the silanization. The FTIR spectra indicates the reactions between the glutaraldehyde and silane functional group. A relative increase in the visibility of imine (-C=N-) band i.e., 1620 - 1660 cm^{-1} has been observed while the intensity of the dominant amine (-NH_2) band at 1580 cm^{-1} has been decreased after the reaction with glutaraldehyde. This imine group is expected to be formed by the Schiff base reaction where a nucleophilic reaction takes place between the amine group (from silanes) and the aldehyde group (from the glutaraldehyde). A vibrational peak at 1720 cm^{-1} has been detected which is the characteristic of C=0 groups present in the aldehydes. The glutaraldehyde treatment is followed by Avidin treatment of the samples. The appearance of distinct amide I peak at around 1650 cm^{-1} is a characteristic of Avidin. This peak is a an indicator of a predominately β-sheet and extended sheet structure of the Avidin protein. Amide II peak at 1450 cm^{-1} has also been observed for the Avidin treated samples.

Figure 4.4(c) shows the spectrum observed in the range of 2400 to 3600 cm^{-1} for the glass sample. Peaks observed between 2800 and 3000 cm^{-1} originate from the stretching of the -CH modes of the APTES and ethoxy groups whereas, symmetric and asymmetric -NH mode stretching, owing the presence of amino groups in the APTES has been observed around 3250 to 3350 cm^{-1}. No broad peak around 3300 cm^{-1} has been observed showing negligible presence of -OH bonds i.e., trapped water or moisture in the cured APTES film

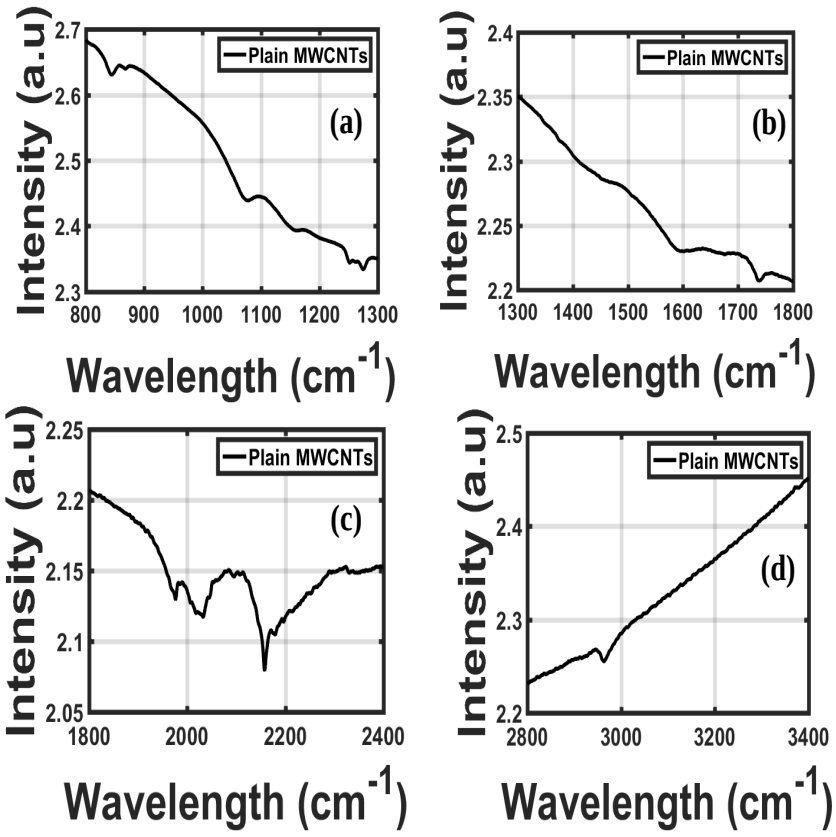

Figure 4.5: The figure shows FTIR spectrum for the untreated MWCNT sample

over the silicon, as well as the PDMS sample. The -NH and -CH mode stretching has also been observed for the glutaraldehyde and Avidin treated samples. Moreover, widening of peaks around 3300 cm^{-1} for both glutaraldehyde and Avidin treated samples also indicates the presence of -OH bonds.

4.9.3 Analysis for MWCNT Samples

Complete FTIR spectrum for the APTES, glutaraldehyde, and Avidin attachment over MWCNT samples has been collected from 550 to 5000 cm^{-1}. Three different wavelength ranges i.e., 800 cm^{-1} to 1300 cm^{-1}, 13000 cm^{-1} to 1800 cm^{-1}, and 2800 cm^{-1} to 3400 cm^{-1} has been selected for observation of the surface functionalization of the MWCNT samples. Figures 4.5 shows the FTIR spectrum observed for untreated pristine MWCNT samples for the different ranges of wavelength as mentioned. The pristine MWCNT sam-

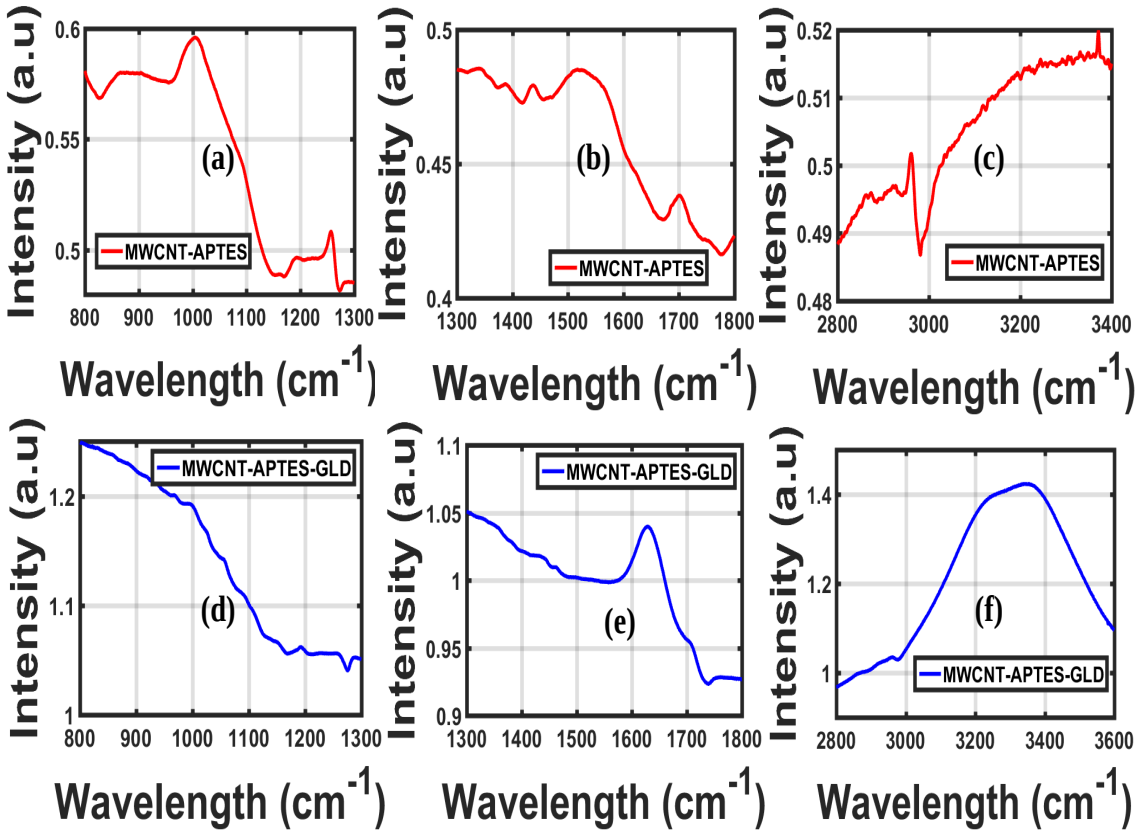

Figure 4.6: The figure shows FTIR spectra for APTES and glutaraldehyde treated MWCNT sample

ples show21 the stretching vibrational peaks observed from 2100 to 2260 cm^{-1} shows the presence of Alkynes. This observation substantiates the fact that multiple alkynes react with acetylene to form the MWCNTS [166]. The aromatic weak vibrational stretching is observed from 1400 to 1600 cm^{-1}. Moreover, the presence of the vibrational stretching around 1620 to 1680 cm^{-1} also ensure the presence of C=C bonds.

The MWCNTs have shown similar peaks and trends for APTES functionalization as seen earlier with the silicon, PDMS, and glass samples. Similarly, identical peaks and trends have been observed for the glutaraldehyde and Avidin treated MWCNT samples. These trends can be observed in the plots shows in figures 4.6 and 4.7.

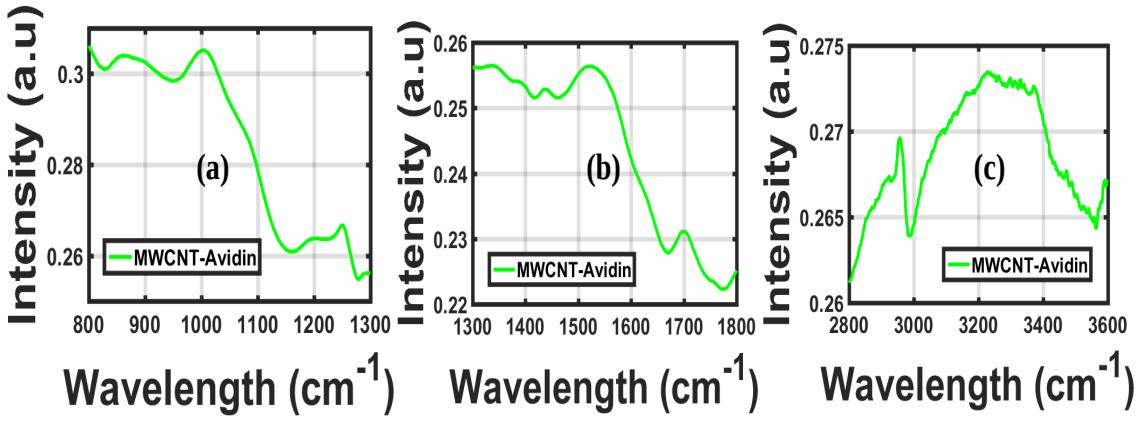

Figure 4.7: The figure shows FTIR spectrum for the Avidin treat MWCNT samples

4.10 XPS Characterization Results

The figure 4.8 shows the XPS survey spectra obtained for a cleaned silicon sample without any surface functionalization (in red) and an Avidin functionalized silicon sample (in blue). The peaks (in red) show the presence of Silicon and Oxygen in the sample. The presence of the oxygen peak substantiates the presence of native oxide layer over the silicon sample. Two new peaks for has been observed in the Avidin spectrum (in blue) showing the presence of Carbon and Nitrogen over the surface. Moreover, the intensity of the silicon and oxygen peaks has also decreased in the spectrum shown for Avidin functionalization. These results shows the presence of Avidin over the Silicon sample.

The table 4.5 contains the elemental composition of Silicon, Nitrogen, Oxygen, and Carbon over the silicon sample. These elements are the constituents of the biomolecular

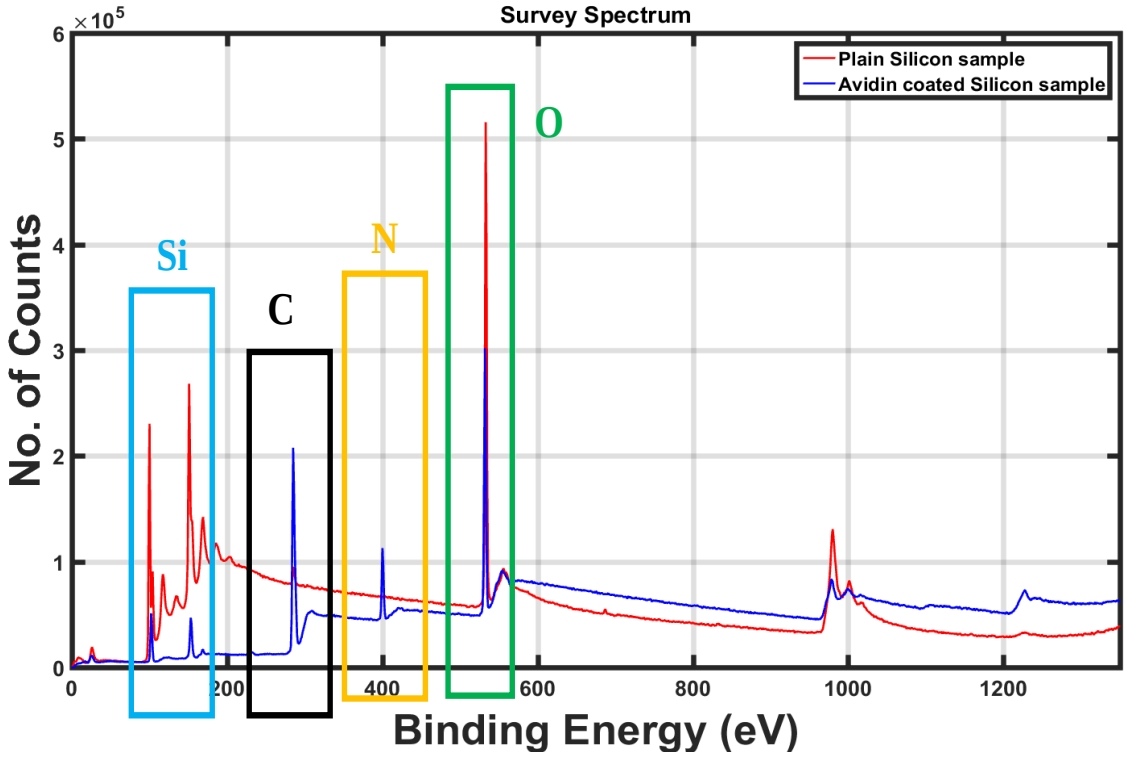

Figure 4.8: The figure shows survey XPS spectra for a plain silicon sample (red) and Avidin coated silicon sample (blue)

compounds employed for the surface functionalization. The table presents the variations in the atomic percentage for each of the elements, corresponding to every surface functionalization step. The results shows the viability of the Silicon surface functionalization protocol by showing the presence of biomolecular attachment over the surface.

The figure 4.9 shows the XPS survey spectra obtained for a cleaned glass sample without any surface functionalization (in red) and an Avidin functionalized glass sample (in

Table 4.5: Elemental composition for functionalized Silicon sample obtained using XPS analysis

	Silicon (Si)	**Carbon (C)**	**Oxygen (O)**	**Nitrogen (N)**
Plain Sample	53.91	4.64	41.45	0
APTES Coating	14.54	48.78	25.92	10.76
APTES - Glutaraldehyde Treatment	9.65	59.58	22.31	8.52
Avidin Coating	9.82	56.6	23.43	10.14

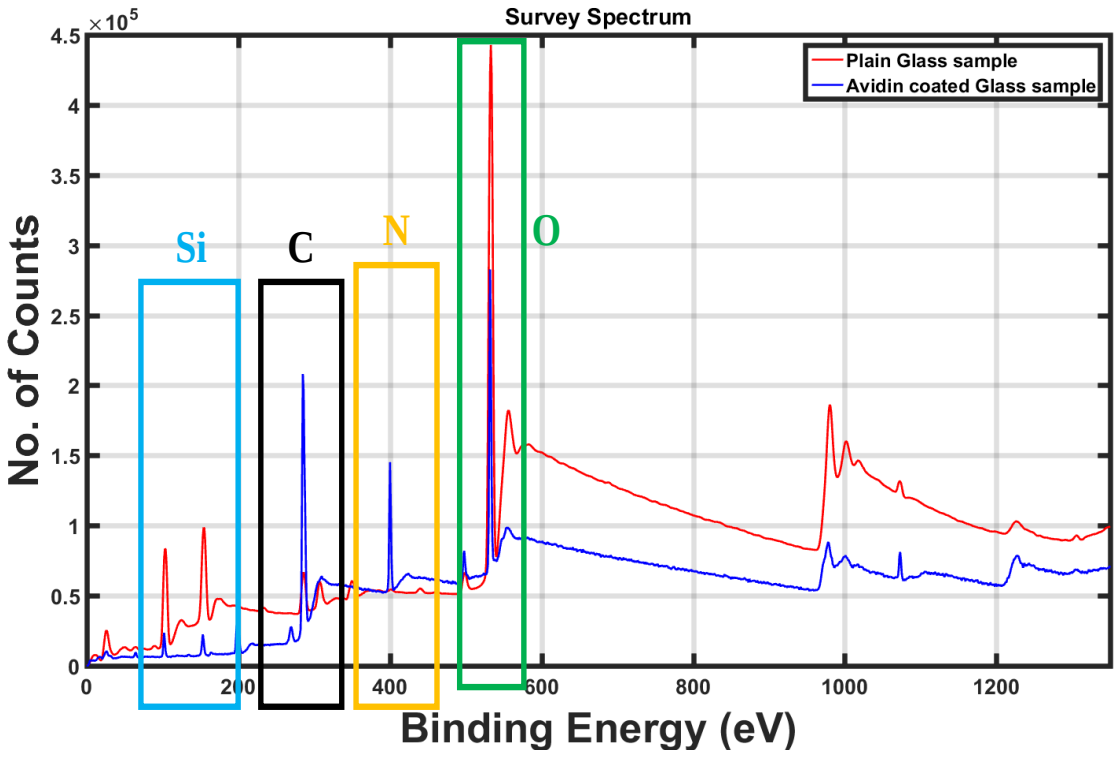

Figure 4.9: The figure shows survey XPS spectra for a plain glass sample (red) and Avidin coated glass sample (blue)

blue). The peaks (in red) show the presence of Silicon and Oxygen in the sample. The presence of the both the elements substantiates the composition of glass i.e., silicon oxide. Two new peaks for has been observed in the Avidin spectrum (in blue) showing the presence of Carbon and Nitrogen over the surface. Moreover, the intensity of the Silicon and Oxygen peaks has also decreased in the spectrum shown for Avidin functionalization. These results shows the presence of Avidin over the glass sample.

The table 4.6 contains the elemental composition of Silicon, Nitrogen, Oxygen, and

Table 4.6: Elemental composition for functionalized glass sample

	Silicon (Si)	**Carbon (C)**	**Oxygen (O)**	**Nitrogen (N)**
Plain Sample	27.5	9.42	63.08	0
APTES Coating	19.3	49.77	23.82	7.12
APTES - Glutaraldehyde Treatment	10.12	60.53	21.48	7.87
Avidin Coating	10.82	58.13	22.82	8.23

Table 4.7: Elemental composition for functionalized MWCNT sample

	Silicon (Si)	Carbon (C)	Oxygen (O)	Nitrogen (N)
Plain Sample	0	96.36	3.27	0
APTES Coating	7.4	67.04	20.66	4.89
APTES - Glutaraldehyde Treatment	9.8	61.74	19.95	8.51
Avidin Coating	10.5	53.63	27.21	9.12

Carbon over the glass sample. These elements are the constituents of the biomolecular compounds employed for the surface functionalization. The table presents the variations in the atomic percentage for each of the elements, corresponding to every surface functionalization step. The results shows the viability of the glass surface functionalization protocol by showing the presence of biomolecular attachment over the surface.

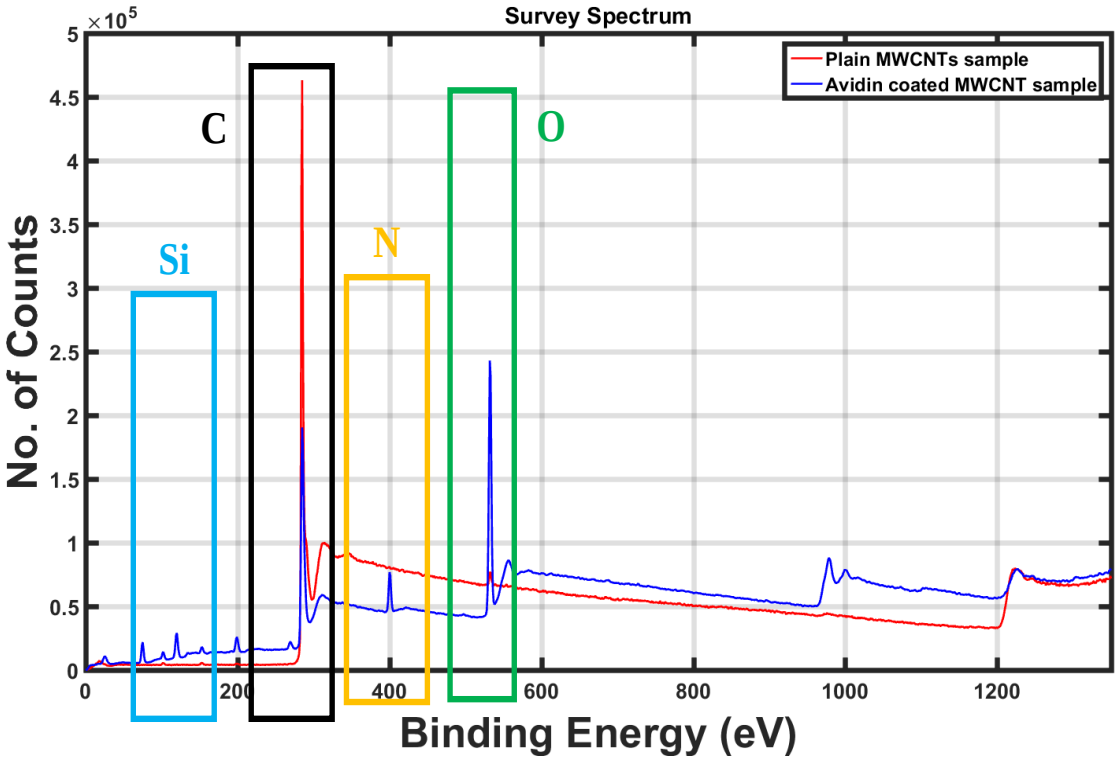

Figure 4.10: The figure shows survey XPS spectra for a MWCNT sample (red) and Avidin coated MWCNT sample (blue)

The figure 4.10 shows the XPS survey spectra obtained for a MWCNT sample without any surface functionalization (in red) and an Avidin functionalized MWCNT sample (in

Table 4.8: Elemental composition for functionalized PDMS sample

	Silicon (Si)	**Carbon (C)**	**Oxygen (O)**	**Nitrogen (N)**
Plain Sample	19.47	51.07	3.2729.19	0
APTES Coating	24.83	44.34	29.35	1.49
APTES - Glutaraldehyde Treatment	11.28	60.29	23.29	5.14
Avidin Coating	10.52	58.17	24.02	7.29

blue). The peaks (in red) show the presence of Carbon and Oxygen (small intensity peak) in the sample. The presence of the both the elements substantiates the composition of the MWCNTs. A dominant Carbon peaks shows a strong presence of Carbon, which is the primary constituent of the MWCNTs. The Oxygen peak can be attributed to some oxidation or trapped Oxygen in the MWCNT sample. Two new peaks for Silicon and Nitrogen has been observed in the Avidin spectrum (in blue) showing the presence of Silicon and Nitrogen over the surface. Moreover, the intensity of the Carbon peak has considerably decreased, while the Oxygen peak becomes more prominent for the Avidin functionalization. These results shows the presence of Avidin over the MWCNT surface.

The table 4.7 contains the elemental composition of Silicon, Nitrogen, Oxygen, and Carbon over the MWCNT sample. These elements are the constituents of the biomolecular compounds employed for the surface functionalization. The table presents the variations in the atomic percentage for each of the elements, corresponding to every surface functionalization step. The results shows the viability of the MWCNT surface functionalization protocol by showing the presence of biomolecular attachment over the surface.

The figure 4.11 shows the XPS survey spectra obtained for a PDMS sample without any surface functionalization (in red) and an Avidin functionalized PDMS sample (in blue). The peaks (in red) show the presence of Silicon, Carbon, and Oxygen in the sample. The presence of these elements substantiates the composition of the PDMS. One new peak for Nitrogen has been observed in the Avidin spectrum (in blue) showing the presence of Nitrogen over the surface. Moreover, the intensity of the peaks obtained earlier has

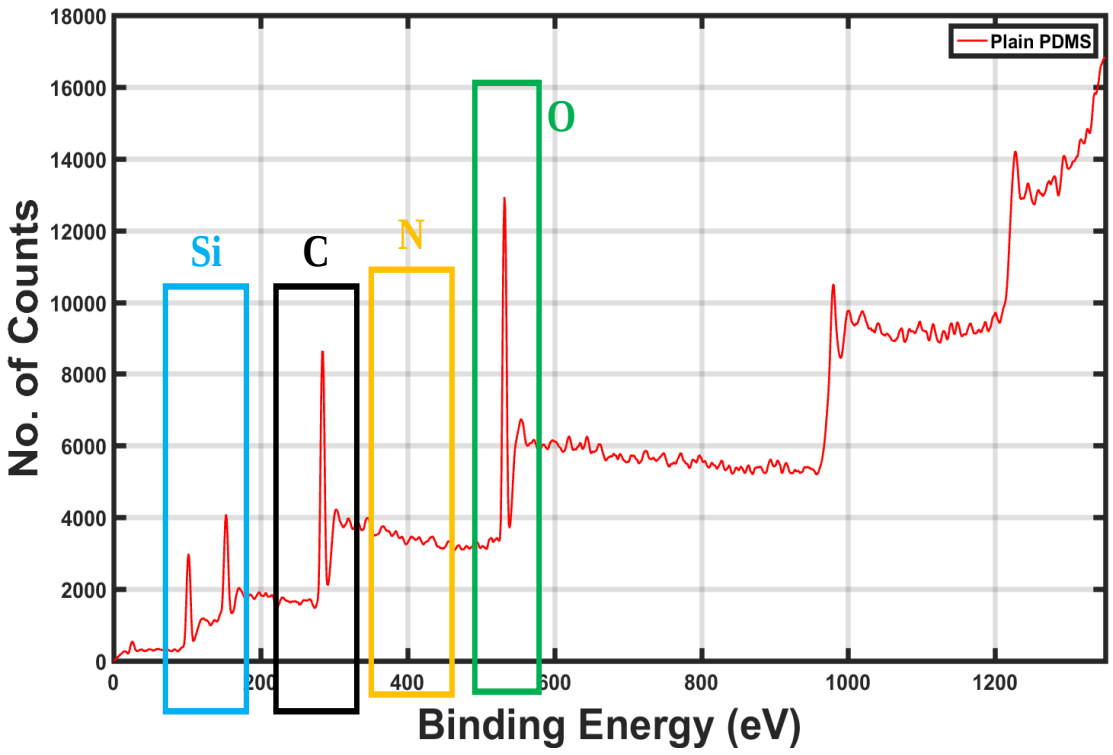

Figure 4.11: The figure shows survey XPS spectra for a plain PDMS sample

Table 4.9: Elemental composition for GPTMS functionalized silicon sample

	Silicon (Si)	**Carbon (C)**	**Oxygen (O)**	**Nitrogen (N)**
Plain Sample	54.21	1.89	43.89	0
GPTMS Coating	17.61	54.45	27.92	0

changed, showing prominent functionalization of the PDMS surface with the Avidin.

The table 4.8 contains the elemental composition of Silicon, Nitrogen, Oxygen, and Carbon over the PDMS sample. These elements are the constituents of the biomolecular compounds employed for the surface functionalization. The table presents the variations in the atomic percentage for each of the elements, corresponding to every surface functionalization step. The results shows the viability of the PDMS surface functionalization protocol by showing the presence of biomolecular attachment over the surface.

The figure 4.12 shows the XPS survey spectra obtained for a cleaned Silicon sample without any surface functionalization (in red) and GPTMS functionalized Silicon sample

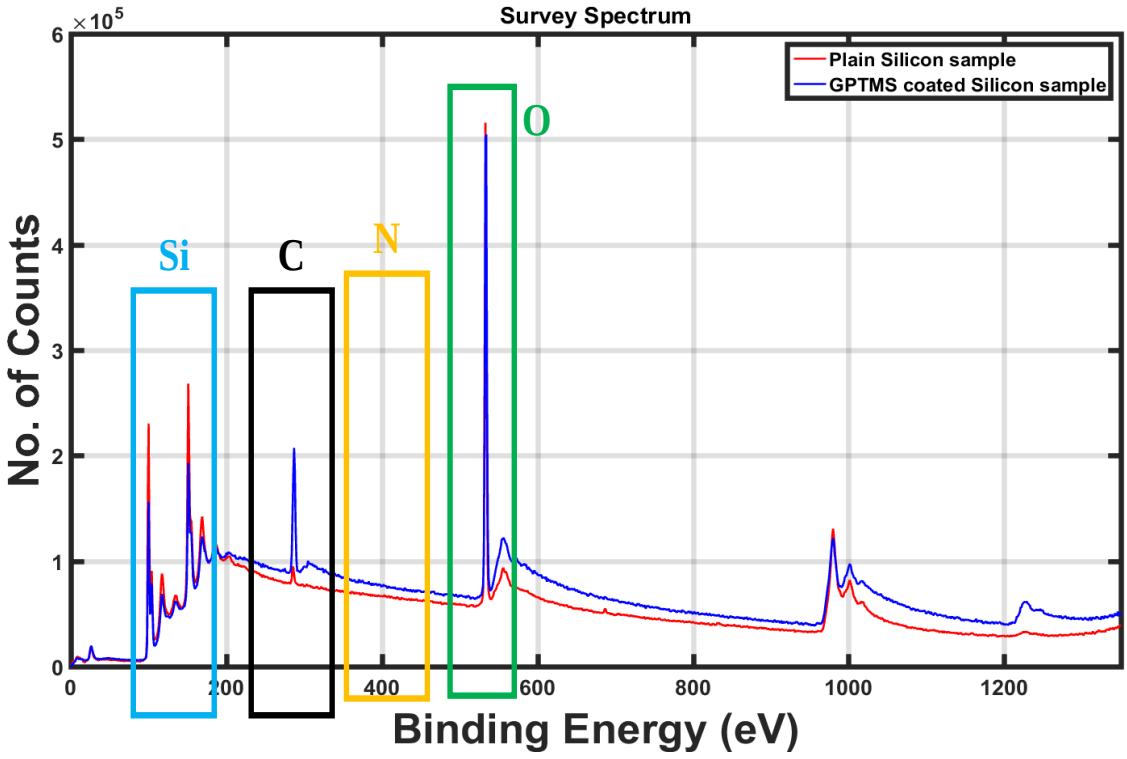

Figure 4.12: The figure shows survey XPS spectra for a plain silicon sample (red) and GPTMS coated silicon sample (blue)

(in blue). The peaks (in red) show the presence of Silicon and Oxygen over the sample. The presence of the Oxygen peak substantiates the presence of a native oxide layer over the Silicon sample. One new peak has been observed in the GPTMS spectrum (in blue) showing the presence of Carbon over the surface. Moreover, the intensity of the silicon and oxygen peaks has also decreased in the spectrum shown for GPTMS functionalization. These results shows the presence of GPTMS over the Silicon sample. The GPTMS epoxy silane does not contain any Nitrogen, unlike the other surface functionalization reagents employed earlier. This fact is evident from the obtained XPS spectrum.

The table 4.9 contains the elemental composition of Silicon, Nitrogen, Oxygen, and Carbon over the GPTMS coated silicon sample. These elements are the constituents of the biomolecular compounds employed for the surface functionalization. The table presents the variations in the atomic percentage for each of the elements, corresponding to every surface functionalization step. The results shows the viability of the Silicon surface func-

tionalization protocol by showing the presence of biomolecular attachment over the surface. It should be noted that no Nitrogen has been observed in the analysis.

CHAPTER 5
MICROPILLAR BASED MICROFLUIDIC PLATFORM FOR ON-CHIP BIOMOLECULAR PRE-CONCENTRATION AND FILTRATING

5.1 Introduction

In this chapter, I present my approach for biomolecular (e.g., proteins, biomarkers) filtering and pre-concentration based on affinity-based separation approach. In this approach, the target biomolecule is captured and pre-concentrated on a surface (i.e., PDMS micropillars) based on the binding of the biomolecule to its specific affinity epitope. The pre-concentrated biomolecules are then released on demand and can be recaptured on a sensing transducer (e.g., optical sensor arrays), allowing a complete label-free sensing and profiling (secondary epitopes such as glycoforms) of the biomolecules. This chapter covers the capturing, pre-concentration, glycoprofiling, and on demand release of the desired PSA cancer biomolecules.

I present a detailed account of a multi-step surface functionalization protocol to optimize on-the-flow surface functionalization and the capturing efficiency of biomolecules in a microfluidic platform. I designed, optimized, fabricated, and characterized a PDMS based microfluidic platform, having a micropillar based biomolecular pre-concentration chamber allowing increased surface-to-volume ratio (SVR) for enhanced biomolecular filtering and preconcentration. The surface of the pre-concentrator chamber is first functionalized with the Avidin protein biomolecules. A biotinylated photo-cleavable (PC) linker conjugated with a biomolecular specific antibodies (i.e., anti-PSA IgGs) is then immobilized on pre-concentrator through the Avidin-Biotin binding. The biomolecules are then flowed through the microfluidic device and are captured in the pre-concentration chamber. Once the capturing and pre-concentration has been performed, the biomolecules are released on demand

for recapturing, profiling, and label-free detection.

5.2 Design rationale for the microfluidic device

In the microfluidic chip, the biomolecules are chemically immobilized on the channel surfaces (walls) and the silicon substrate. The process of capturing is primarily based on interaction between the biomolecules and the self assembled mono-layers developed inside the microfluidic chip. The microfluidic chip has a low Reynolds number, resulting in a strictly laminar flow inside the chip. The laminar flow allows the biomolecular capturing process to be affected primarily by the density of the molecular interaction (binding) sites, molecular reaction rate, and the reaction time between the incoming molecule and the binding sites.

Microfluidic affinity based pre-concentration and filtering devices are engineered for transport and analysis of biomolecular samples (e.g., blood, plasma, serum, etc.) such that the biomolecules (proteins, nano/micro particles, cells, viruses, DNA, etc.) are separated owing to their binding to specific target sites. It has been observed that higher surface-to-volume ratio (SVR) results in enhanced pre-concentration and better capturing efficiency for these devices [167],[168]. Moreover, lesser volumes allows faster reaction dynamics, sensitivities, less processing time, and above all very small size of precious biomolecular samples [40],[169].

Clogging in microfluidic devices (especially in blood processing chips) is a key challenge that decreases their efficiency and lifetime. Clogging in microfluidic devices mainly results from sieving of particles, bridging, and aggregation of biomolecules and particles [170]. The sieving is observed when the biomolecular size (D) is larger or comparable to the minimum width (W) of the device (i.e., $W/D \leq 1$), for any biomolecular concentration in the sample [171]. Bridging is observed for samples having higher biomolecular concentration passing through a narrow microchannels [172],[173], whereas aggregation is observed for dilute biomolecular solutions having fairly larger constrictions but requiring

wall-to-biomolecule and inter-biomolecular attractions [174].

To address these challenges, I propose a circular micropillar based microfluidic device design such that the minimum constriction dimension (i.e., pillar spacing) is assumed as $d_{min} = 10\mu m$ (values below $10\mu m$ will result in clogging especially for blood processing devices as the size of white blood cells (lymphocytes, neutrophils, etc.) ranges from 8 to $15\mu m$). The micropillars are arranged in a hexagonal array pattern to achieve large interaction area with the input sample to enhance the probability of biomolecular capturing. The introduction of micropillars increases the availability of the binding sites per unit volume of the chip, allowing enhanced reaction rates and more attachment of the biomolecules. This increases the overall capture efficiency of the device.

I assumed a rectangular pre-concentration channel, having a length (L) of $0.01cm$, a width (W) of $500\mu m$, and a height (h) of $50\mu m$, allowing a interaction volume of $250nl$. To have an optimized hexagonal placement of micropillar in the pre-defined rectangular chamber, I came up with the universal design conditions for a micropillar based pre-concentration device design. These conditions can be employed to evaluate the design parameters for any circular micropillar based design with given rectangular dimensions and minimum unit cell spacing of the pre-concentration chamber.

Condition - 1: For all cases, the total circular area of the introduced circular micropillars should always be less than the total base area of the microfluidic channel i.e., $N\pi r^2 \leq WL$

Condition - 2: The change in surface area inside the pre-concentration chamber after the introduction of micropillars should be greater than zero such that the overall SVR always increase i.e., $N(2\pi rh) - 2N(\pi r^2) \geq 0$, resulting in $h \geq r$

Condition 3: For a unit cell of micropillars as shown in the figure 5.1,

$$d_{min} = \frac{S - 0.8242r}{\sqrt{2}}$$

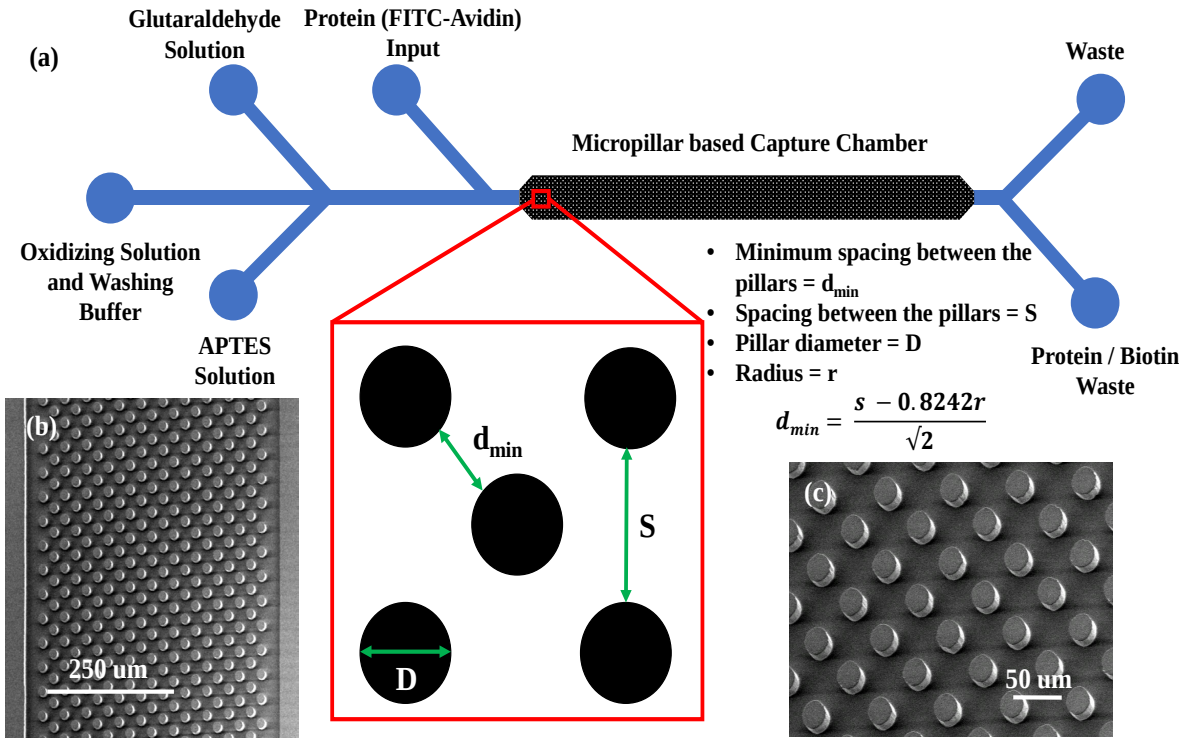

Figure 5.1: Design layout of the affinity-based microfluidic pre-concentration device. The inset shows the unit cell diagram of the arrangement of micropillars

where N is the total number of pillars, r is the radius of the micropillar, S is the spacing between the adjacent micropillars, and d_{min} is the minimum spacing between the micropillars in a unit cell.

The design based on the above mentioned conditions allows minimizing the total pre-concentrator volume to optimize the pre-concentration factor, thus enabling enhanced biomolecular capturing and enrichment efficiency. For a microfluidic device height of $50\mu m$ and minimum unit cell spacing of $10\mu m$, micropillars with a radius (r) of $10\mu m$ and spacing (S) of $23\mu m$ results in the highest increase in the SVR ratio of the device and allowing a $250nl$ volume for the pre-concentration chamber.

5.3 Computational Fluid Dynamic Modeling and Simulations

The sample pre-concentration and filtering is dependent on numerous reciprocating phenomenons including the fluid dynamics, mass transport (convection and diffusion), and molecular binding kinetics. I employed multi-physics model based approach, using the finite element method (FEM) analysis capability of the COMSOL 5.1a environment to design, simulate, and optimize the pre-concentrator microfluidic structure. A 2D multi-physics computational model involving fluid dynamics for mass transport (convection and diffusion) and binding reactions (antigen-antibody reactions in the capture chamber) has been designed. The effects of the input analyte's flow-rate(or velocity), concentration, and microfluidic chip's geometry (e.g., pillar radius, pillar pitch, and channel length) have been investigated.

The mathematical model governing the immunoreactions taking place in a microfluidic environment is determined by the simultaneous analysis of the Navier-Stokes equations, the analyte convection-diffusion equations, and the surface interaction equations of the analyte-ligand binding. The dimensions of the envisioned microfluidic device along with the pressure driven flow mechanism (i.e., Harvard 2000 PHD flow pump) results in a laminar and steady flow through out the device (Reynolds number $\ll 2100$). Moreover, it has been assumed that the fluid flow is Newtonian and incompressible. Therefore, in the proposed/designed microfluidic channel, the flow is modeled with the help of the Continuity and the Naiver-Stokes equations, and can be described using the equations 5.1 and 5.2, respectively.

$$\Delta.\mathbf{u} = 0 \tag{5.1}$$

$$\frac{\partial \mathbf{u}}{\partial t} + \mathbf{u}.\nabla\mathbf{u} = -\frac{\nabla \mathbf{P}}{\rho} + \frac{\mu}{\rho}\nabla^2\mathbf{u} \tag{5.2}$$

where $\mathbf{u}$ is the flow velocity field, $\mathbf{P}$ is pressure (Nm^{-2}), ρ is the density (kgm^{-3}), and

μ is the dynamic viscosity ($Pa.s$).

The spaito-temporal variations of the antigen inside the microfluidic channel are modeled using the convection-diffusion equation as shown in the equation 5.3, whereas the binding interactions between the antigen and the immobilized receptors (i.e., antibodies in my case) in the microfluidic channel are described using the equations 5.4 and 5.5.

$$\frac{\partial c}{\partial t} + \mathbf{u}.\nabla c = D\nabla^2 c \tag{5.3}$$

$$c + R_t \rightleftharpoons B \tag{5.4}$$

$$\frac{\partial B}{\partial t} = k_a c(R_t - B) - k_d B \tag{5.5}$$

where c is the antigen concentration ($mol.m^{-3}$), D is the diffusion coefficient ($m^2 s^{-1}$), R_t is the immobilized receptor's surface density ($mol.m^{-2}$), B is the bound antigen-receptor (i.e., antibodies) complex ($mol.m^{-2}$), k_a is the association rate constant ($M^{-1}s^{-1}$), and k_d is the dissociation rate constant (s^{-1}).

One of the key aspects of the simulation effort is to determine whether the reaction is mass transport-limited or reaction rate-limited. The velocity of the antigen solution in the microfluidic channel is one of the important parameters that determine whether the kinetics of capture of the antigen is mass transport-limited or reaction rate-limited. The capture of the antigen is mass transport-limited if the number of antigen molecules binding per unit of time is sensitive to the flow velocity of the sample in the microfluidic channel, whereas the capture of the analyte is reaction rate-limited if the number of antigen molecules binding to the capture site per unit of time remains similar for different flow velocities. This is followed by calculation of time to saturation of the pre-concentration device to estimate the overall time required for the assay.

Figure 5.2 and 5.3 shows the variation of concentration of the analyte (i.e., "PSA

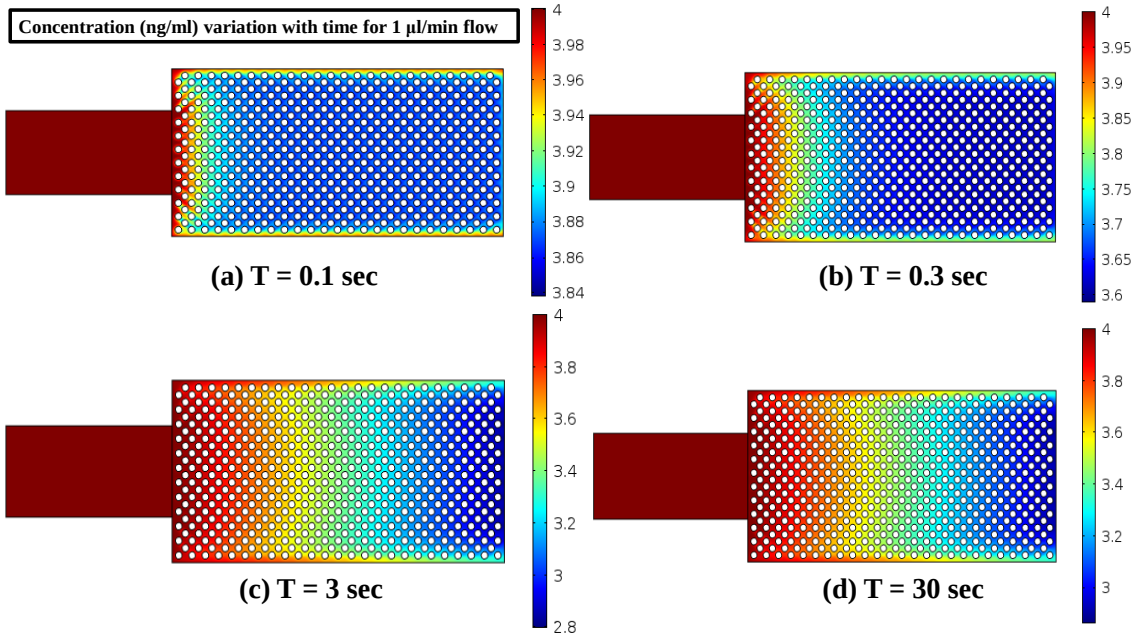

Figure 5.2: COMSOL simulation results for variation in concentration of PSA antigen in the microfluidic chip with input flow of $1\mu l/min$, capture chamber width of $500\mu m$, channel thickness of $50\mu m$ and input analyte concentration of $4ng/ml$.

biomarker protein" used as an example for a biomolecular analyte) in the capture chamber obtained from the reaction kinetics and mass transfer simulations. The input concentration of the analyte C_0 is assumed to be $4ng/ml$ (clinically relevant concentration). The association and disassociation rate constants are assumed to be $k_a = 2.7 * 10^6 M^{-1}s^{-1}$ and $k_d = 2.4 * 10^{-3}s^{-1}$, respectively. The determined affinity constant is $K = \frac{k_a}{k_d} = 10^9 M^{-1}$. These constants are based on binding between the PSA and monoclonal antibody (mAb) [39]. The initial surface concentration for the antibodies coated on the micropillars is assumed to be $C_{S0} = 10 * 10^{-7} mol/m^2$. The bulk diffusion coefficient of the analyte/antigen is assumed to be $D = 1 * 10^{-11} m^2/s$ and the surface diffusion coefficient for the antibodies is taken as $D_S = 1 * 10^{-9} m^2/s$ [39].

It has been observed that for a constant antigen capturing area, the antigen exploitation (capturing and interaction of antigens on the surface of microfluidic channel) increases with the decrease in the input flow velocities as of the insufficient mass transport, which results in increase in reaction time for capturing (fewer antigen molecules are available at

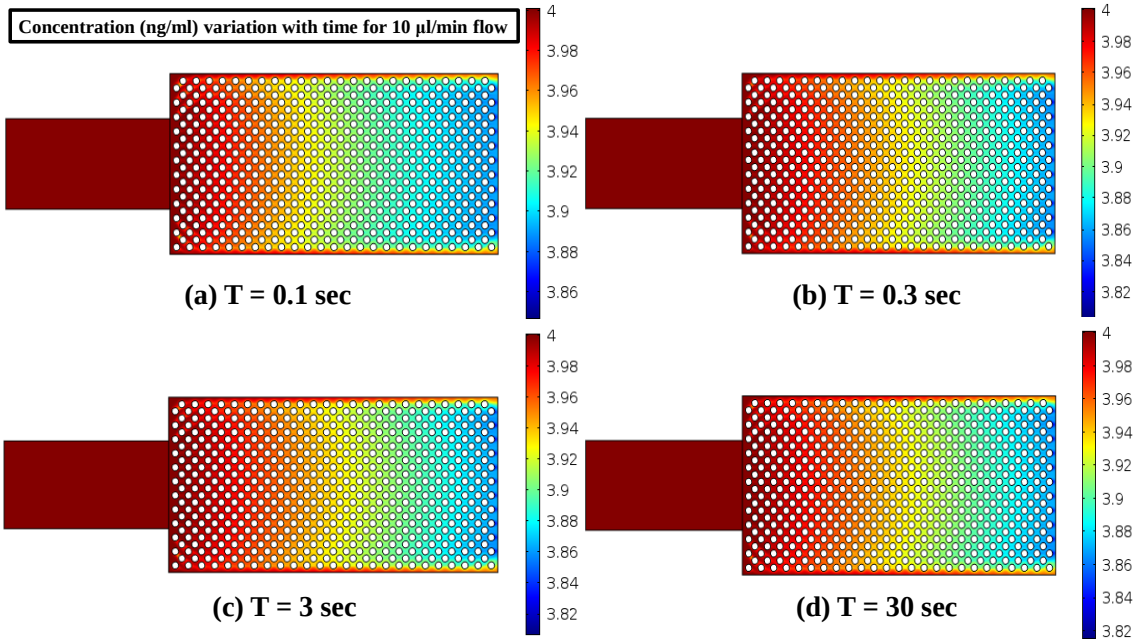

Figure 5.3: COMSOL simulation results for variation in concentration of PSA antigen in the microfluidic chip with input flow of $1\mu l/min$, capture chamber width of $500\mu m$, channel thickness of $50\mu m$ and input analyte concentration of $4ng/ml$.

the capture area per unit time i.e., mass transport-limited regime). In contrast, increased flow rates results in decreased residency time of the antigens over the capture area, resulting in less analyte exploitation and reduced reaction times (i.e., reaction rate-limited regime). Therefore, it is recommended to use higher flow velocities to achieve faster assay time. The simulation results, as shown in figures 5.2 and 5.3, have shown that approximately 70% of the capture chamber has been saturated in 30 seconds for $1\mu l/min$ of the flow rate of antigens, while $\sim 95\%$ of the capture chamber is saturated for $10\mu l/min$ of flow rate for the antigens.

Another challenge of optimization lies with the sample concentrations. The clinical samples require quantification of concentrations of $\ll$ 10 pM. The generation of antigen binding response from such small concentrations results in a constraint on minimum antigen exploitation. The kinetics of mass transport and reaction transport affects the assay process for lower concentration in a similar fashion. Therefore, it is recommended to increase the incubation time for the sample along with using higher flow rates to yield measurable

results.

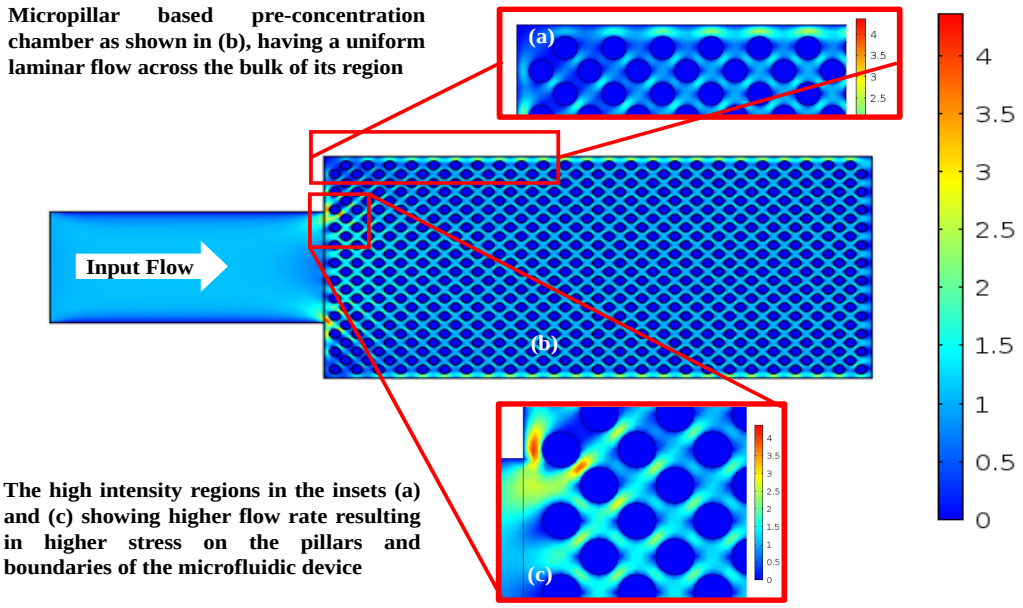

Figure 5.4: The figure shows COMSOL flow simulation results for the designed microfluidic pre-concentrator device. The high intensity regions in the insets (a) and (c) showing higher flow rate resulting in higher stress on the pillars and boundaries of the microfluidic device. The micropillar based pre-concentration chamber shown in (b) reveals a uniform laminar fluid flow across the bulk of its region.

Figure 5.4 shows the simulation results for the designed pre-concentrator microfluidic chip consisting of a PDMS based capture chamber with micropillars of $10\mu m$ radius, vertical height of $50\mu m$, and center-to-center spacing of $43\mu m$ between adjacent pillars. The width of the capture chamber is $500\mu m$. It has been observed that almost uniform flow velocity appears across the length of the microfluidic device. The micropillars immediately adjacent to the inlet channel and the ones along the microfluidic device boundaries, face the highest values of the fluid velocity. This corresponds to higher shear rates, and as a consequence higher shear stress across these positions. It has also been observed that the micropillars in the pre-concentrator chips with wider capture chambers (i.e., $1000\mu m$ and $2000\mu m$), have experienced much smaller shear stress values for similar flow rates as compared to the ones with capture chambers having smaller widths such as $500\mu m$. Extremely high shear rates result in decreased capture efficiency and denaturing of the biomolecules

such as proteins [175]. Moreover, higher shear rates and pressures also result in leaking and delamination of the microfluidic devices [176]. An optimal value of input flow rate is thus desired to achieve a balance between the microfluidic pre-concentrator device's capturing efficiency and the throughputs (i.e., the assay time and the total input sample volume). To evaluate performance of other affinity interaction such as Biotin-Avidin, IgG - anti-IgG antibodies, similar approach can be employed with respective parameters.

It has also been observed that when the thickness of the capture chamber is doubled, the amount of captured antigen is also doubled, for the same input flow velocity. Higher flow-rates can be achieved using wider microfluidic chips (e.g., $1000\mu m$ and $2000\mu m$), but at an expense of having higher total pre-concentrator volume. In this research, we have considered $1cm$ long capture chamber, with the width of widths of $500\mu m$ having input flow velocities ranging between $1\mu l/min$ to $10\mu l/min$. The simulations are only performed for $1mm$ length because of the computational hardware constraints.

5.4 Experimental Methods

5.4.1 Materials

The silane reagents (3-aminopropyl) triethoxysilane (APTES) and (3-Mercaptopropyl)-trimethoxysilane has been purchased from Sigma-Aldrich. Anhydrous 2-Propanol solution ($\geq$ 99% pure), Glutaraldehyde solution, Phosphate Buffer Saline (1X-PBS, pH 7.4), FITC-Avidin protein, N,N-Dimethylformamide (DMF), Ethanolamine, Sodium periodate, Sodium Acetate, Sodium Cyanoborohydride, and N,N-Dimethylformamide has been purchased from Sigma-Aldrich, US. Avidin from egg white has been purchased from Thermofisher scientific, US, while PC-biotin-PEG3-NHS-ester has been obtained from Click Chemistry Tools, US. Mouse monoclonal anti-PSA IgG antibody (10C-CR2051M5) and human lyophilized PSA (free-PSA (f-PSA) from human source) has been purchased from Fitzgerald Industries. Unconjugated Sambucus Nigra Lectin (SNA), Unconjugated Maackia Amurensis Lectin (MAA-MAL II) and CY5 labeled SNA lectin has been pur-

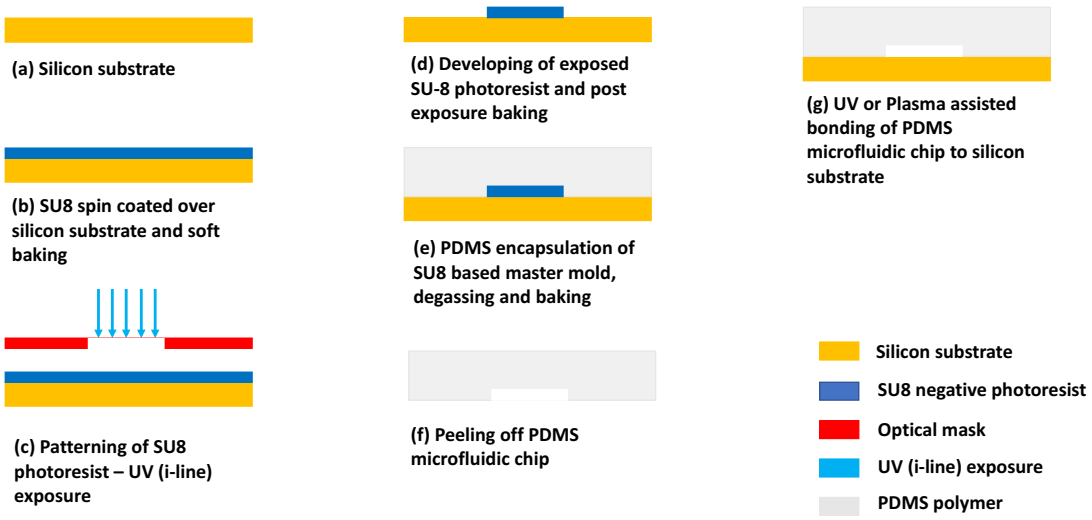

Figure 5.5: Schematic showing fabrication steps for the affinity-based microfluidic preconcentration device

chased from Vector Labs, while unconjugated MAA-MAL II lectin has been purchased from BioWorld. ELISA Synblock blocking buffer has been purchased from BioRad. Silicon wafers has been procured from WaferPro, US, while the Glass wafers has been procured from University Wafers, US. SU-8 2035 and SU-8 developer has been purchased from MicroChem, US. Sylgard 184 (PDMS by Dow Corning Corporation) and the curing agent has been purchased from Ellsworth Adhesives, US. The transparency masks has been developed and purchased from CAD/Art Services, US. All other equipment and cleaning solutions has been provided at the IEN cleanroom utility of the Georgia Institute of Technology, Atlanta, US.

5.4.2 Microfluidic chip fabrication

The PDMS microchips are fabricated using the soft lithography technique [35]. SU-8 2035 negative photoresist is spin coated over the silicon wafers to achieve a uniform thickness of $50\mu m$. The spin coated wafer is then soft baked for 3 minutes at 65°C, and cooled down.

The pre-concentrator pattern is then defined by exposing the SU-8 in MA-6 mask aligner setup with UV light (i-line, λ = 365nm), using transparency masks). A post exposure bake for 3 minutes at 65°C and 5 minutes at 90°C is performed. The wafer is then developed in SU-8 developer (purchased from MicroChem, US) for 3 minutes, washed using IPA, dried using nitrogen gas, and inspected using microscope and profilometer. Once the master mold is made, it is silanized using (3-Mercaptopropyl)trimethoxysilane in a vacuum desiccator for 12 hours.

Sylgard 184 base and the curing agent are thoroughly mixed in 10:1 ratio, respectively. The mixture is then poured over the silanized master template in a plastic petri dish and degassed using vacuum desiccator for 6 hours. Once degassed, the PDMS is placed in an oven at 65°C for 4 hours for curing. The cured PDMS mold is peeled off the master mold using a razor blade and punch through holes are made for the fluid inlet. The PDMS mold is then cleaned using IPA, dried using nitrogen gas, and placed in the UVCOS (UV-Ozone cleaning system) system for 10 minutes along with the glass or silicon substrate. After 10 minutes, the PDMS is taken out and carefully placed on the substrate, slightly pressed, and heated for 30 minutes on a hotplate at 65°C to ensure bonding. Once the bonding is complete, tubing, and connectors are attached to have inlet and outlet for the microfluidic chip.

The microfluidic chips are tested for flow leakage and clogging after the bonding process. Phosphate Buffer Saline (1X-PBS, purchased from Thermofisher Scientific, US) solution (pH 7.4) has been flown at different flow rates ranging from $0.1\mu l/min$ to $30\mu l/min$. Perfect flows of PBS without any leakage and clogging has been observed in the microfluidic chip.

Two different designs for microfluidic chips are fabricated. The designs consists of a simple $50\mu m$ deep rectangular pre-concentration chamber with width and length of $500\mu m$ and $1cm$, respectively. The first design is a simple rectangular channel (no micropillars), while the second design consists of a hexagonal array of $20\mu m$ diameter micropillars, hav-

ing a minimum spacing of $10\mu m$ among them. Figure 5.5 shows the steps involved the fabrication and testing of the microfluidic chip.

5.4.3 Silanization protocol

The microfluidic chip is initially purged with the 1X-PBS solution (pH 7.4) to remove the trapped air bubbles. Once the air is removed, oxidizing solution containing hydrogen peroxide (H_2O_2), hydrochloric acid (HCl), and water (H_2O) (1:1:5) is flowed for 15 minutes at $10\mu l/min$ ($10\mu l/min$ flow is used throughout the experiments unless stated otherwise). The microfluidic chip is then rinsed with 1X-PBS solution, followed by the flow of silanization solution (5% APTES in 2-Propanol(v/v)) for 15 minutes, and a 2-Propanol rinse. The microfluidic chip is then baked at 80°C for 30 minutes in an oven and rinsed with 1X-PBS solution for 5 minutes.

5.4.4 Glutaraldehyde functionalization and Avidin immobilization

A 2.5% glutaraldehyde solution in 1X-PBS (v/v) is flowed through the APTES modified microfluidic chip for 15 minutes, followed by 30 minutes of incubation at room temperature. The microfluidic chip is then rinsed with 1X-PBS solution for 5 minutes. Avidin solution is flowed through the microfluidic chip for 30 minutes, followed by incubation at room temperature for 30 minutes to have a uniform Avidin adsorption over the walls and micropillars in the pre-concentration chamber. The microfluidic chip is then rinsed using 1X-PBS solution to remove the unattached Avidin.

5.4.5 Quantification of capture efficiency

Avidin is a tetrameric biotin-binding protein with an estimate size of 66-69 kDa. I used FITC-tagged Avidin to quantify the attachment of Avidin to the glutaraldehyde modified surface and estimate the biomolecular capture efficiency of the fabricated microfluidic devices. A stock solution of $100\mu g/ml$ of FITC Avidin in 1X-PBS has been prepared and

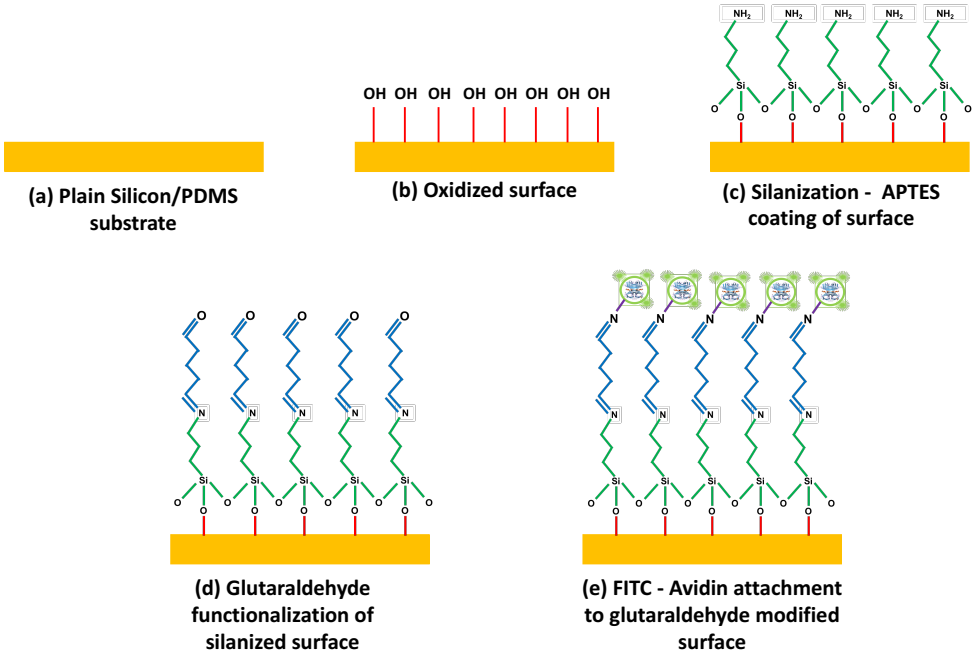

Figure 5.6: Schematic showing surface functionalization for quantification of Avidin capture efficiency

ten different solutions of FITC Avidin (with 10 fold dilutions) are flowed through the microfluidic chips for 30 minutes. The microfluidic chip is incubated at room temperature for 30 minutes to have a uniform Avidin adsorption over the walls and micropillars in the pre-concentration chamber. The microfluidic chip is then rinsed using 1X-PBS solution to removed the unreacted FITC-tagged Avidin. The fluorescence intensity of the microfluidic devices is then measured to monitor the capture efficiency of the affinity based pre-concentration devices. The figure 5.6 shows a pictorial representation of surface functionalization for quantification of Avidin capture efficiency.

5.4.6 Results and Discussions

The figure 5.7 shows the actual results obtained for FITC-Avidin capture efficiency quantification using simple and micropillar based microfluidic pre-concentration devices. Five different concentrations of FITC-Avidin has been used (i.e., 0.01, 0.1, 1, 10 and 100 ng/ml) for the analysis. All the images and the baseline data are obtained using constant exposure

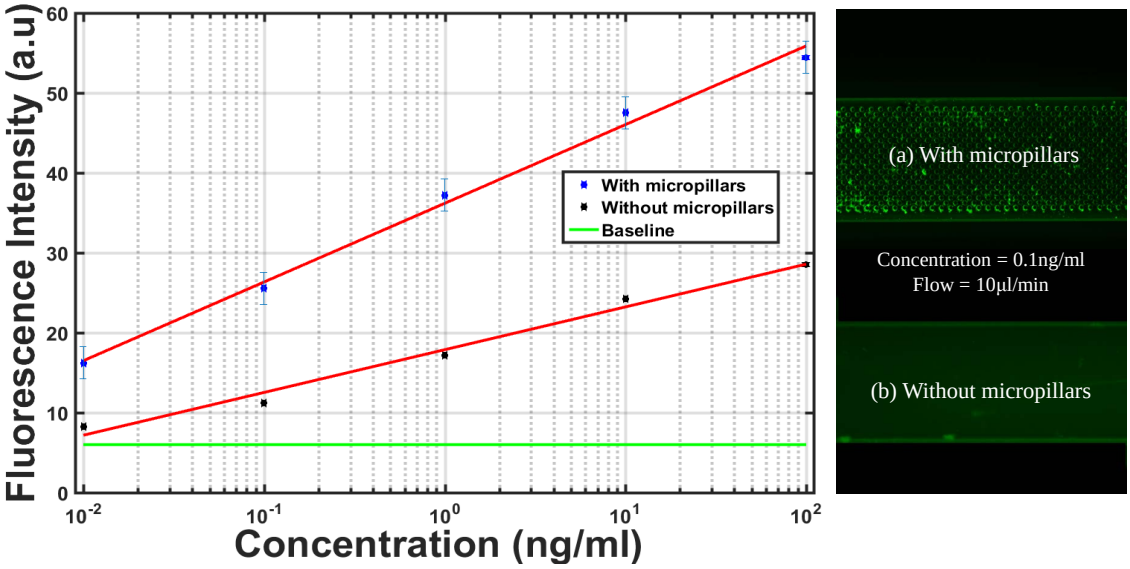

Figure 5.7: Actual results showing enhancement of Avidin capture with and without micropillars for a $500\mu m$ wide microfluidic channel. A plot showing variation of fluorescence intensity (a.u) against FITC Avidin concentration (ng/ml) (a) Fluorescence image for FITC-Avidin ($0.1ng/ml$) capturing in a micropillar based pre-concentration device (b) Fluorescence image for FITC-Avidin ($0.1ng/ml$) capturing in straight microfluidic channel based device.

to the microfluidic devices using "Zeiss Axio-Observer Z1" fluorescent microscope. An intensity enhancement of ~ 2 times has been observed showing enhanced affinity based biomolecular capturing with the introduction of micropillars in the simple channel based microfluidic devices.

5.5 Affinity-based analyte pre-concentration and detection

My scheme for biomolecular (protein biomarker) filtering and pre-concentration is based on an affinity-based approach, for which I have developed an affinity-based multi-step surface functionalization protocol to optimize the surface coverage and capturing efficiency of the biomolecules. The surface of the pre-concentrator chip is first functionalized with the Avidin molecules (as explained earlier). Antibodies-enhanced affinity probes are then

employed to selectively capture the desired biomolecules from the sample. Specifically tailored antibodies has been extensively used in the literature for highly selective and specific affinity-based capturing of the biomolecules in a high background noise environment [177], [178]. I have employed one such biomolecule specific antibody i.e, anti-PSA IgG antibody and tailored it accordingly, such that it not only acts as my affinity-based biomolecular capturing probe but also provides me with an ability to release the captured biomolecules on demand.

To alleviate the challenges associated with the traditional affinity-based protein purification techniques such as sample degradation, introduction of contaminants (due to the release of non-specifically bound proteins), and elution of endogenous proteins (along with the desired protein) [23] (as elaborated earlier in chapter 2), I used a photo-cleavable (PC) biotin-PEG3-NHS-ester linker for tailoring and immobilizing my antibody affinity probes for the capture of the target biomolecules on the Avidin coated pre-concentrator chip. The biotinylated PC-linker is conjugated with the desired antibodies, purified to removed the excess biotinylated PC-linker molecules, and finally immobilized on the pre-concentrator chip' surface through the Biotin-Avidin binding. After applying the PC-linker based surface chemistry, the target antigens are captured by the affinity-based immobilized antibodies. The captured antigens can then be released on demand through an efficient photocleavage mechanism using UV light exposure at 300 - 380 nm wavelength [179]. Figure 5.8 shows a pictorial representation and working of the PC-biotin-PEG3-NHS ester.

5.5.1 Immuno-affinity assay for enhanced biomolecular pre-concentration and detection

Enzyme-linked immunosorbent assay (ELISA) has been extensively used for the detection and quantification of the biomolecules and antigens such as proteins, peptitdes, hormones, viruses, etc. [180],[181]. In additions to these, ELISA has also been employed for glysosylation analysis of proteins [182],[183]. A modified version of ELISA employing lectins (i.e., Enzyme linked lectin assay - ELLA) and antibodies for glycoprofiling has been devel-

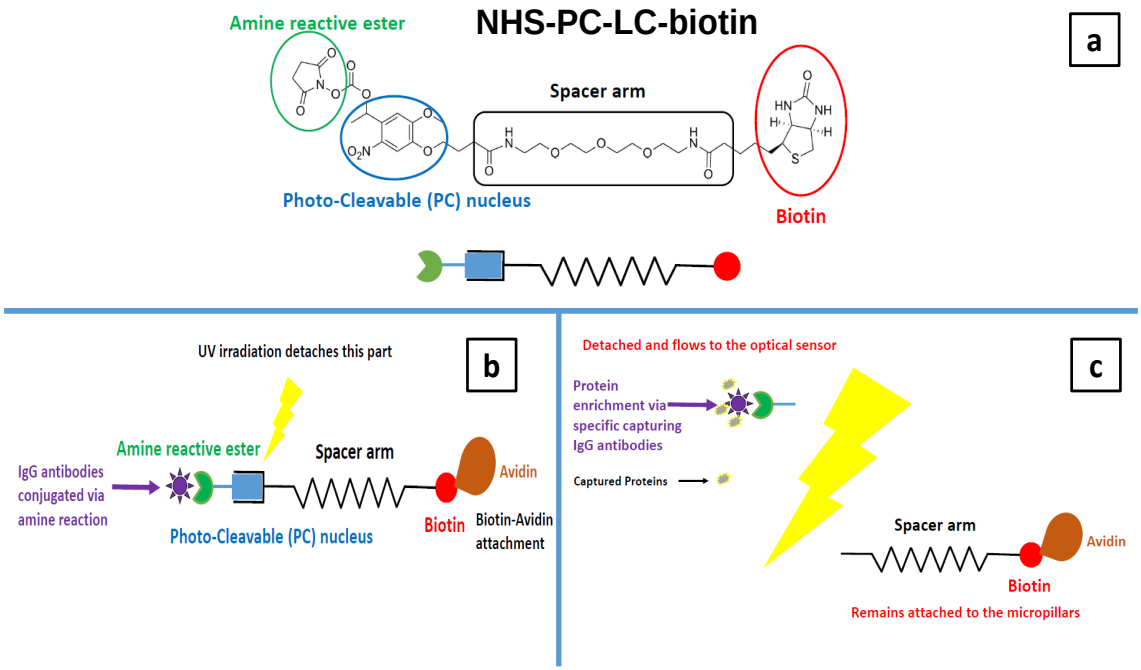

Figure 5.8: (a) Schematic of NHS-PC-LC(or PEG3)-biotin linker molecule (b) Behavior of NHS-PC-LC-biotin affinity probe. Attachment to Avidin surface and IgG antibodies conjugation with the amine reactive part (c) Post UV exposure behavior of the NHS-PC-LC-biotin affinity probe.

oped [184],[185]. Since, most of the FDA approved cancer biomarkers are glycosylated, the use of ELLA based technique for cancer biomarker detection can be extremely efficient but compared to the ELISA technique, ELLA has not been widely exploited by the researchers. It is perhaps owing to the complexity of interactions associated with lectins and glycans (carbohydrates) and the intricate nature of the glycosylated proteins [164],[184]. One of the key challenges associated with ELLA is that the lectins measure the presence of corresponding glycans on all the available substances in the sample, including the proteins of interest. Moreover, the antibodies employed the ELLA, especially the polyclonal antibodies are heavily glycosylated [164],[186]. This results in high background noise and spurious readings, undermining the benefits reaped by the pre-concentration of the desired glycan proteins (i.e., cancer biomarkers) for enhanced biomolecular detection [184]. I have designed and modified an immuno-affinity based assay approach for biomolecular pre-concentration and detection. The key component to my approach is the use of the PC-

biotin-PEG3-NHS linker and its conjugation with the desired antibodies for biomolecular capturing, detection, and release. The PC-biotin-PEG3-NHS-ester linker has a unique PC moiety (1-2 (nitrophenyl)-ethyl) attached to the biotin part through the PEG3 spacer arm, separating the biotin from the NHS portion. The NHS-ester portion reacts specifically with primary amine groups of the specific probe molecules (i.e., anti-PSA IgG antibody) to form a carbamate linkage [187]. The biotin portion binds to the Avidin modified surface (i.e., silicon or glass substrate) and the PDMS (walls and micropillars)). I modified the existing ELLA procedure to extract advantages of both the affinity-based pre-concentration and the highly specific glycoprofiling capability provided by the ELLA. I specifically oxidized the carbohydrates moieties present on the capture antibodies before conjugating them with the PC-biotin linker. This selective deglycosylation of the capture antibodies drastically reduces the non-specific attachment of the lectins, allowing me to exploit the benefits of the affinity-based pre-concentration and lectin enhanced glycoprofiling of the biomolecules. Here, I present my protocol for the conjugation of PC-linker with the antibodies, surface functionalization of the pre-concentration chamber with the conjugated complex, and capturing and release of the desired biomolecules.

Deglycosylation and oxidation of the antibodies

Mouse monoclonal anti-PSA IgG antibody (10C-CR2051M5) has been obtained from Fitzgerald, US. Sodium azide is first removed from the obtained antibodies with the help of a micro-centrifuge device ((Amicon 0.5ml Ultra, 100kDa MW cutoff, 1000g), followed by reconstitution of the antibodies in the 100 mM of sodium acetate solution (pH 5.5) at a final concentration of $2mg/ml$. The antibodies are then oxidized using sodium periodate to remove the associated carbohydrate moieties. 20 mM sodium periodate solution is prepared using 100mM of sodium acetate buffer and $1ml$ of the solution is added to $1ml$ of the reconstituted antibodies. The solution is placed in dark for 2 hours at 4°C for the oxidation reaction to take place. The oxidized antibodies solution is then desalted using the micro-

centrifuge devices and reconstituted in 1X-PBS solution (pH 7.4) to a final concentration of $5mg/ml$.

Antibodies and PC-linker conjugation protocol

The PC-biotin-PEG3-NHS-ester and the oxidized anti-PSA IgG antibody are conjugated together to develop the affinity probe for the PSA biomolecular enrichment and filtration. $1mg$ of PC-biotin-PEG3-NHS-ester is dissolved in $119\mu l$ of DMF just before use. $26.6\mu l$ of the solution is then added to the oxidized antibodies solution (having a volume of $1ml$), followed by incubation on ice for 2 to 3 hours. After the incubation, the excess PC-biotin-PEG3-NHS ester is removed using the 0.5 ml micro-concentrator vials (Amicon 0.5ml Ultra) using a micro-centrifuge device (1000g, 100kDa MW cutoff, 30 minutes), followed by reconstitution of the solution using 1X-PBS solution (pH 7.4) to a final volume of $1ml$. $10\mu l$ of 5M sodium cynaoborohydride solution is then added to $1ml$ of the biotinylated oxidized antibodies solution to stabilize the Schiff base formed between the amines and the aldehydes moieties. The reaction is allowed to take place for 30 minutes. Once completed, $50\mu l$ of 1M ethanolamine (ETA or MEA) solution has been added to the $1ml$ solution to block the unreacted aldehyde sites. The reaction is again allowed to take place for 30 minutes, followed by desalting using the micro-centrifuge, and reconstitution of the solution in 1X-PBS (pH 7.4).

Surface functionalization of the pre-concentrator chip with the PC-affinity probes

The oxidized biotinylated-PC anti-PSA IgG antibody solution is diluted to $100\mu g/ml$ and then flowed in the microfluidic chip for 10 minutes. The chip is then incubated at room temperature for 30 minutes. The process is repeated three times to have a uniform adsorption of the antibodies across the PDMS based pre-concentration chamber. The unabsorbed antibodies are then removed using 1X-PBS rinse. Synblock blocking solution of is then flowed for 10 minutes and the chip is incubated for 30 minutes at room temperature to

prevent any non-specific adsorption.

Capturing and release of PSA cancer biomarker

The capturing and pre-concentration performance of the functionalized pre-concentration microfluidic chip is evaluated using the human lyophilized PSA (from human source, purchased from Fitzgerald, US). Five different concentrations of the PSA with 10-fold dilutions (i.e., 0.01, 0.1, 1, 10, and 100 ng/ml), in PBS buffer solution are flowed through the corresponding microfluidic pre-concentration devices for 10 minutes, followed by 30 minutes of incubation. The unattached PSA has been rinsed using 1X-PBS solution. A solution containing $100\mu g/ml$ of FITC-tagged MAA-II lectin and Cy5-tagged SNA lectin in 1X-PBS (pH 7.4) has been used to quantify the capturing and pre-concentration of PSA. The lectin solution is then flowed in the microfluidic capture chamber for 10 minutes. The chip is then incubated at room temperature for 30 minutes (in dark environment wrapped in aluminum foil). The chip is rinsed with 1X-PBS for 5 minutes and imaged for fluorescence measurements. Once fluorescence is observed, the chip is placed under a UV lamp (MJB4 Mask Aligner Lamp, $10mW/cm^2$ intensity, distance of 5cm) for 10 minutes. After the exposure, the chip is rinsed using 1X-PBS solution for 30 minutes (flow rate of $5\mu l/min$) and the fluorescence intensity is recorded.

Results and discussion

The change in carbohydrate structure of the PSA biomarker plays an important role in the glycoprofiling of PSA for PCa detection. One of the most prominent aberrations in the carbohydrate structure of the PSA is the sialylation in linkage of sialic acid from α-(2,6) linkage to α-(2,3) linkage during the PCa progression. This aberration in the glycoprotein structure of the PSA can predict the presence of a pathological process and in some cases the stage of the process as well [188]. It has been observed that the PCa patients have a significantly increased presence of α-(2,3)-linked sialic acid in the serum free-PSA (fPSA)

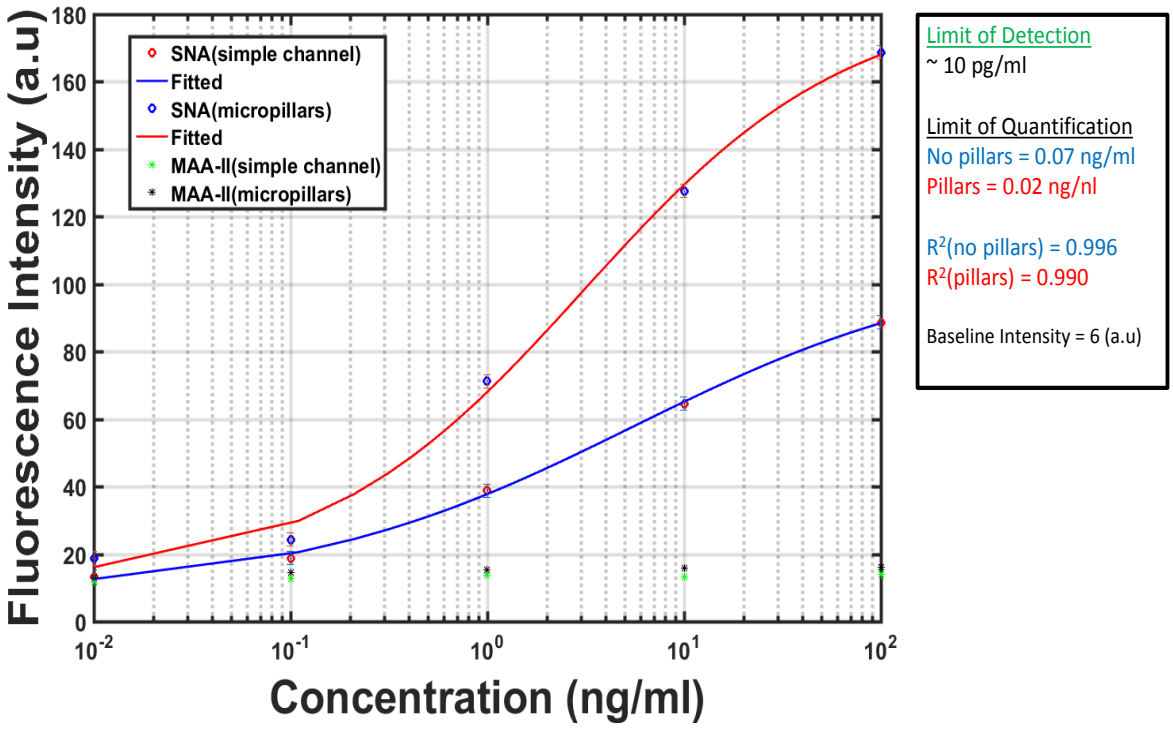

Figure 5.9: Actual results showing PSA capture with and without micropillars for a $500\mu m$ wide microfluidic channel. The four point fitted curves showing variation of fluorescence intensity for multiplexed PSA sensing using Cy5-tagged SNA lectin and FITC-tagged MAA-II lectin for different concentrations (ng/ml) of PSA

[188],[189]. It has also been observed that the PCa patients have a significantly lower presence of the -(2,6)-linked sialic acid in the serum fPSA, when compared to the BHP patients [188],[189].

The binding of PSA with different lectins has been reported in [190]. Among the employed lectins, the SNA lectin provides one of the highest affinity to the PSA and revealed preferential binding to the terminal α-(2,6)-linked sialic acid of the PSA [188],[189]. It has been reported in the literature that PSA from the PCa patients revealed significant binding to the MAA-II lectin when compared to the PSA from the BHP patients [188],[189]. It has also been observed that both the α-(2,3)-linked, and α-(2,6)-linked sialic acid are expected in all the PSA samples. However, the ratio of α-(2,3)-linked to α-(2,6)-linked sialic acid is enhanced for the PCa patients.

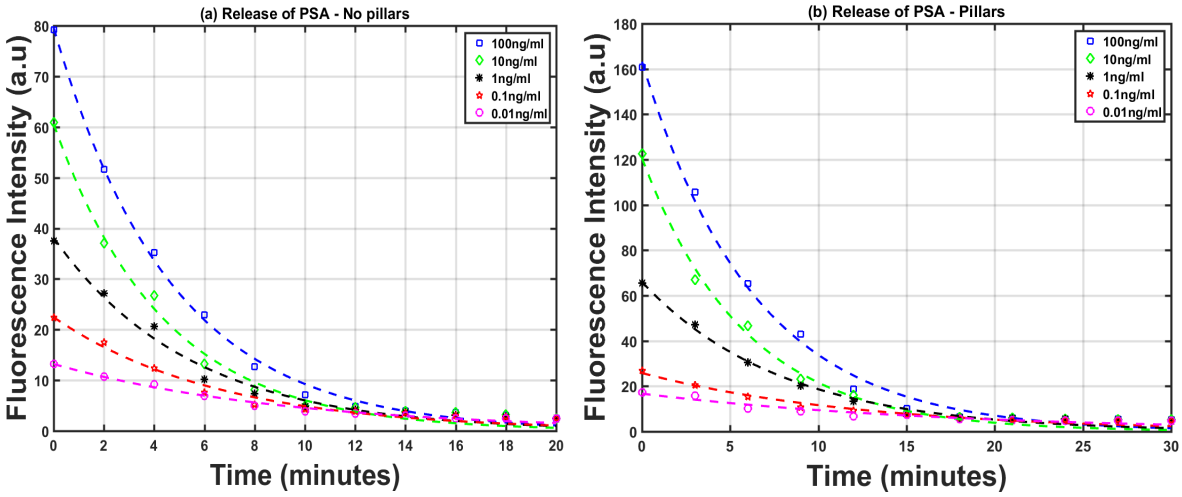

Figure 5.10: Actual results showing PSA release with time from microfluidic devices. (a) Fluorescence intensity variation with time for rectangular microfluidic devices. (b) Fluorescence intensity variation with time for micropillar based microfluidic devices. The curves are fitted to the measured results using exponential fitting function. The curve fitting processing has been performed using in-house developed MATLAB code.

The commercially available non-malignant f-PSA is reported to have high concentration of α-(2,6)-linked sialic acid, while only trace amounts of α-(2,3)-linked sialic acid is present [188],[189]. This allows the MAA-II lectin to be employed as a negative control for commercial fPSA obtained from healthy subjects (as no interaction is expected), while at the same time can be employed for the detection of PSA from PCa patients.

I have employed both the SNA (Cy5-tagged) and MAA-II (FITC-tagged) lectins to demonstrate an on-chip multiplexed PSA glycoprofiling. Commercial fPSA (obtained from healthy subjects) has been used for the experiments. The fluorescence intensity has been measured to estimate the binding of the lectins to the PSA. The figure 5.9 shows the obtained fluorescence intensity results for the on-chip multiplexed PSA glycoprofiling in the simple PDMS microfluidic channels and PDMS micro-pillar based affinity preconcentrator devices. The fluorescence intensity measurements for the Cy5-tagged SNA lectin has shown considerable increase with the increase in PSA concentration, showing

binding of the SNA lectin to the PSA. However, extremely weak fluorescence signals has been observed for the FITC-tagged MAA-II lectin showing negligible binding of the MAA-II lectin to the PSA. These results are in agreement with the works in the literature as mentioned earlier [188],[191].

The calibration curve has been constructed by plotting the obtained fluorescence data with respect to the PSA concentration and fitting the points to a four parameter curve (or Hill's dose-response curve given as $y = y_0 + (y_{max} - y_0)c^n/(c_n + K_d^n)$ where c is the concentration of the antigen, K_d is the dissociation constant of the dose response). The four parameter curve is given as

$$Y = B + (A - B)/(1 + (x/C)^D) \tag{5.6}$$

where A is the maximum fluorescence intensity obtained for the maximum PSA concentration, B is the minimum fluorescence intensity obtained to the minimum PSA concentration, C is the concentration producing 50% of the fluorescence intensity, and D is the slope at the inflection point of the sigmoidal curve.

The LOD for each of the devices i.e., simple microfluidic channels and micro-pillar based pre-concentration devices has been calculated to be the concentration when the average fluorescence response from the blank experiment (no PSA flowed in the device) plus 3 times the standard deviation from that blank measurement. The figure 5.9 shows the obtained fluorescence reading for the experiment. The four point curve fitted data obtained shows increased fluorescence for the micropillar based microfluidic devices compared to the simple microfluidic channels, showing enhanced PSA preconcentration capability of the micropillar based devices. The linear working range is $\sim 0.1ng/ml$ to $\sim 50ng/ml$ for both of the devices, with both allowing LOD of $\sim 10pg/ml$. This lies well within the clinical concentration regime for the PSA detection i.e., $1ng/ml$ to $10ng/ml$. I defined the "Limit of Quantification" (LOQ) as ten times the intensity of the blank signal, to have reliable information for multiplexed detection of PSA with the designed devices. It has been

observed that the incorporation of micropillars have decreased the LOQ to $0.02ng/ml$ from $0.07ng/ml$, resulting in $\sim$ 3.5 times enhancement in the minimum quantifiable range for PSA detection. The working range of both of the devices is atleast 10 orders of magnitude higher compared the commercially available ELISA kit for the PSA (i.e., $0.01ng/ml$ to $12ng/ml$ for fPSA ELISA kit [192]). It should be noted that the commercially available kits have propriety paired antibodies, detection tags, and materials which are specifically modified for the given test.

Figure 5.10 shows the release of captured PSA from the microfluidic devices. The fluorescence intensity variation with time has been shown in 5.10(a) and 5.10(b). It has been observed that $\sim$ 10 minutes are required to release the PSA sample from the simple rectangular microfluidic devices, while $\sim$ 20 minutes are required to release the PSA sample from the pillar based devices.

5.6 Conclusion

I have demonstrated biomolecular (i.e., proteins and biomarkers) filtering and pre-concentration based on an affinity-based separation approach. The target biomolecules are captured and pre-concentrated on the PDMS-based micropillars. The micropillar's surface is specifically functionalized with the specific affinity epitopes corresponding to the biomolecules for enhanced affinity-based capturing. The pre-concentrated biomolecules are then released on demand and can be recaptured on a sensing transducer (e.g., optical sensor arrays), allowing a complete label-free sensing and profiling (secondary epitopes such as glycoforms) of the biomolecules.

I demonstrated a multi-step surface functionalization protocol to optimize on-the-flow surface functionalization and capturing efficiency of the biomolecules in a PDMS-based microfluidic platform. I designed, optimized, fabricated, and characterized a PDMS-based microfluidic platform, having a micropillar based biomolecular pre-concentration chamber allowing increased surface-to-volume ratio (SVR) for enhanced biomolecular filtering and

preconcentration. The surface of the pre-concentrator chamber is functionalized with the Avidin protein, followed by the use of a biotinylated photo-cleavable (PC) linker conjugated with the biomolecular specific antibodies (i.e., anti-PSA IgGs). The use of PC-biotin linker is the key towards solving the challenges such as sample degradation, introduction of contaminants (due to the release of non-specifically bound proteins), and elution of endogenous proteins (along with the desired protein) [23], faced while releasing the pre-concentration samples from microfluidic devices.

I effectively demonstrated the capture and release of IgG proteins (from Rabbit serum) and PSA cancer biomarkers (fPSA, human serum) using the PC-biotin linker with clinically relevant sample concentrations and volumes. I also demonstrated the capability of multiplexed glycoprofiling for elucidating the PTMs of the PSA cancer biomarker using the SNA and MAA-II lectins. A dynamic working range of $\sim$ 10 orders of magnitude higher compared the commercially available ELISA kit for PSA detection (i.e., $0.01ng/ml$ to $12ng/ml$ for fPSA ELISA kit [192]), has been achieved using the designed PDMS-based micropillar pre-concentration platform. Overall, a minimum LOD of $\sim 10pg/ml$ and a LOQ of $\sim$ $20pg/ml$ has been been achieved for on-chip multiplexed PSA pre-concentration, detection, and glycoprofiling.

CHAPTER 6
CARBON NANOTUBES AS NANOPOROUS ELEMENTS FOR MIRCOFLUIDIC PRE-CONCENTRATION AND FILTERING

6.1 Introduction

In this chapter, I present the use of carbon nanotubes (CNTs) as high porosity material for enhanced on-chip biomolecular pre-concentration applications. I fabricated and utilized vertically aligned (VA-MWCNTs) forests and micropillar structures over a silicon substrate to increase the effective surface area of a microfluidic pre-concentrator device. These MWCNTs are taken as an alternate to the PDMS micropillars based pre-concentration platform, can be vertically grown with high porosity, and high aspect ratio [193], resulting in much larger surface areas for target analyte capturing, pre-concentration, and filtering.

The MWCNT forests and micropillars has been grown over a silicon substrate, aligned, and bonded with the PDMS based microfluidic channels to develop the biomolecular pre-concentrator and filtering devices. The envisioned and designed MWCNT-based biomolecular pre-concentrator platform provides enhanced capture area and smaller effective volume in the biomolecular capture chambers of the PDMS-based microfluidic devices, allowing enhanced biomolecular capturing and pre-concentration. The capturing efficiency and performance of these designed MWCNT forests and micropillar-based pre-concentration platforms has been assessed by employing the surface chemistry protocols and fluorescence microscopy techniques as elaborated in the earlier chapters.

6.2 Fabrication of Carbon Nanotube Forests and Micropillars

Plain silicon wafers has been used as the carrier substrate for the growth of MWCNTs. The wafers are ”piranha” cleaned using the standard 3:1 $H_2SO_4 : H_2O_2$ solution. The cleaned

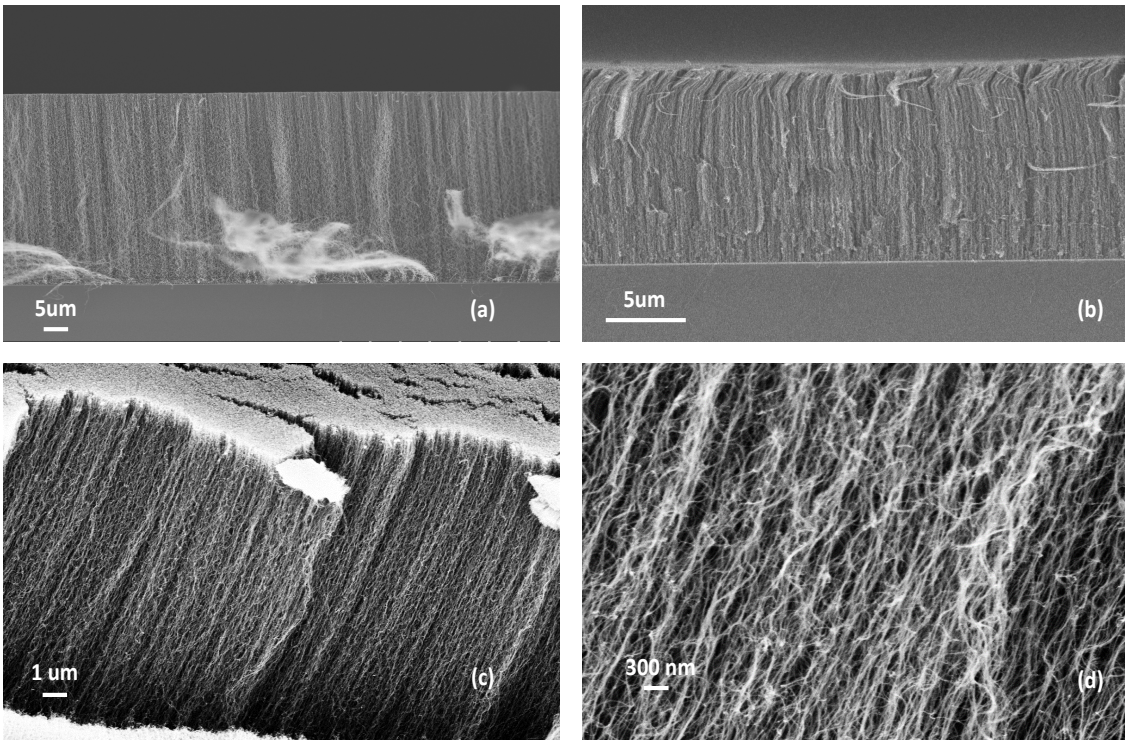

Figure 6.1: The figure shows SEM images of the vertically grown MWCNTs structures (forests) (a) Cross-sectional image of the grown MWCNTs with a growth time of 300 seconds having a measured height of $\sim 30\mu m$ (b) Cross-sectional image of the grown MWCNTs with growth time of 180 seconds having a measured height of $\sim 18\mu m$ (c) Vertically grown dense MWCNT structures (MWCNT forests) (d) High magnification image of MWCNTs showing highly dense growth MWCNTs with estimated individual MWCNT width of ~ 8 to $12nm$. $1.1nm$ of Fe catalyst has been used for the growth of these forests.

wafers are dried using nitrogen gas and are baked in an oven for 30 minutes at $100°C$ to remove any moisture content. A $200nm$ layer of silicon oxide SiO_2 is deposited over the clean and dried silicon sample, followed by evaporation of $10nm$ of Aluminum oxide (Al_2O_3) and $1.1nm$ of Iron (Fe), using the e-beam evaporator tool (Denton e-beam evaporator). The SiO_2 layer acts as an insulation layer and also allows adhesion of the Al_2O_3 to silicon sample surface. The Fe acts as a catalyst by forming nanoparticle enhanced nanoislands at high temperatures over the porous Al_2O_3, for the growth of vertically aligned MWCNTs [142].

The MWCNTs have been grown using the root growth mechanism, employing the low pressure chemical vapor deposition (LPCVD) process in the "Axitron Black Magic reactor"

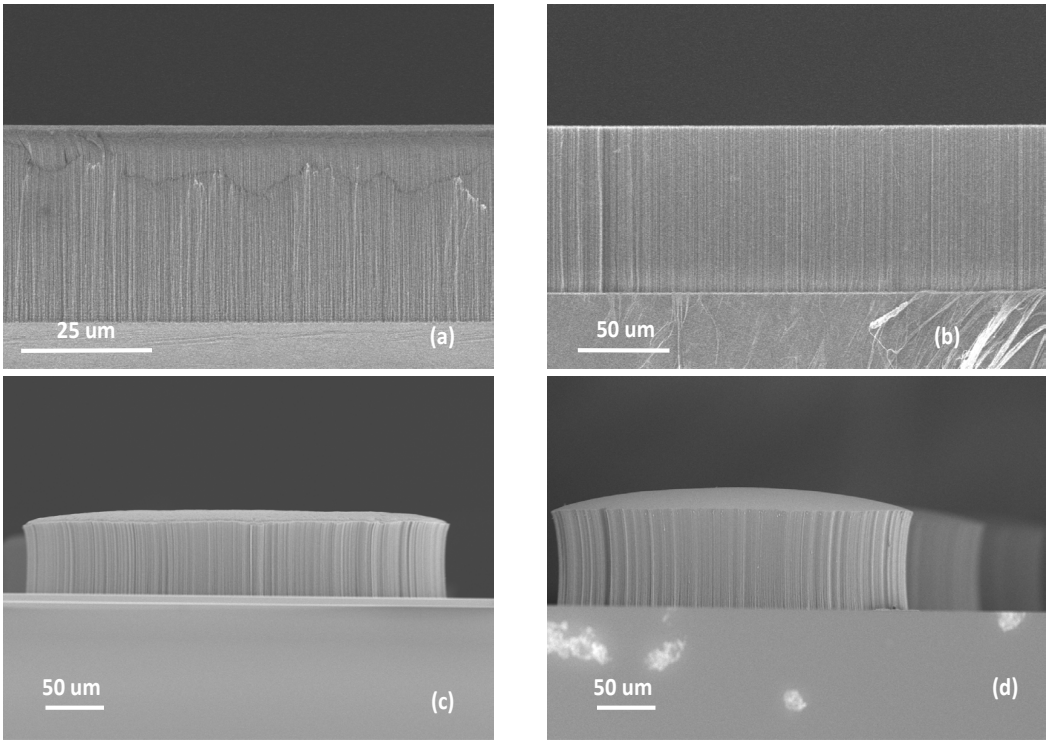

Figure 6.2: The figure shows SEM images of the vertically grown MWCNTs structures (forests) (a) Cross-sectional image of the grown MWCNTs with the Fe catalyst layer of $2nm$ and a growth time of 300 seconds having a measured height of $\sim 50\mu m$ (b) Cross-sectional image of the grown MWCNTs with the Fe catalyst layer of $3nm$ and growth time of 300 seconds having a measured height of $\sim 75\mu m$ (c) Vertically grown MWCNT micropillar with a height of $\sim 50\mu m$ and a radius of $125\mu m$ (Fe catalyst layer of $2nm$), and (d) Vertically grown MWCNT micropillar with a height of $\sim 75\mu m$ and a radius of $100\mu m$ (Fe catalyst layer of $3nm$). *Note: 3 minutes of oxygen plasma cleaning at 80W has been performed for each of the devices, followed by cleaving the sample, and nitrogen blowing to remove any dangling MWCNTs.

[147]. Acetylene (C_2H_2) gas has been used as a precursor, in the presence of nitrogen (N_2) and hydrogen (H_2) gas. The N_2 and H_2 gases are maintained in the chamber at a flow rate of $1000sccm$ and $100sccm$, respectively, while the temperature of the reactor has been gradually increased. The C_2H_2 gas is allowed to flow in the reactor, when the reactor temperature and pressure reaches $820°C$ and $720mbar$, respectively, having a flow rate of $160sccm$. This mixture of gases is then maintained for the MWCNT growth duration. Finally, the C_2H_2 and H_2 gases are discontinued, while the N_2 gas is flowed for further 5 to 10 minutes to gradually cool and displace the remaining gases in the reactor. The sample

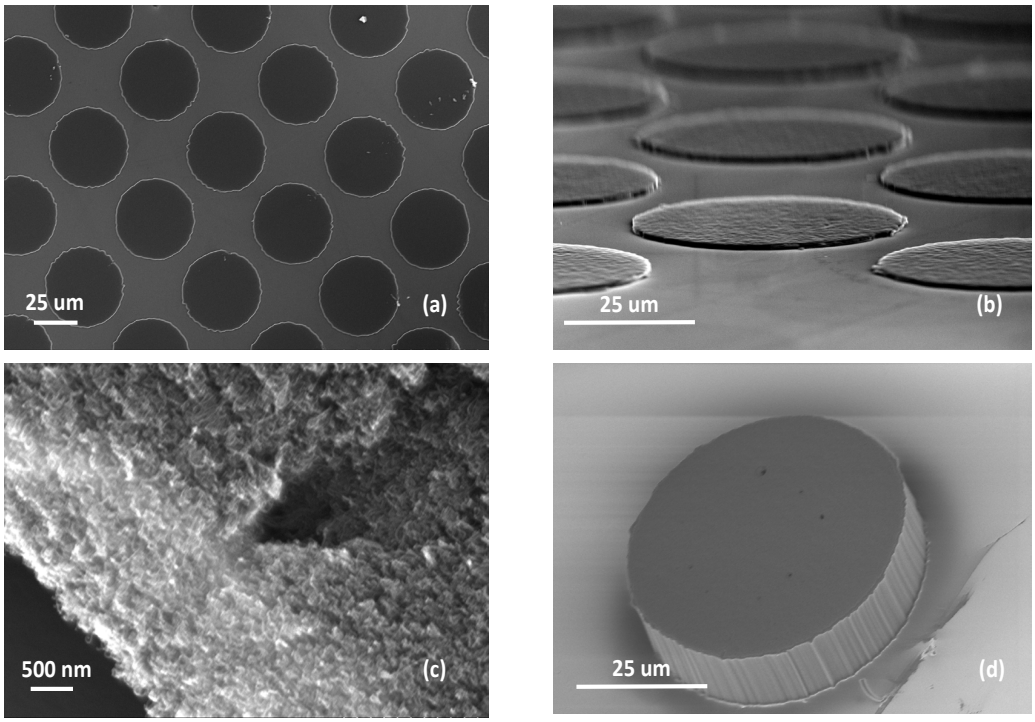

Figure 6.3: The figure shows SEM images of MWCNT grown micropillar shaped forests. (a) Top view of the grown MWCNT micropillar regions on a silicon substrate, (b) Pillar growth on a optical lithography defined region on a silicon substrate (growth time = 30 sec) (c) High magnification image of the porosity of the top surface of the MWCNTs, and (d) Vertically grown MWCNT micropillar with a height of $\sim 18\mu m$ and a radius of $25\mu m$. $1.1nm$ of Fe catalyst has been used for the growth of MWCNTs

is then removed from the chamber and inspected using the SEM for the MWCNT growth.

Vertically aligned MWCNT forests and micropillars have been fabricated using the optical lithography based lift-off process. A thin layer of photoresist (Shipley 1805) has been spin coated over the SiO_2 deposited ($200nm$ thick oxide) silicon sample. The spin coated sample is soft baked for 5 minutes at 115°C, and cooled down. The forest (or micropillar) pattern is defined by exposing the photoresist in the MA-6 mask aligner setup using the UV light (g-line, λ = 405nm), employing a transparency mask (or MLA 150 Maskless Aligner System). The exposed wafer is developed in the MF-319 photoresist developer for 4 minutes and inspected under the microscope for feature realization. The sample is then placed in the Denton e-beam evaporator tool and a $15nm$ thick layer of

Table 6.1: Variation of MWCNT growth with the amount of catalyst

Catalyst (Fe) Thickness (nm)	**Aluminum Oxide Thickness (nm)**	**Growth Time (seconds)**	**Growth Height (μm)**
1.1	10	180	18
1.1	10	300	30
2	20	300	50
3	30	300	75

Al_2O_3 has been evaporated, followed by $1.1nm$ thick layer of Fe. Followed by the e-beam deposition process, the sample is immersed in the Acetone solution for 5 minutes to remove the photoresist, leaving only the catalyst layer over the released features defined for the MWCNT forest (or micropillar) growth. The sample is dried using nitrogen gas, cleaned using oxygen plasma for 1 minute, and then placed in the Axitron Black Magic tool for the growth of MWCNT pillars. The MWCNT growth has been performed using the root growth mechanism, (as explained earlier), followed by inspection using optical microscope and SEM.

6.2.1 Tailoring the MWCNT forests and micropillar growth

Table 6.1 shows the variation of MWCNT growth with the amount of Fe catalyst used. Figure 6.1(a) and (b) shows the grown MWCNTs forests with $1.1nm$ of Fe catalyst and a growth time of 300 seconds and 180 seconds having a measured height of $\sim 30\mu m$ and $\sim 18\mu m$, respectively. Figure 6.2(a) shows the the grown MWCNTs forests with $2nm$ of Fe catalyst growth time of 300 seconds having a measured height of $\sim 50\mu m$, while figure 6.2(b) shows the grown MWCNTs forests with $3nm$ of Fe catalyst and 300 seconds of growth time, having a height of $\sim 75\mu m$. Similar results has been seen for the micropillar growth as shown in figures 6.2(c), 6.2(d), and 6.3(d).

It has been observed that for similar growth time and conditions, the increase in the deposited amount of Fe catalyst results in increased growth of the MWCNTs. It has also been observed that 300 seconds is the maximum time that allows growth of the MWCNTs, for these amounts of catalysts under these conditions. Increasing time more than 300 sec-

onds results in no further growth in the MWCNTs. I have used times upto 400 seconds for each of the Fe catalyst thickness mentioned in the table, with no further growth increase after 300 seconds has been observed. This allows control over the growth and height of the MWCNT forests and micropillars, which can be tailored according to the biomolecular pre-concentration device's requirements. Moreover, it can be observed from the SEM analysis that the CNTs grown are multi-walled (concentric walls) with an average height of $\sim 30\mu m$, average diameter of $\sim 8nm - 12nm$, and an average intra-CNT spacing of $\sim 80 - 100nm$, leading to a volume fraction of less than $1\% - 2\%$ CNTs. This resulted in an increased surface are for biomolecular capturing applications

6.3 Experimental Methods

6.3.1 Materials

The silane reagents (3-aminopropyl) triethoxysilane (APTES) and (3-Mercaptopropyl)-trimethoxysilane has been purchased from Sigma-Aldrich. Anhydrous 2-Propanol solution ($\geq$ 99% pure), Glutaraldehyde solution, Phosphate Buffer Saline (1X-PBS, pH 7.4), FITC-Avidin protein, N,N-Dimethylformamide (DMF), Ethanolamine, Sodium periodate, Sodium Acetate, Sodium Cyanoborohydride, and N,N-Dimethylformamide has been purchased from Sigma-Aldrich, US. Avidin from egg white has been purchased from Thermofisher scientific, US, while PC-biotin-PEG3-NHS-ester has been obtained from Click Chemistry Tools, US. Mouse monoclonal anti-PSA IgG antibody (10C-CR2051M5) and human lyophilized PSA (free-PSA (f-PSA) from human source) has been purchased from Fitzgerald Industries. Unconjugated Sambucus Nigra Lectin (SNA), Unconjugated Maackia Amurensis Lectin (MAA-MAL II) and Cy5-tagged SNA lectin has been purchased from Vector Labs, while unconjugated MAA-MAL II lectin has been purchased from BioWorld. ELISA Synblock blocking buffer has been purchased from BioRad. Silicon wafers has been procured from WaferPro, US, while the Glass wafers has been procured from University Wafers, US. SU-8 2035 and SU-8 developer has been purchased

from MicroChem, US. Sylgard 184 (PDMS by Dow Corning Corporation) and the curing agent has been purchased from Ellsworth Adhesives, US. The transparency masks has been developed and purchased from CAD/Art Services, US. All other equipment and cleaning solutions has been provided at the IEN cleanroom utility of the Georgia Institute of Technology, Atlanta, US.

6.3.2 MWCNT sample preparation

The 4 inch silicon and glass wafers have been diced into $7cm$ by $3cm$ sample using the ADT 7100 Dicing Saw. The diced silicon samples are copiously cleaned using acetone, methanol, and DI-water. The diced samples are then used for the growth of MWCNT forests and micropillars employing the optical lithography, e-beam deposition, and root growth fabrication mechanism as explained earlier.

6.3.3 MWCNT oxidation protocol

Protocol(1)

The plain silicon diced samples are dried using nitrogen gas, followed by Piranha (4:1 of H_2SO_4:H_2O_2) cleaning at 80°C for 30 minutes. The cleaned samples are again dried using the nitrogen gas and placed in the UV-Ozone Cleaning System (UVOCS) for 15 minutes. The UVOCS cleaning mechanism controls the hydrophilicity of the samples by generating the hydroxyl (-OH) bonds at the surface. The samples are then rinsed with DI-water, dried using nitrogen gas, and placed over the hotplate at 110°C for 5 minutes to completely remove any moisture content. The dehydrate baking step extremely important as the silane reagents reacts with the moisture (water) and hydrolyze over the sample resulting in loss of reactivity [145].

Protocol(2)

The MWCNTs grown samples are dried using nitrogen gas, followed by immersion in an oxidizing solution of 1:1:5 of $HCl : H_2O_2 : H_2O$ at room temperature for 60 minutes. The immersion in oxidizing solution results in generation of carboxylic (-COOH), carbonyl (-C=O), and hydroxyl (-OH) groups [194],[195]. Moreover, the presence of HCl results in removal of the remaining catalyst metal from the MWCNT surface [196]. It should be noted that the using of hydrogen peroxide (as a mild oxidizing reagent) results in minimal structural damage, no incorporation of foreign metals on the carbon surface, and can be used under neutral conditions, unlike the other CNT oxidizing techniques [196]. The cleaned samples are again dried using the nitrogen gas and placed in the UV-Ozone Cleaning System (UVOCS) for 15 minutes.

Protocol(3)

The MWCNTs grown samples are dried using nitrogen gas, followed by immersion in an oxidizing solution of 3:1 of $HNO_3 : H_2SO_4$ cleaning at room temperature for 30 minutes. The immersion in oxidizing solution results in generation of carboxylic (-COOH), carbonyl (-C=O), and hydroxyl (-OH) groups [194],[195]. It should be noted that extended treatment of MWCNTs using this protocol results in structural damage of the CNTs [195]. This protocol has been extensively utilized in the literature to oxidize the MWCNTs, especially for biomolecular attachments and sensing applications [55],[54],[197]. The oxidized samples are rinsed using DI-water, dried using the nitrogen gas and placed in the UV-Ozone Cleaning System (UVOCS) for 15 minutes before further utilization.

6.3.4 Microfluidic chip fabrication

The PDMS microchips are fabricated using the soft lithography technique as explained in the earlier chapters. The microchip design consists of a simple $50\mu m$ deep rectangular pre-concentration chamber with width and length of $500\mu m$ and $1cm$, respectively. The

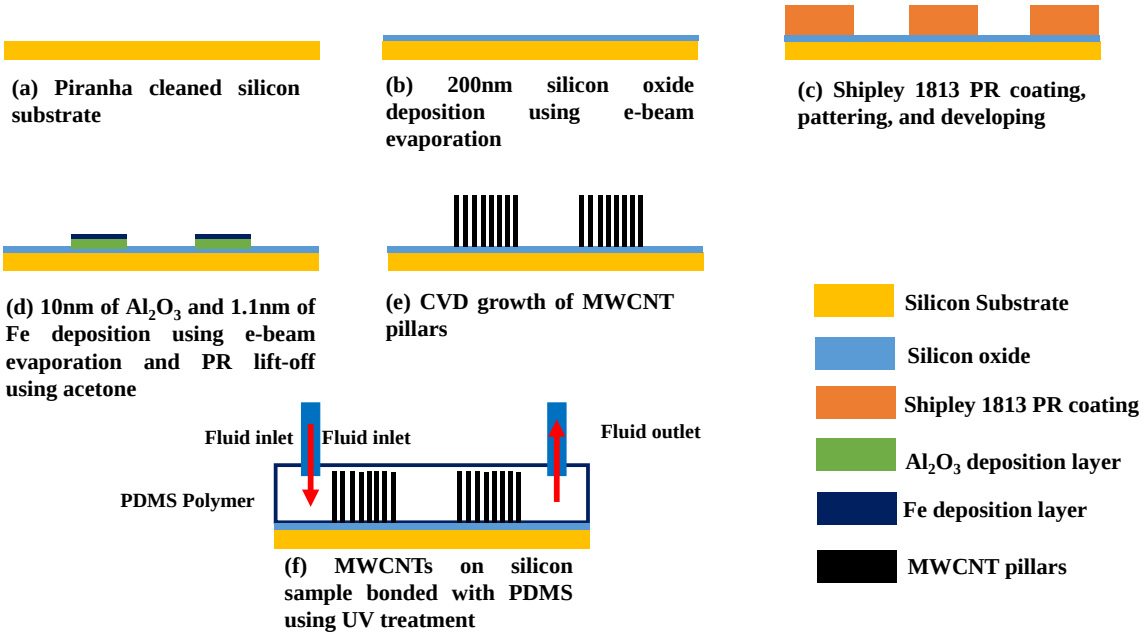

Figure 6.4: Schematic showing fabrication steps for the MWCNTs-based microfluidic pre-concentration device

microchip is aligned and bonded to the MWCNT forests ($30\mu m$ high, $500\mu m$ wide, and $1cm$ long) and micropillars ($20\mu m$ diameter, with $10\mu m$ spacing) fabricated on a silicon substrate.

6.3.5 Silanization protocol

The microfluidic chip is initially purged with the 1X-PBS solution (pH 7.4) to remove the trapped air bubbles. Once the air is removed, oxidizing solution containing hydrogen peroxide (H_2O_2), hydrochloric acid (HCl), and water (H_2O) (1:1:5) is flowed for 30 minutes at $10\mu l/min$ ($10\mu l/min$ flow is used throughout the experiments unless stated otherwise). The microfluidic chip is then rinsed with 1X-PBS solution, followed by the flow of silanization solution (5% APTES in 2-Propanol(v/v)) for 15 minutes, and a 2-Propanol rinse. The microfluidic chip is then baked at 80°C for 30 minutes in an oven and rinsed with 1X-PBS solution for 5 minutes.

6.3.6 Glutaraldehyde functionalization and Avidin immobilization

A 2.5% glutaraldehyde solution in 1X-PBS (v/v) is flowed through the APTES modified microfluidic chip for 15 minutes, followed by 30 minutes of incubation at room temperature. The microfluidic chip is then rinsed with 1X-PBS solution for 5 minutes.

6.3.7 Avidin protein immobilization

Protocol(1)

I used FITC-tagged Avidin to quantify the attachment of Avidin to the glutaraldehyde modified surface and estimate the biomolecular capture efficiency of the fabricated MWCNTs. A stock solution of $100\mu g/ml$ of FITC Avidin in 1X-PBS has been prepared along with ten different solutions of FITC Avidin (with 10 fold dilutions). Ten different MWCNT (silanized and GA treated) samples are immersed in these solutions for 30 minutes to have a uniform Avidin adsorption over the MWCNT surface. The MWCNT samples are then rinsed using 1X-PBS solution to removed the unreacted FITC-tagged Avidin. The fluorescence intensity of the sample is the measured to monitor the capture efficiency of the MWCNT samples.

Protocol(2)

Avidin solution is mixed with 0.04M N-Hydroxysuccinimide (NHS) and 0.06M N-(3-Dimethylaminopropyl)-N-ethylcarbodiimide hydrochloride (EDC) in 1X-PBS (or MES buffer (pH 5.3)). The APTES coated samples are then incubated in the solution having Avidin at room temperature for 1 hour to have a uniform Avidin adsorption over the surface. The samples are then rinsed using 1X-PBS solution to remove the unattached Avidin, dried using nitrogen gas, and taken for characterization.

It should be noted that the EDC (or EDC/NHS) conjugation protocol also allows conjugation of proteins by reacting with the carboxylic (-COOH) groups. The oxidized MWC-

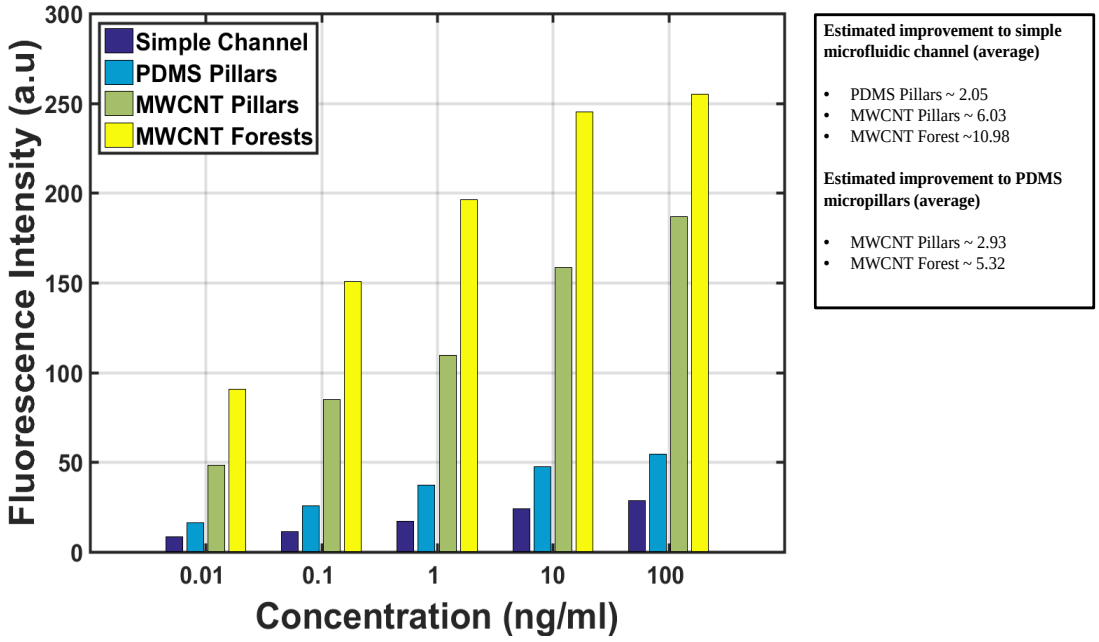

Figure 6.5: A comparative variation of measured fluorescence intensity against FITC-tagged Avidin concentration (ng/ml) in simple pre-concentration channel, PDMS micropillar-based pre-concentration chamber, MWCNT micropillar-based pre-concentration chamber, and MWCNT forests-based pre-concentration chamber. The average estimated enhancement in Avidin protein capturing compared to a simple microfluidic channel and PDMS micropillar-based preconcentration chamber has been shown.

NTs have presence of -COOH groups at their surface which can directly react with EDC (or EDC/NHS) to allow conjugation of Avidin protein. This mechanism has been extensively employed in the literature along with its associated challenges (as mentioned in Chapter 4) [198].

I have utilized the first protocol for the conjugation of Avidin protein for my work. Avidin solution is flowed through the microfluidic chip for 30 minutes, followed by incubation at room temperature for 30 minutes to have a uniform Avidin adsorption over the forests and micropillars in the pre-concentration chamber. The microfluidic chip is then rinsed using 1X-PBS solution to remove the unattached Avidin.

Figure 6.5 shows a comparative variation of measured fluorescence intensity against FITC-tagged Avidin concentration (ng/ml) in simple pre-concentration channel, PDMS

micropillar-based pre-concentration chamber, MWCNT micropillar-based pre-concentration chamber, and MWCNT forests-based pre-concentration chamber. The average estimated enhancement in Avidin protein capturing compared to a simple microfluidic channel and PDMS micropillar-based preconcentration chamber has been calculated. It has been observed that introduction of MWCNT micropillars in the pre-concentration chamber enhances the capturing efficiency by ~ 6 times, while the introduction of forests enhances the capturing efficiency by ~ 11 times, compared to simple microfluidic channel having a rectangular microfluidic channel of similar dimensions.

6.4 Affinity-based analyte pre-concentration, glycoprofiling, and release

The capturing and pre-concentration performance of the functionalized MWCNTs pre-concentration microfluidic chip has been evaluated using the human lyophilized PSA (from human source, fPSA), as mentioned earlier in Chapter 5. Briefly, five different concentrations of the PSA with 10-fold dilutions (i.e., 0.01, 0.1, 1, 10, and 100 ng/ml), in PBS buffer solution are flowed through the functionalized MWCNT microfluidic pre-concentration devices for 15 minutes, followed by 30 minutes of incubation. The functionalization of the devices has been performed in the similar manner as explained earlier in Chapter 5. The unattached PSA has been rinsed using 1X-PBS solution. A solution containing $100\mu g/ml$ of FITC-tagged MAA-II lectin and Cy5-tagged SNA lectin in 1X-PBS (pH 7.4) has been used to quantify the capturing and pre-concentration of PSA. The lectin solution is then flowed in the microfluidic capture chamber for 15 minutes. The chip is then incubated at room temperature for 30 minutes (in dark environment wrapped in aluminum foil). The chip is rinsed with 1X-PBS for 5 minutes and imaged for fluorescence measurements. Once fluorescence is observed, the chip is placed under a UV lamp (MJB4 Mask Aligner Lamp, $10mW/cm^2$ intensity, distance of 5cm) for 10 minutes. After the exposure, the chip is rinsed using 1X-PBS solution for 30 minutes (flow rate of $5\mu l/min$) and the fluorescence intensity is recorded.

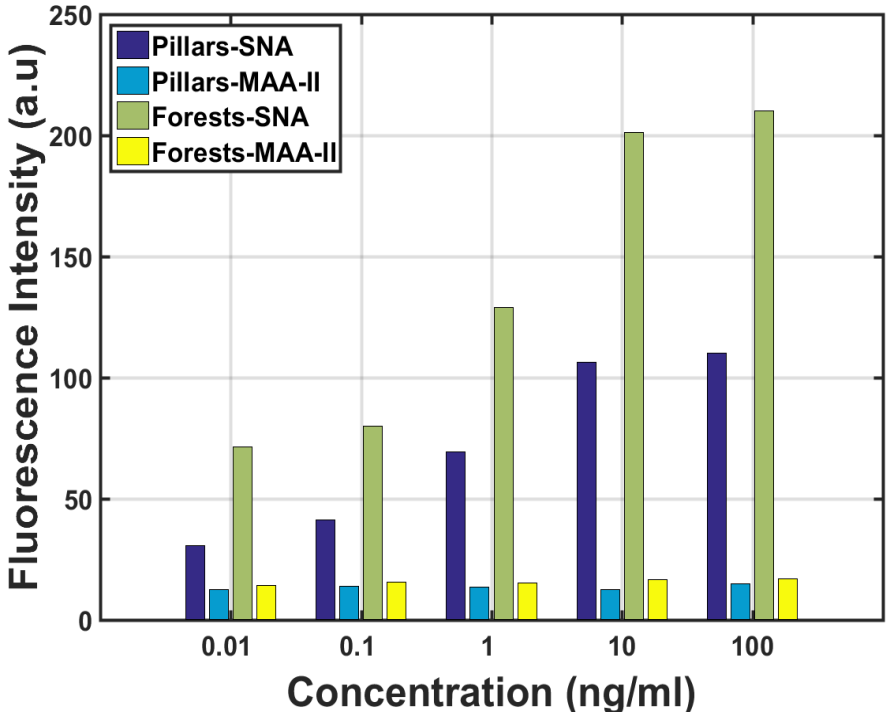

Figure 6.6: Actual results showing PSA capture with MWCNT micropillars and forests for a $500\mu m$ wide microfluidic channel. Fluorescence intensity variations for Cy5-tagged SNA lectin and FITC-tagged MAA-II lectin has been shown

6.4.1 Results and Discussions

As explained earlier in chapter 5, I have employed the SNA (Cy5-tagged) and MAA-II (FITC-tagged) lectins simultaneously, to demonstrate an on-chip multiplexed PSA glycoprofiling. Commercial fPSA (obtained from healthy subjects) has been used for the experiments. The fluorescence intensity has been measured to estimate the binding of the lectins to the PSA. The figure 6.6 shows the obtained fluorescence intensity results for the on-chip multiplexed PSA glycoprofiling in the MWCNT forests-based and MWCNT mircopillars-based affinity pre-concentrator devices. The fluorescence intensity measurements for the Cy5-tagged SNA lectin has shown considerable increase with the increase in PSA concentration, showing binding of the SNA lectin to the PSA. However, extremely weak fluorescence signals has been observed for the FITC-tagged MAA-II lectin showing negligible binding of the MAA-II lectin to the PSA. These results are in agreement with

the results obtained earlier for the PDMS micropillar-based microfluidic pre-concentration devices and ones reported in the literature [188],[191]. Moreover, the pre-concentrated sample has been released in ~ 30 minutes for both micropillars and forest based structures.

6.5 Conclusion

I demonstrated the use of carbon nanotubes (CNTs) as high porosity material for enhanced on-chip biomolecular pre-concentration applications. I fabricated and utilized CNTs forests and micropillar structures over a silicon substrate to increase the effective surface area of a microfluidic pre-concentrator device. These CNTs grown are multi-walled (concentric walls) with an average height of $\sim 30\mu m$, average diameter of $\sim 8nm - 12nm$, and an average intra-CNT spacing of $\sim 80 - 100nm$, leading to a volume fraction of less than $1\% - 2\%$ CNTs. This resulted in an increased surface are for biomolecular capturing applications.

The MWCNT forests and micropillars has been grown over a silicon substrate, aligned, and bonded with the PDMS based microfluidic channels to develop the biomolecular pre-concentrator and filtering devices. The capturing efficiency and performance of these designed MWCNT forests and micropillar-based pre-concentration platforms have been assessed by employing the PC-biotin linker-based modified lectin immunoassay for the PSA biomarker capturing, pre-concentration, glycoprofiling, and release. The capability of multiplexed glycoprofiling for elucidating the PTMs of the PSA cancer biomarker has been demonstrated by using the SNA and MAA-II lectins. An estimated (interpolating the measured fluorescence results) minimum LOD of $\sim 0.5pg/ml$ and a LOQ of $\sim 1pg/ml$ can be achieved for on-chip multiplexed PSA pre-concentration, detection, and glycoprofiling using the MWCNT forest based platform.

CHAPTER 7
INTEGRATED OPTICAL MICRORESONATORS FOR MULTIPLEXED SENSING APPLICATIONS

7.1 Introduction

In this chapter, a design approach for high-Q optical microresonators in silicon has been presented. The high-Q optical microresonators provide highly sensitive, compact, and scalable transducers that enables versatile realization of highly multiplexed and array based chemical and biological sensing platforms. The immobilization of different biological reagents such as silanes, antibodies, biomarkers, DNA, viruses, and lectins, makes the sensor highly sensitive and selective to different target antigens of interest. Moreover, the integration of microfluidics with the sensing transducers allows on demand delievery of extremely small volumes of chemical and biological analytes, resulting in realization of advanced LOC solutions for various chemical and biological sensing applications.

7.2 Optical Microresonators

The resonance wavelength of the optical microresonators is dependent on the refractive index of the material surrounding the resonator. The refractive index variation in the evanescent tail of the resonator mode such as TE or TM, results in a resonance shift. Chemicals and biomolecules having different refractive indices can be detected by monitoring the shift in resonance for any resonator device. The planar cavity based resonators such as microrings, microdisks, racetracks, or spirals, are ”resonating” (on the resonance) when the ”phase” ϕ is an integer multiple of 2π, or when the wavelength of the light fits a whole number of times inside the optical length of the resonator [109], as expressed in Equation 7.1.

$$\lambda_{res} = \frac{n_{eff} L}{m} \tag{7.1}$$

where n_{eff} = effective refractive index of the guided mode, L = length of the cavity (microring resonator), m = azimuthal mode integer = 1,2,3,... .

Exploiting the highly sensitive refractive index based sensing capability, I have designed ultra-compact, high-Q, single-mode, and TM polarized optical microresonators for operation at $1550nm$ wavelength. Silicon-on-insulator (SOI) sample has been considered as the substrate owing to its CMOS process compatibility. Silicon ($n = 3.480$ @ $\lambda = 1550nm$) as device layer, silicon oxide ($n = 1.444$ @ $\lambda = 1550nm$) as bottom cladding, and air ($n = 1.000$ @ $\lambda = 1550nm$) and water ($n = 1.318$ @ $\lambda = 1550nm$) as top cladding, has been used for the design. COMSOL finite element method (FEM) software has been employed for the design and simulations of these optical microresonators. Figure 7.1 illustrates the planar on-chip architecture of the waveguide coupled microresonators.

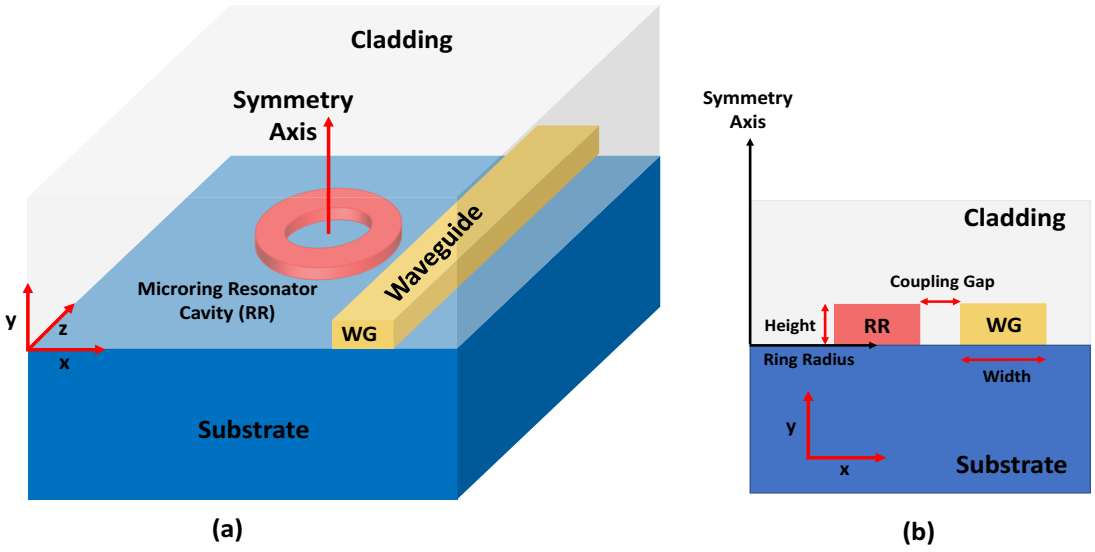

Figure 7.1: A pictorial illustration of (a) an optical microresonator (microring) coupled to an input waveguide (b) 2D cross sectional view of the illustrated 3D architecture in (a).

7.2.1 Microresonator Optimization and Design Simulations

The TE and TM polarized optical mode profiles for the silicon microresonator devices on a silicon-on-insulator (SOI) substrate ($250nm$ of silicon device layer and $3\mu m$ of buried oxide layer), with air and water as cladding for different values of device widths, operating at $\lambda = 1550nm$, has been simulated using COMSOL numerical software. The width (w_r) of the resonators and the input waveguide has been selected to be $500nm$ to ensure single-mode TE or TM polarized operation [199].

The mode profile simulations for a $4\mu m$ microring resonator (with air cladding) revealed bulk sensitivities of $44.684nm/RIU$ and $124.671nm/RIU$ for TE and TM polarized light, respectively. Similarly, bulk sensitivities of $50.157nm/RIU$ and $160.205nm/RIU$ for TE and TM polarized light with water as cladding has been observed, respectively. Figure 7.2 shows the COMSOL simulation for the TE mode and TM optical modes propagating in a $500nm$ wide and $250nm$ thick silicon device, with air and water as top claddings. Table 7.1 shows the COMSOL simulation results for the designed $4\mu m$ microring resonator in air and water cladding.

It has been observed that the TM mode profile extends much further into the cladding compared to the TE mode profile. This results in higher sensitivities of the TM mode (upto 3 times greater than TE mode) for bulk refractive index variations. Moreover, when compared to the TE mode, the TM mode have much less interaction with the sidewalls of the resonators as most of the mode energy is guided above the waveguide into the cladding. This allows lesser scattering loss as the fabricated devices are prone to sidewall imperfections owing to the fabrication limitations [199]. These advantages of the TM polarized mode allowed its selection for chemical and biological sensing applications. Figure 7.3 shows the COMSOL simulation results for a TM polarized mode propagation in a silicon device (height = 250 nm, width = 500 nm) on a SOI sample ($3\mu m$ of buried oxide), operating at $\lambda = 1550nm$ with (a) air cladding (n = 1.0), (b) water cladding (n = 1.318), (c) oxide cladding (n = 1.44), and (d) SU-8 (n = 1.57) cladding.

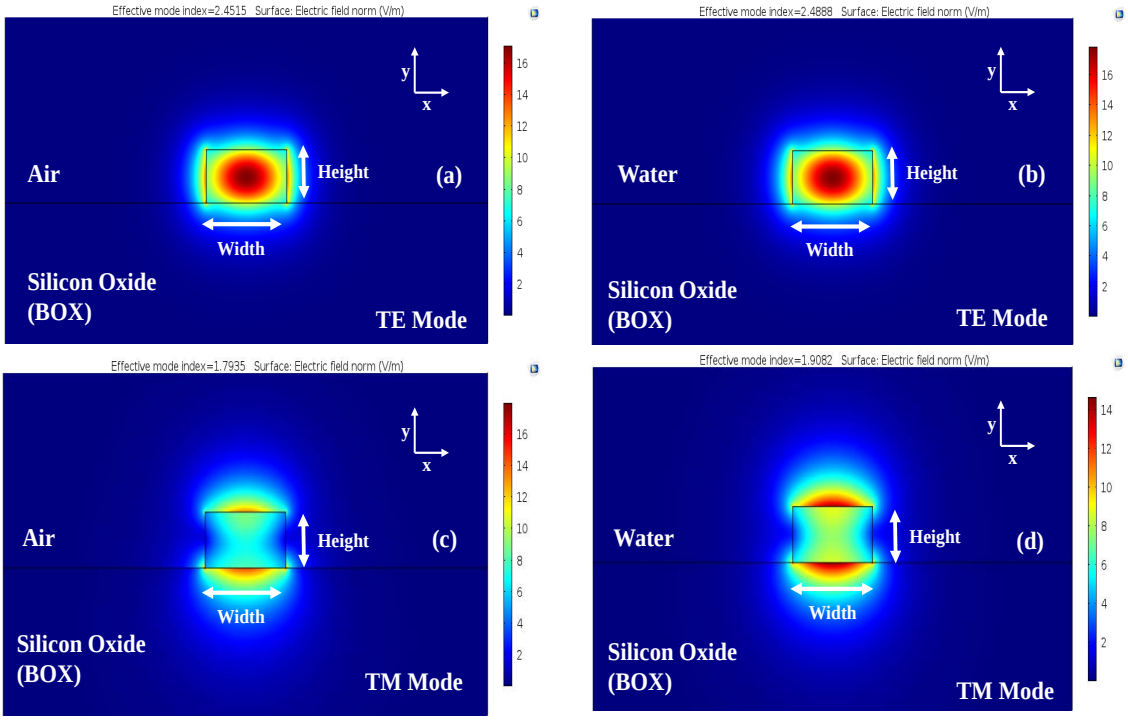

Figure 7.2: COMSOL effective mode simulations for a $500nm$ wide, $250nm$ thick silicon microresonator on a SOI substrate ($3\mu m$ buried oxide) operating at $\lambda = 1550nm$ (a) TE polarized optical mode profile (air cladding), (b) TE polarized optical mode profile (water cladding), (c) TM polarized optical mode profile (air cladding), (d) TM polarized optical mode profile (water cladding)

The FSR simulations of the $4\mu m$ microring resonator operating at $\lambda = 1550nm$, with air cladding has resulted in $23.62nm$ and $21.62nm$ of spectral shift between the alternating azimuthal mode orders for the TE and TM polarized optical mode excitations,respectively. Similarly, FSR values of $23.83nm$ and $24.61nm$ has been observed for water clad TE and TM polarized microring resonators, respectively, as shown in figure 7.4. Similar FSR simulations for a $100\mu m$ microring resonator (having a total cavity length of $\sim 630\mu m$, resembling a spiral resonator), operating at $\lambda = 1550nm$ has been performed. FSR values of $0.908nm$ and $0.854nm$ has been observed for air clad TE and TM polarized optical mode operation, respectively. Similarly, FSR values of $0.962nm$ and $0.881nm$ has been observed for water clad TE and TM polarized mode operation, respectively. Figure 7.4 shows the FSR simulations for a $4\mu m$ microring resonator device with air and water as top

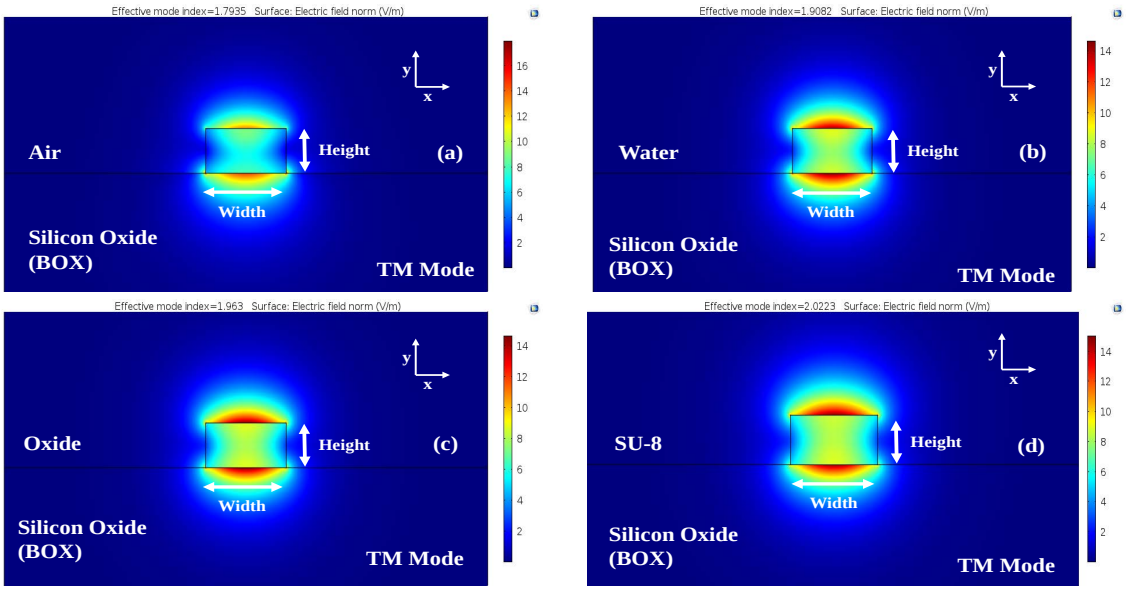

Figure 7.3: COMSOL simulation results for a TM polarized optical mode propagation at $\lambda = 1550nm$ in a SOI sample ($height = 250nm, width = 500nm$) with (a) air cladding (n = 1.0) , (b) water cladding (n = 1.318), (c) oxide cladding (n = 1.44), and (d) SU-8 cladding (n = 1.57)

claddings. Both TE and TM mode profiles of the $4\mu m$ microring resonator device has been shown. Table 7.2 shows the COMSOL simulation results for the designed spiral resonator in air and water cladding.

It has been observed that the FSR bandwidth decreases with the increase in radius of the microresonators. The smaller resonator radius (i.e., smaller cavity lengths) is preferred as it allows multiple similar resonators (with small modifications in the dimensions) to be incorporated in the FSR bandwidth without having any spectral overlap, thus allowing highly multiplexed operation capability. The challenge with smaller radius lies in the coupling gap adjustment between the single mode optical waveguide and the resonator [199]. Smaller resonator dimensions result in considerably smaller coupling gap requirements for efficient coupling i.e., the critical coupling [199]. Therefore, considering the fabrication limitations, a microring radius of $4\mu m$ has been selected for the multiplexed array design, with coupling gap of $100nm$ and $120nm$ for air and water cladding, respectively.

Although, multiplexed sensing platforms can be achieved using smaller resonator di-

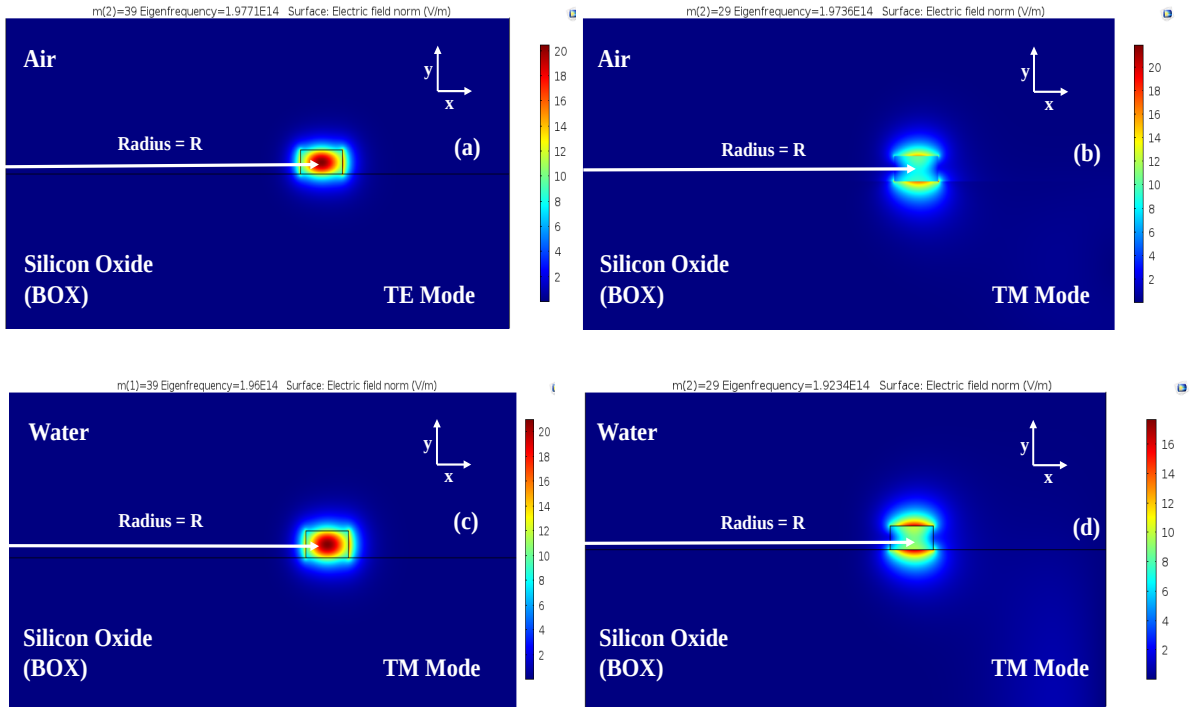

Figure 7.4: COMSOL free spectral range (FSR) simulations for a $500nm$ wide, $250nm$ thick silicon microresonator on a SOI substrate ($3\mu m$ buried oxide) operating at $\lambda = 1550nm$ (a) TE polarized optical mode profile (m = 39, air cladding), (b) TM polarized optical mode profile (m = 29, air cladding), (c) TE polarized optical mode profile (m = 39, water cladding), (d) TM polarized optical mode profile (m = 29, water cladding)

mensions and tailoring the coupling gap, the surface for the analyte interaction also decreases with the decrease in the sensor dimensions. Conversely, increasing the resonator dimensions increases the overall footprint of the device, decreases the available FSR bandwidth for multiplexing, and consumes the precious silicon real estate. To address these challenges, I came up with a spiral shaped resonator design, having a cavity length equivalent to a $100\mu m$ ring resonator, packed within a $50\mu m$ by $50\mu m$ of silicon footprint, and with a coupling gap of $\sim 250nm$. This allows larger capture area per unit of available silicon real estate and also relaxes the phase matching conditions (coupling gap adjustment) for operation in critical coupling regime [121],[200]. The FSR bandwidth can also be tailored accordingly for highly multiplexed sensing applications by changing the overall cavity length of the spiral resonators according to the requirement.

The silicon microresonator's thermal drift issue has been addressed by selectively coating ring resonators as on-chip reference resonators. SU-8 polymer ($n = 1.57$ @ $\lambda = 1550nm$) has been employed for the coating purpose. Both of the designs i.e., the multiplexed microring resonator design and the spiral array design, are equipped with a SU-8 coated $4\mu m$ microring reference resonators. The SU-8 protective layer isolates the microring resonators from the biological and chemical solutions during the sensing experiments, thereby allowing a differential resonance shift measurement which is not affected by the temperature, or a homogeneous wavelength drift in the laser.

Table 7.1: COMSOL simulation results for microring resonator in air and water cladding

Material	**Refractive Index (n @ 1.55 μ m)**	**Effective Refractive Index (n_{eff})**		**Free Spectral Range - FSR (nm)**		**Bulk Sensitivity (nm/RIU)**	
		TE	**TM**	**TE**	**TM**	**TE**	**TM**
Air	1.000	2.452	1.794	23.600	21.623	44.685	124.672
Water	1.318	2.489	1.908	23.890	24.612	50.157	160.205

Table 7.2: COMSOL simulation results for spiral resonator in air and water cladding

Material	**Refractive Index (n @ 1.55 μ m)**	**Effective Refractive Index (n_{eff})**		**Free Spectral Range - FSR (nm)**		**Bulk Sensitivity (nm/RIU)**	
		TE	**TM**	**TE**	**TM**	**TE**	**TM**
Air	1.000	2.452	1.794	0.908	0.854	35.237	100.313
Water	1.318	2.489	1.908	0.962	0.881	53.368	160.677

7.2.2 Grating Design

Coupling light is a major aspect in the design of any optical sensing platform. In the proposed microresonator based design, TM polarized optical mode has been preferred for enhanced sensing applications. To excite this desired TM polarized optical mode into the sensor platform, a periodic, fully etched, TM polarized, optical grating couplers has been designed, simulated, optimized, fabricated, and characterized for the realization of a disposable, POC, densely integrated, and compact on-chip optical sensing platform. 2D-Finite-difference Time-domain (FDTD) simulations and particle swarm optimization algorithm available with the Lumerical software platform has been employed for the designing and

optimization of the TM polarized optical grating coupler to achieve high I/O light coupling efficiency for the integrated photonic sensor chip.

The traditional methods of designing optical grating couplers involve exhaustive simulations for optimizing the design parameters, such as grating period (pitch), grating duty cycle (or fill factor), effective refractive index, transmission efficiency, fiber position, back reflections [201],[202]. These simulations are time consuming and computationally intensive. In this design approach, I used the available mathematical models (i.e, Bragg's condition and effective refractive index estimation) for the initial calculations employing the process and design limited parameters such as cladding, core, silicon thickness, etch depth, operating wavelength, effective refractive index, fiber input, output angles as initial values [201],[202]. Once these initial results are calculated, I employed the "Lumerical software" program to estimate and optimize the I/O fiber position over the grating, followed by optimization of the pitch and duty cycle of gratings employing the particle swarm optimization algorithm (available with Lumerical Software). Transmission efficiency (T_{avg}) has been selected as the figure of merit (FOM) and is maximized during these optimizations. Figure 7.5 shows a work flow chart of the approach followed for the design.

Silicon-on-insulator (SOI) sample has been considered as the substrate for the design of TM polarized gratings. Silicon as device layer with a thickness of $250nm$, silicon oxide as bottom cladding with a thickness of $3\mu m$, and air as top cladding has been considered as the starting point for the design. The design has been proposed to have a single lithography step and etching step for the realization of overall sensing architecture, resulting in a fast and economical fabrication solution for the device manufacturing and packaging. Therefore, a grating etch depth value of $250nm$ has been used through-out the design analysis and optimization. Figure 7.6 shows a 2D illustration of a fully etched and TM polarized grating coupler on a SOI substrate.

For initial analytical calculations, a grating duty cycle (D) value of 0.5 has been assumed. Effective refractive index of TM polarized mode (n_{eff1}) propagating in silicon has

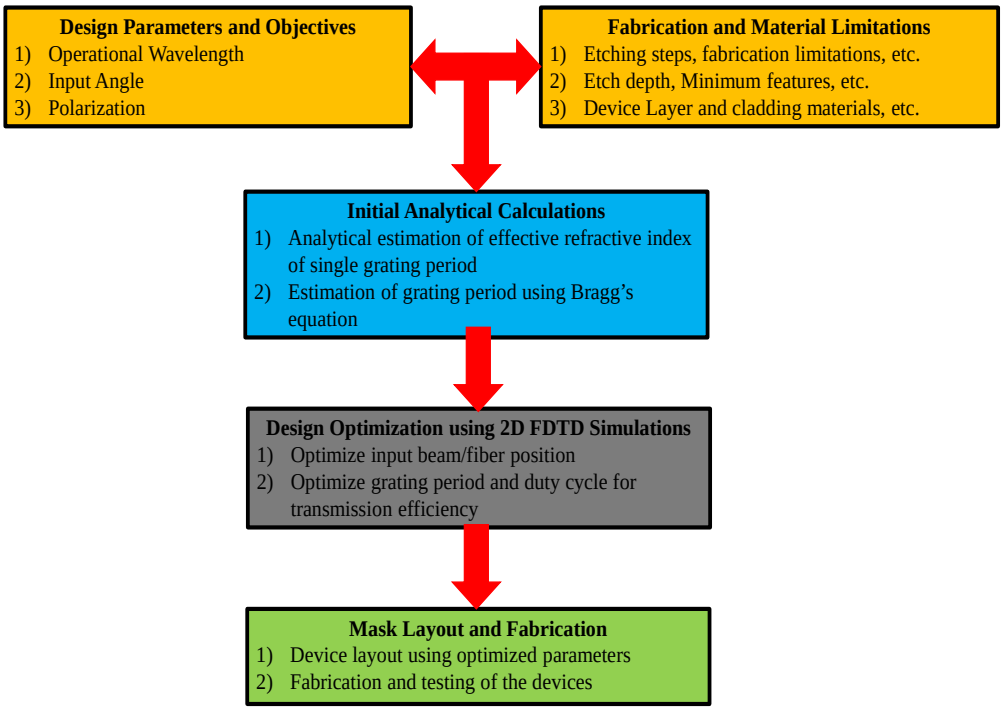

Figure 7.5: A schematic work flow for 2D-FDTD based design of grating couplers

been simulated using COMSOL i.e., $n_{eff1} = 1.7935$, and an effective refractive index of air i.e., etched section, n_{eff2}) = 1.0, has been used for the effective refractive index estimation (for TM polarized mode) for a periodic unit cell of the grating, using the formula given in equation 3.2.

$$n_{eff_{TM}} = n_{eff1} + (1 - D)n_{eff2} \tag{7.2}$$

where

n_{eff1} = effective refractive index for TM mode propagation in silicon (non-etch section), n_{eff2} = effective refractive index for TM mode propagation in air (etched section), and D = Duty Cycle (fill factor) of the grating

The Bragg's condition, as given in equation 3.3, is then utilized for the initial calculations of the grating period (Λ). The 1st order grating mode ($m = 1$), operating laser wavelength of $\lambda = 1550nm$, and an I/O fiber angle (θ) of 10° has been assumed for the

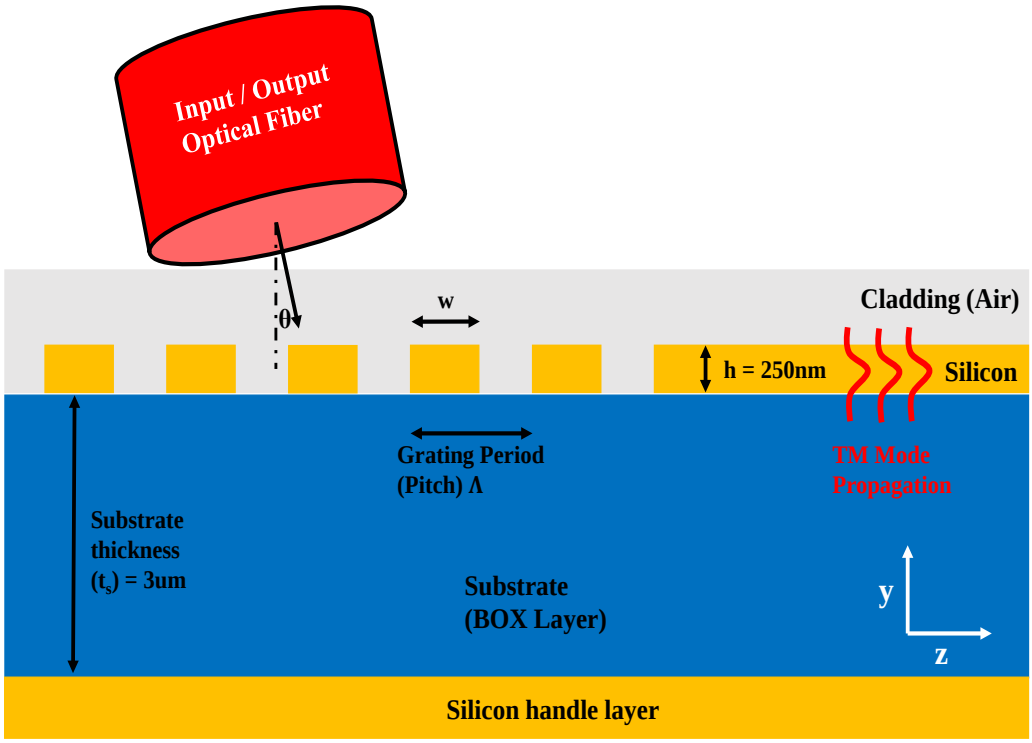

Figure 7.6: A 2D illustration of a fully etched and TM polarized grating coupler on a SOI substrate

initial calculations.

$$m\frac{\lambda}{\Lambda} = n_{eff_{TM}} - n_c sin(\theta) \tag{7.3}$$

where

m = grating mode order, λ = laser wavelength, Λ = grating pitch, $n_{eff_{TM}}$ = effective refractive index for the propagating TM mode in one unit cell of the grating, n_c = cladding refractive index, θ = I/O fiber angle.

The analytically calculated values are then used as the initial conditions for the optimization of the grating's period (Λ) and the duty cycle (D). The average transmission efficiency (T_{avg}) between $1500nm$ and $1600nm$ has been selected as the FOM for the optimization of the gratings, as shown in equation 3.3. Particle swarm optimization setup is then employed to optimize the FOM for both input and output grating couplers.

$$FOM = T_{avg} = \frac{\int_{1.6\mu m}^{1.5\mu m} T(\lambda) d\lambda}{\int_{1.6\mu m}^{1.5\mu m} d\lambda} \tag{7.4}$$

Figure 7.7 shows the results for the optimization. An efficiency of 49.25% has been achieved for the grating couplers using a duty cycle (D) of 0.555 with a grating pitch of $0.996\mu m$. Actual TM polarized grating couplers are then fabricated using the obtained values to demonstrate the CMOS compatible fabrication of densely integrated, grating based optical sensing platforms.

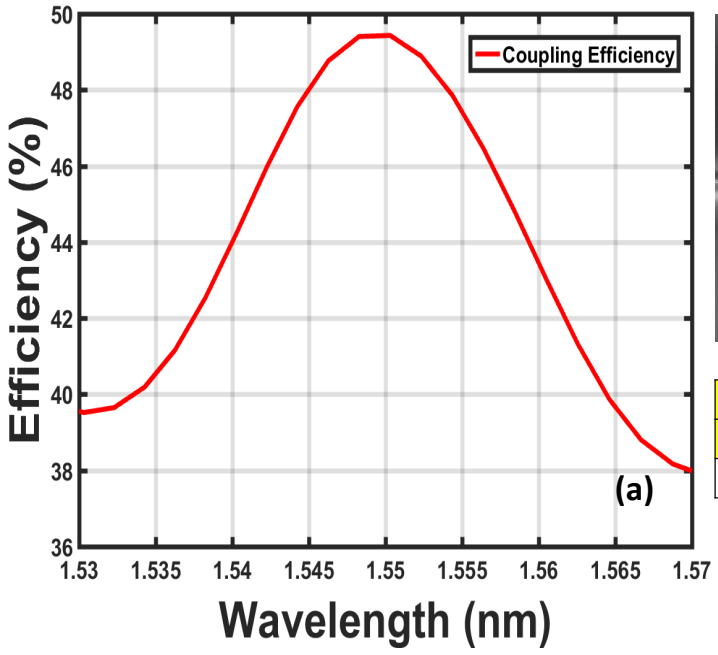

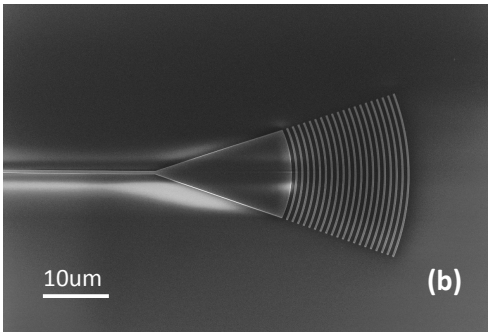

Pitch	Duty Cycle	Efficiency
Λ (μm)	D	η
0.996	0.555	49.2

Figure 7.7: The figure shows (a) optimized coupling efficiency result for a TM polarized grating using the Lumerical FDTD software, (b) SEMs images for the fabricated TM polarized grating, and (c) a table showing optimized results for pitch (Λ), duty cycle (D), and efficiency (η) using the Lumerical FDTD software.

7.2.3 Multiplexed Sensing using Optical Microring Resonators

Multiple sets of five high-Q microring resonators coupled to a common input waveguide have been designed and fabricated. The width of the microring resonators is selected to be $500nm$ and their radii are adjusted (radii variations of $\pm 10nm$ across a radius of $4\mu m$), to

achieve equally spaced (within one free spectral range (FSR)) and unique resonance wavelengths for each of the microrings. This allows independent and individual monitoring of each microring sensing element at its corresponding wavelength, such that when simultaneously excited, the corresponding resonance frequencies are evenly spaced in the desired FSR range without any spectral overlap. This allows realization of highly multiplexed refractive index based sensing capability.

7.2.4 Array based Sensing using Optical Spiral Microresonators

High-Q spiral resonators, which provide a higher sensing area in a small footprint, as an alternative to the multiplexed microring resonator array has been proposed. Single-mode TM polarized spiral resonators with a length of $630\mu m$, (enabling higher light-matter interaction with the analyte over the resonator surface) has been designed and fabricated. The designed spiral resonators provide a small footprint of $50\mu m$ by $50\mu m$, and a sensing area more than 6 times of a microring in a similar footprint.

7.3 Fabrication

The TM mode I/O grating devices, along with the waveguides and the micro resonators (microrings and spirals) are patterned on a SOI substrate with a $250nm$ thick silicon device layer on a $3\mu m$ thick buried oxide, using electron beam lithography. 6% HSQ (negative electron beam resist) is spin coated on the sample, followed by ESPACER which prevents the charge build up effect on the sample. The device pattern is written over the sample using the JEOL JBX-9300FS EBL system. Immediately after pattering, the sample is rinsed with running DI-water for 2 minutes, dried using nitrogen gas and developed in a solution of tetramethylammonium hydroxide (TMAH, 25% w/w) at 40°C for 30 seconds. The developed sample is rinsed using DI-water for 5 minutes, dried using nitrogen gas, and etched using a chlorine-based recipe in an Inductively Coupled Plasma (ICP) system. Figure 7.8 (a) and (b) shows the flow diagram for the major fabrication processes involved in the real-

ization of the on-chip sensing devices. Figure 7.9 (a) and (c) shows the optical microscope images for the fabricated TM optical mode grating and microring resonator, while figure 7.9 (b) and (d) shows the SEM images of fabricated TM optical mode grating and microring resonator. Similarly, figure 7.10 (a) and (b) shows the optical microscope and SEM images of the fabricated spiral resonator.

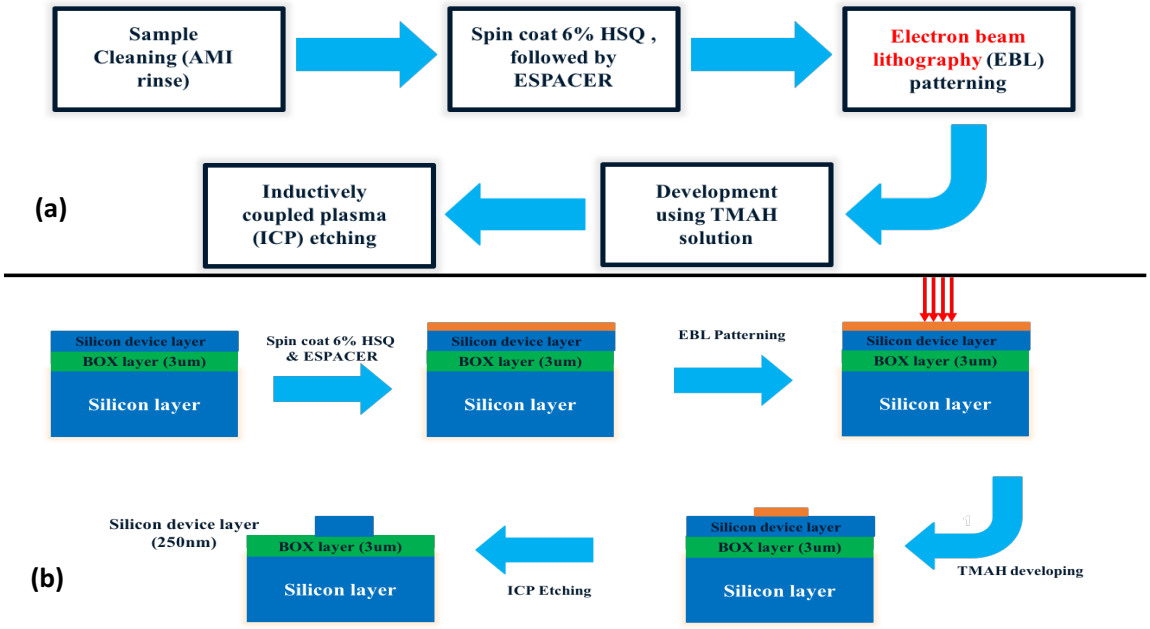

Figure 7.8: (a) A fabrication process flow diagram showing major steps involved in device fabrication (b) A schematic illustration of major device fabrication steps (side view cross-section)

7.4 Characterization

The fabricated devices are characterized using an Infra Red (IR) tunable laser (Agilent 81682A) setup. The laser is launched into a lensed single mode fiber using an in-line polarization controller. The fiber is mounted on a 3D rotating stage equiped with XYZ axis controllers, along with the rotation and tilt compensation mechanism. The fiber is then aligned such that the outcoming light is focused on the input facet of the input TM mode grating coupler. The output light from the chip is collected at the output facet of the output TM mode grating coupler using a similar lensed fiber and fed directly to an InGaAs

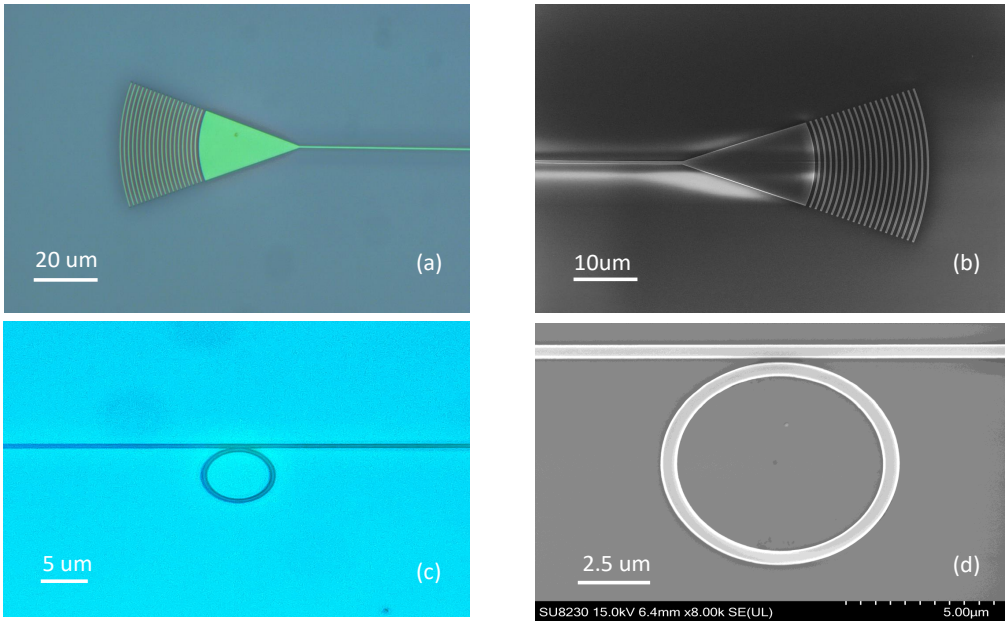

Figure 7.9: SEMs and microscope images of fabricated devices

photodetector (Thorlabs PDB 150C, 800 nm to 1700 nm).

The transmission spectrum of all the devices is then obtained by sweeping the laser wavelength from 1460 nm to 1600 nm. The state of polarization of the incoming laser light is adjusted by aligning the single mode optical fibers with the TM grating, and the in-line polarization controller is adjusted such that the TM resonance modes of the microring resonator are only obtained at the output (i.e., TE modes are not excited through the waveguide). Once the TM polarization is adjusted, the transmission spectrum of the desired devices on the chip are characterized by measuring the optical power in the output fiber for each device. To minimize the effect of fiber to waveguide coupling variation (caused by possible misalignment), we repeat the alignment several times to make sure maximum coupling is achieved at a fixed wavelength (i.e., 1550 nm). Moreover, the experiments has been performed for a constant input laser power i.e., $800\mu W$, with the sample placed over a temperature stabilization stage at $25°C$ to have uniform readings across all the experiments. Figure 7.11 shows an illustration of optical fiber-based characterization setup for silicon microresonator sensing platforms [203].

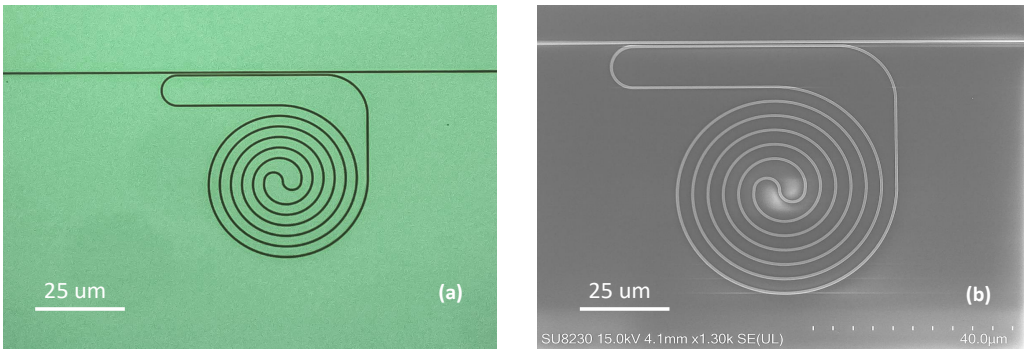

Figure 7.10: SEMs and microscope images of fabricated devices

Figure 7.12 shows the post-processed experimental transmission spectrum of a multiplexed ring resonator platform with air cladding. The resonance corresponding to each of the fabricated minoring resonator are visible. Marked FSR of $\sim 23nm$ for the azimuthal mode orders (m) of 28 and 27 respectively, is also shown for the fabricated device. The inset shows a single resonance peak of a ring resonator R_4 for azimuthal order of 29, having a measured loaded Q-factor of $\sim 50K$. Figure 7.13 shows the post-processed experimental transmission spectrum of a multiplexed ring resonator platform with and without SU-8 coated reference resonator in air cladding. The reference resonator peaks are marked on the spectrum.

Figure 7.14 (a) shows the post-processed experimental transmission spectrum of a spiral ring resonator platform in air cladding. Figure 7.14 (b) shows a zoom-in version of the transmission spectrum with marked FSR of $0.88nm$ between azimuthal mode orders of 727 and 726, respectively, and figure 7.14 (c) shows a single resonance peak of a spiral resonator for azimuthal mode order of 727. Loaded Q-factor of $\sim 50K$ has been observed for the fabricated device. Figure 7.15 shows a post-processed experimental transmission

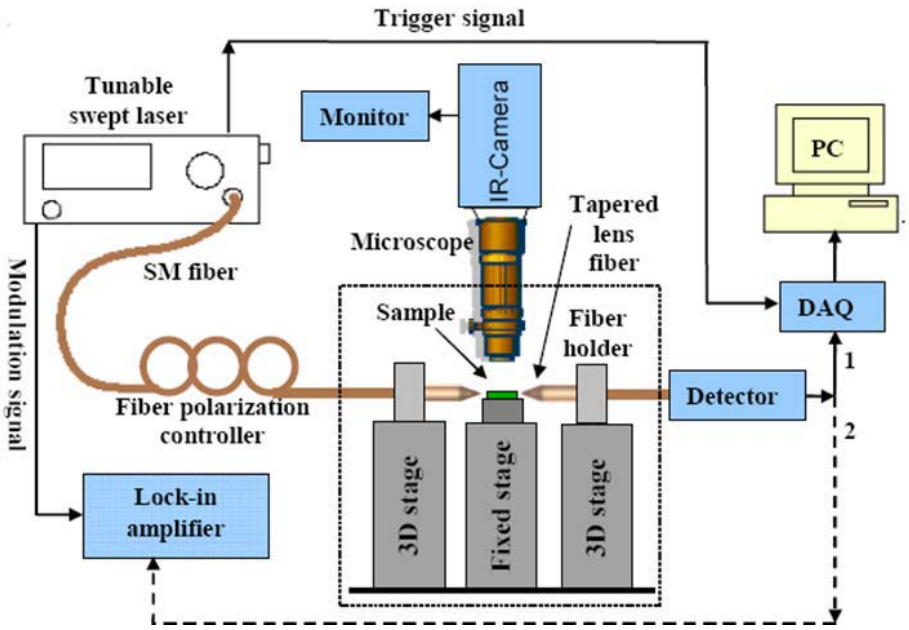

Figure 7.11: An illustration of optical fiber-based characterization setup for silicon microresonator sensing platforms [203]

spectrum of a spiral resonator platform with and without SU-8 coated reference resonator in air cladding. The reference resonator peaks are marked on the spectrum.

7.5 Sensor Performance Metrics

7.5.1 Sensitivity (S)

Sensitivity (S) of a microring resonator is defined as the shift in resonance wavelength per unit change in the refractive index of the cladding (nm/RIU) [204]. The normalized sensitivity can be obtained as

$$S' = \frac{S}{\lambda}$$

where S is given as

$$S = \frac{\Delta\lambda}{\Delta n_{clad}}$$

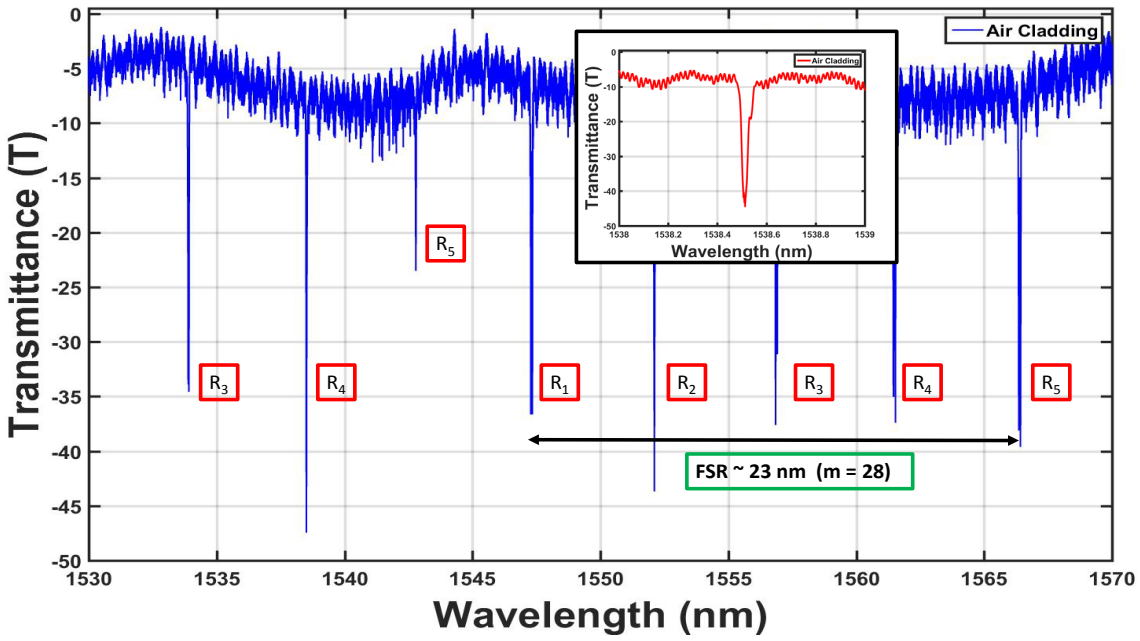

Figure 7.12: The figure shows a post-processed experimental transmission spectrum of a multiplexed ring resonator platform with air cladding. The resonance corresponding to each of the fabricated minoring resonator are visible. Marked FSR of $\sim 23nm$ for the azimuthal mode orders (m) of 28 and 27 respectively, is also shown for the fabricated device. The inset shows a single resonance peak of a ring resonator R_4 for azimuthal order of 29, having a measured loaded Q-factor of $\sim 50K$.

such that λ = input wavelength, $\Delta\lambda$ = change in resonance wavelength, and Δn_{clad} = change in the refractive index of the cladding.

In the realm of sensing applications, the change in refractive index can result from a change in the bulk refractive index, biomolecular layer attachment over the surface, surface density of attached biomolecules, or analyte concentration [114],[115].

7.5.2 Q-Factor

The Q-factor of a microring resonator has been defined as the number of oscillations before the energy in the resonators decays to 1/e of its actual value [204]. Higher Q-factor means in more light time in the resonator, resulting in longer interactions with the analyte. Moreover, higher Q-factor results in reduction of spectral noise, leading towards enhanced limit-of-detection (LOD) [204].

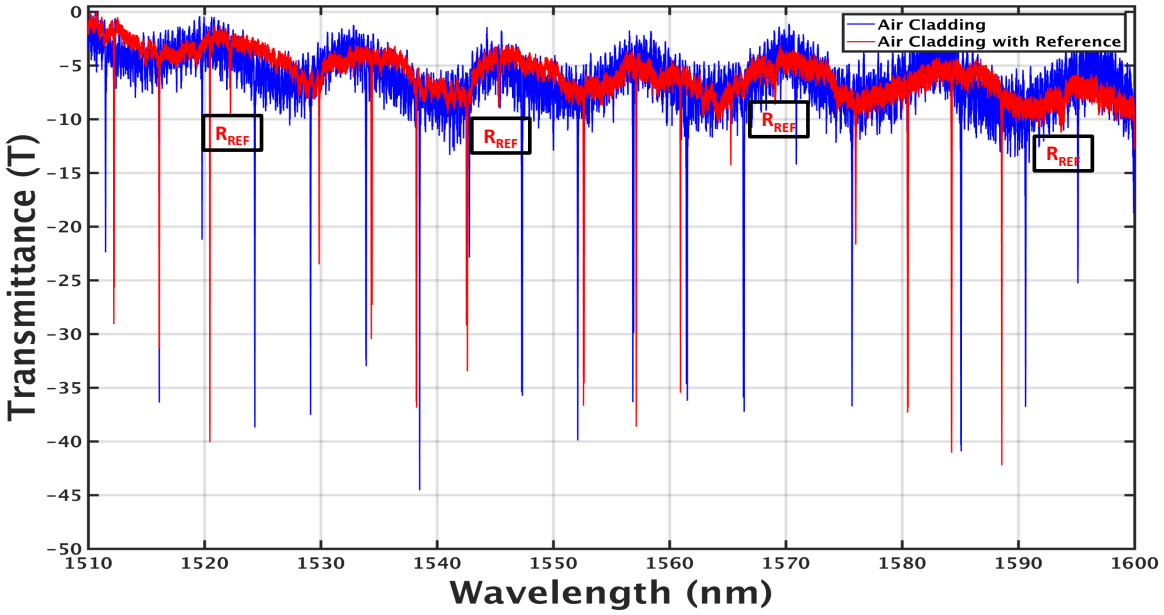

Figure 7.13: The figure shows a post-processed experimental transmission spectrum of a multiplexed ring resonator platform with and without SU-8 coated reference resonator in air cladding. The reference resonator peaks are marked on the spectrum.

7.5.3 Limit of Detection (LOD)

The LOD for a microring resonator has been defined as the minimum change in analyte refractive index the resonator is capable of detecting [204]. It is calculated as

$$LOD = \Delta n_{min} = \frac{1}{Q.S'}$$

7.6 Chemical Sensing using Optical Microresonators

7.6.1 Saltwater Analysis

Saltwater analysis has been performed to determine the sensitivities (S) and intrinsic limit of detection (LOD) of the fabricated microrings and spiral resonators to characterize their performance for advanced chemical and biosensing applications. Sodium chloride (NaCl) salt solutions are prepared in DI-water with six different concentrations i.e., 0 mM, 31.25mM, 125mM, 250mM, 500mM, and 1M. The control signal has been generated with DI-water

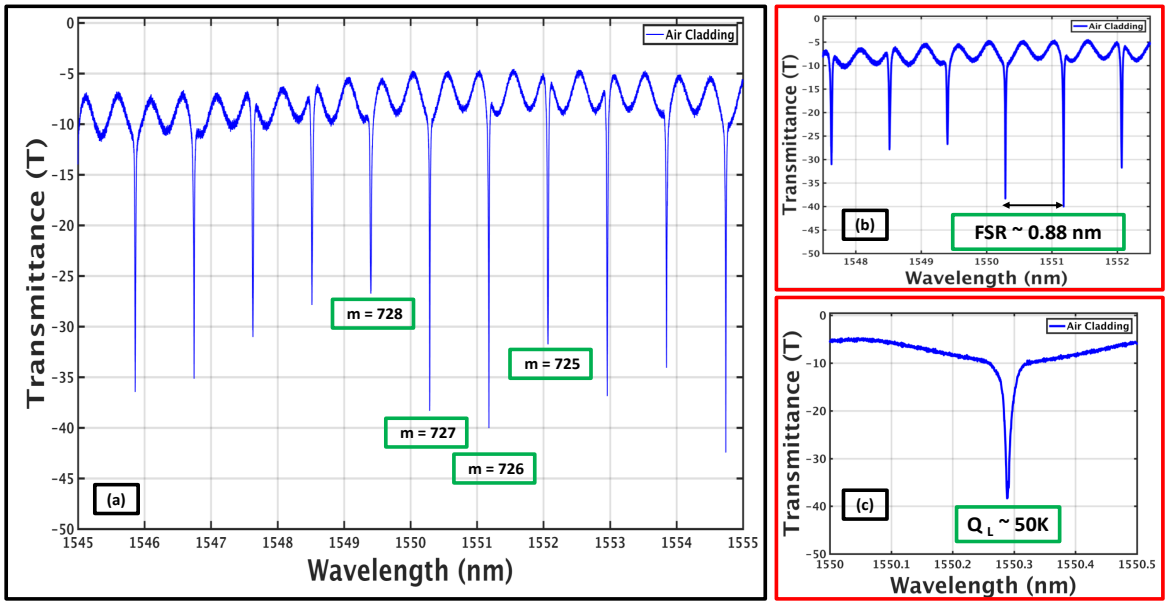

Figure 7.14: The figure shows (a) post-processed experimental transmission spectrum of a spiral ring resonator platform in air cladding, (b) shows a zoom-in version of the transmission spectrum with marked FSR of 0.88nm between azimuthal mode orders of 727 and 726, respectively, and (c) shows a single resonance peak of a spiral resonator for azimuthal mode order of 727. Loaded Q-factor of $\sim 50K$ has been observed for the fabricated device.

(i.e., 0mM).

Figure 7.16 shows the measured results for saltwater analysis for a $4\mu m$ ring resonator. The shift in resonance wavelength for one of the azimuthal mode order (i.e., m = 27) is visible from the results. A sensitivity of 112.15 nm/RIU and LOD of $\sim 10^{-5}RIU$ has been observed from the results. Figure 7.17 shows the measured results for saltwater analysis for the spiral resonators. The shift in resonance wavelength for one azimuthal mode order (i.e., m = 727) is visible from the results. A sensitivity of 108.23 nm/RIU and LOD of $\sim 10^{-5}RIU$ has been observed from the results.

7.6.2 Chemical Sensing

Chemical sensing capability for the microring resonator platform has been tested using Water (n = 1.318), Anhydrous 2-Propanol (n = 1.365), IPA (30% water, 70% 2-Propanol, n = 1.364), Methanol (n = 1.3195) , and Acetone (n = 1.3555) as chemical reagents. The

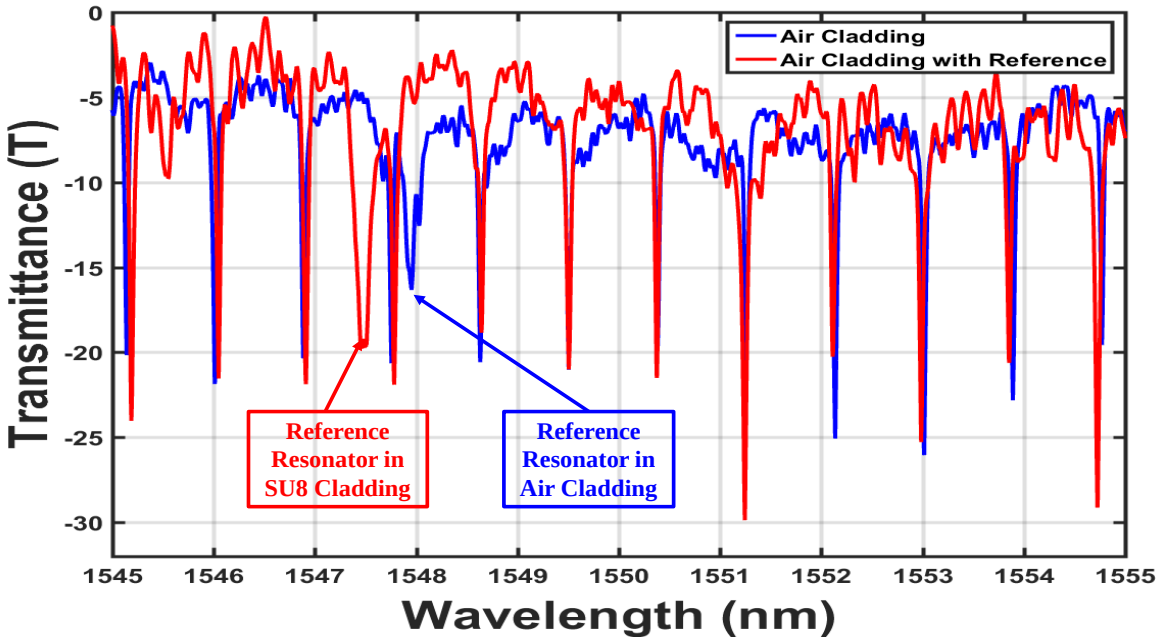

Figure 7.15: The figure shows a post-processed experimental transmission spectrum of a spiral resonator platform with and without SU-8 coated reference resonator in air cladding. The reference resonator peaks are marked on the spectrum.

shift in resonance frequency for each of the resonator has been observed. The reference resonator has also been monitored for the variation in the resonance shift. The overall shift in resonance frequency ($\Delta\lambda$) has been adjusted by subtracting the reference shift from the sensing shift to compensate the thermal drift of the resonators. Figure 7.18 shows the variation in resonance wavelength (adjusted with reference) for air-clad microring resonators for chemical sensing applications. A sensitivity of $\sim 118nm/RIU$ has been observed which corresponds to the simulated TM mode sensitivity of the microring resonators. The variation in the simulated and observed values are primarily because of the fabrication imperfections.

7.7 Biosensing Applications using Optical Microresonators

In this work, the fabricated devices (i.e., silicon ring and spiral resonators) are tested for two different chemical modification techniques to establish biomolecular attachment and sensing. The devices are silanized using (3-Aminopropyl)triethoxysilane (APTES) and (3-

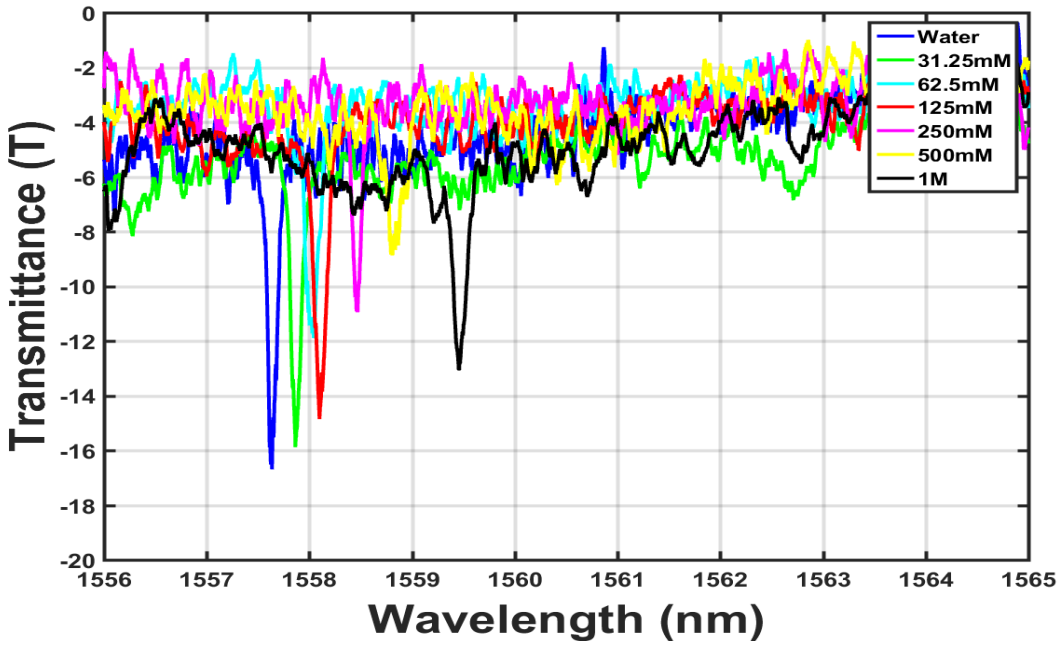

Figure 7.16: Measured results for saltwater analysis for sensing for ring resonators showing shift in resonance

Glycidyloxypropyl) trimethoxysilane (GPTMS, GPTS, GLYMO) for allowing advanced biosensing applications. Avidin protein (66 - 69 kDa) is allowed to react with the APTES silanized devices, while the SNA and MAA lectins are reacted with the GPTMS silanized devices to quantify the biomolecular attachment and sensing. The change in the resonance wavelength is evaluated for the resonators to characterize the surface attachment of the proteins.

7.7.1 Case No: 1 - Avidin attachment experiment

Device cleaning

The devices are first copiously rinsed using acetone, methanol, and isopropyl alcohol (IPA) and then dried using nitrogen gas. This is followed by Piranha (4:1 of H_2SO_4:H_2O_2) cleaning at 80°C for 30 minutes. The Piranha cleaned devices are again dried using the nitrogen gas and placed in the UV-Ozone Cleaning System (UVOCS) for 15 minutes. The

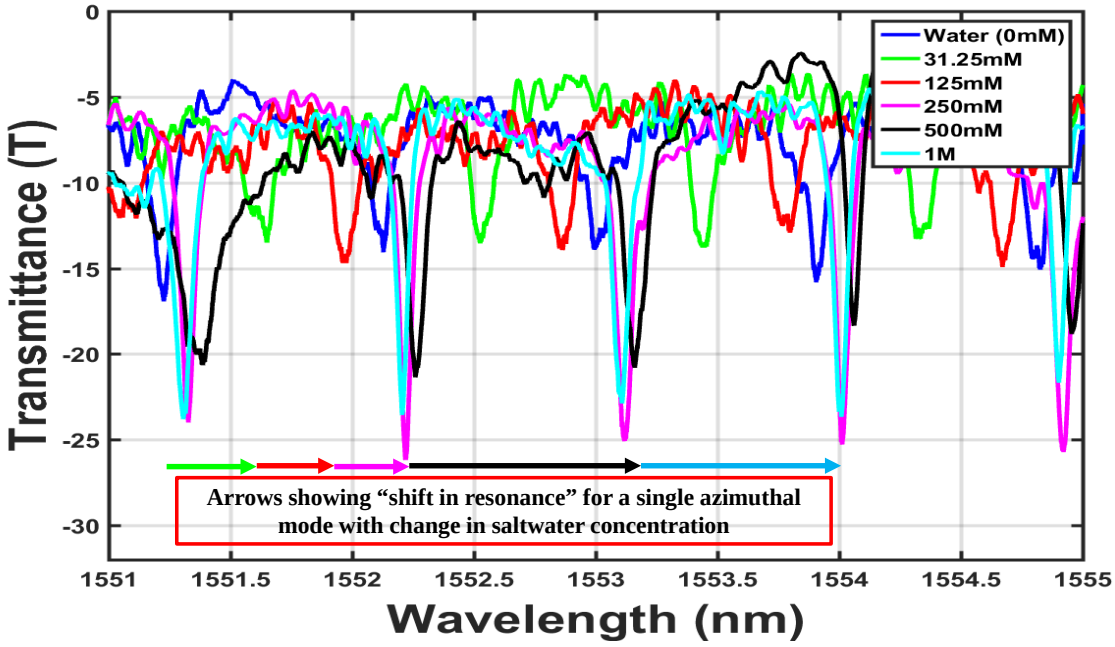

Figure 7.17: Measured results for saltwater analysis using spiral resonators showing shift in resonance wavelength

UVOCS cleaning mechanism controls the hydrophilicity of the devices by generating the -OH bonds at the surface. The devices are then rinsed with DI-water, dried using nitrogen gas, and placed over the hotplate at 110°C for 5 minutes to completely remove any moisture content. The dehydrate baking step extremely important as the silane reagents reacts with the moisture (water) and hydrolyze over the sample resulting in loss of reactivity [145].

APTES silanization

The APTES solution has been prepared with a concentration of 5% (v/v) using anhydrous 2-Propanol solvent. The solution is properly mixed together using a vortexer (Thermo Scientific) at 1500rpm for 30 seconds. $50\mu l$ of the APTES solution is then dropped over the sample (using a pipette) and the sample is incubated for 30 minutes. After the incubation, the sample is rinsed with 2-Propanol, and baked for 100°C for 15 minutes over a hotplate to achieve uniform immobilization of APTES over the surface. This process resulted in a uniform layer of APTES over the surface with a thickness of $\sim 125nm$ (measured using a

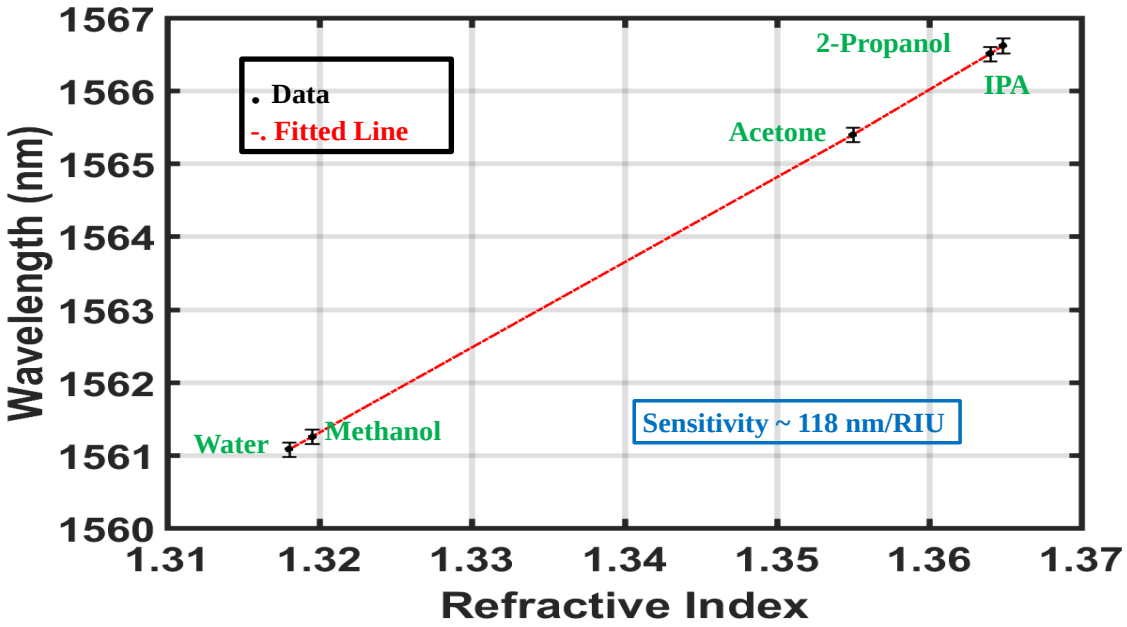

Figure 7.18: Measured results for chemical sensing for ring resonators showing variation in resonance wavelength for air-clad resonators

Woollam M2000 Ellipsometer setup). The shift in resonance is measured after the APTES functionalization for both of the devices (i.e, microring and spiral resonators).

Glutaraldehyde treatment

A 2.5% glutaraldehyde ($C_5H_8O_2$) solution in 1X-PBS (in volume ratio) is then drop-casted over the APTES treated resonator surface surface for 15 minutes to generate aldehyde functionalized surfaces. This is followed by 1X-PBS rinse to remove the unreacted glutaraldehyde solution and the shift in resonance is measured for both of the devices (i.e, microring and spiral resonators).

Avidin adsorption

Avidin is a tetrameric biotin-binding protein with an estimate size of 66 - 69 kDa. It has been used to monitor the biomolecular attachment of a protein to the aldehyde modified surfaces. A solution of $100\mu g/ml$ of egg-white Avidin in 1X-PBS has been prepared and drop-casted over the microring resonator surface to to monitor the attachment. The micror-

ing resonator (and spiral resonator) is then incubated at room temperature for 30 minutes to have a uniform adsorption over its surface. The sensor chip is then rinsed using 1X-PBS solution to remove the unreacted Avidin and the shift in resonance is measured.

7.7.2 Case No: 2 - Lectin attachment experiment

Device cleaning

The devices are first copiously rinsed using acetone, methanol, and isopropyl alcohol (IPA) and then dried using nitrogen gas. This is followed by Piranha (4:1 of H_2SO_4:H_2O_2) cleaning at 80°C for 30 minutes. The Piranha cleaned devices are again dried using the nitrogen gas and placed in the UV-Ozone Cleaning System (UVOCS) for 15 minutes. The UVOCS cleaning mechanism controls the hydrophilicity of the devices by generating the -OH bonds at the surface. The devices are then rinsed with DI-water, dried using nitrogen gas, and placed over the hotplate at 110°C for 5 minutes to completely remove any moisture content.

GPTMS silanization

The GPTMS solution has been prepared with a concentration of 5% (v/v) using anhydrous 2-Propanol solvent. The solution is properly mixed together using a vortexer (Thermo Scientific) at 1500rpm for 30 seconds. $50\mu l$ of the solution is then dropped over the sample (using a pipette) and the sample is incubated for 30 minutes. After the incubation, the sample is rinsed with 2-Propanol, and baked for 100°C for 15 minutes over a hotplate to achieve uniform immobilization of GPTMS over the surface. This process resulted in a uniform layer of GPTMS over the surface with a thickness of $\sim 3.3nm$ (measured using a Woollam M2000 Ellipsometer setup). The shift in resonance is measured after the GPTMS functionalization for both of the devices (i.e, microring and spiral resonators).

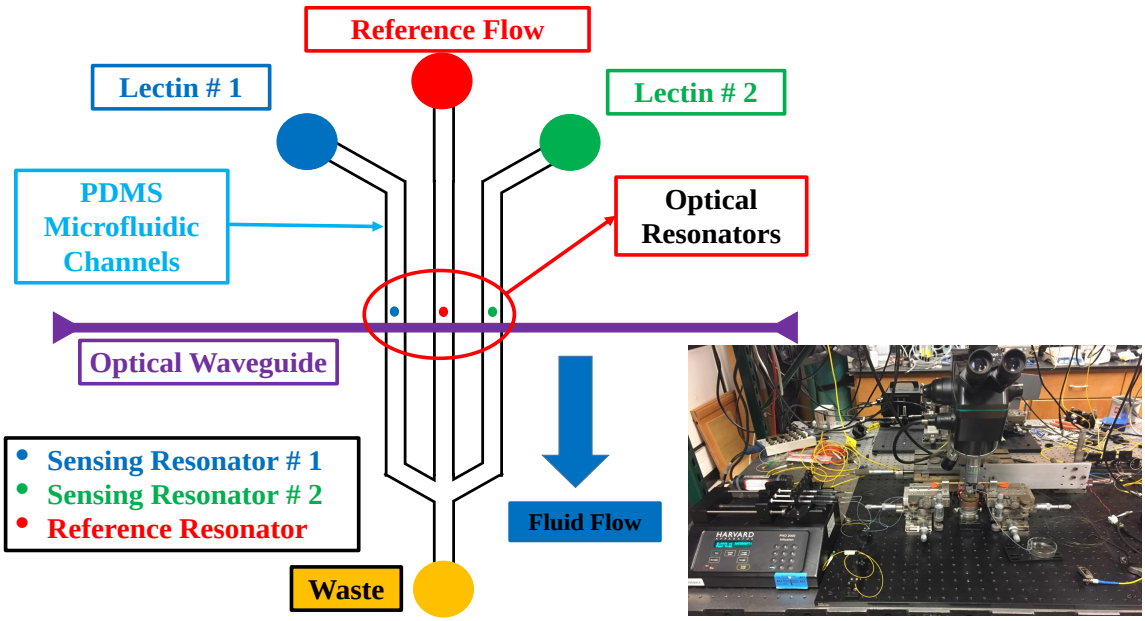

Figure 7.19: An illustration of on-flow coating and multiplexed sensing platform based on silicon microresonators. Inset shows a fabricated device under the characterization setup for realization of real-time label-free sensing using high-Q optical microresonators.

Lectin adsorption

SNA and MAA-II lectins are glycan binding proteins with an estimated size of 140 kDa and 130 kDa, respectively [205]. A solution of $100\mu g/ml$ of each of the lectins in 1X-PBS has been prepared and drop-casted over the microring resonator surface (two separate sensor chips are utilized for experiments) to monitor the attachment. The microring resonator (and spiral resonator) device is then incubated at room temperature for 30 minutes to have a uniform adsorption over its surface. The sensor chip is then rinsed using 1X-PBS solution to remove the unreacted lectins and the shift in resonance is measured.

*Note: The lectin attachment to the GPTMS surface is favored in a high humidity environment (i.e., 80% humidity). The resonator devices are incubated in a humidity chamber for the lectin attachment procedure.

Table 7.3: Measured shift in resonance wavelength for microring resonators for different surface modification protocols

Observations	Silanization		Glutaraldehyde Treatment	Biomolecular Attachment		
	APTES	GPTMS		Avidin	SNA Lectin	MAA Lectin
Shift in Resonance (nm)	49.82	4.876	6.678	3.127	2.076	1.729

7.8 On-flow coating and multiplexed sensing demonstration

I have designed and fabricated a microfluidic platform, coupled with densely integrated on-chip high-Q SOI optical microresonators, to demonstrate real time, on-flow label-free multiplexed sensing. Figure 7.19 shows a pictorial representation of the designed platform, while inset shows a fabricated device under the characterization setup for realization of real-time label-free sensing using high-Q optical microresonators.

7.9 Conclusion

I have designed high-Q optical microring and spiral resonators in SOI platform to work as highly sensitive, compact, and scalable transducers, enabling a versatile realization of highly multiplexed and array based chemical and biological sensing platforms. I have also demonstrated the integration of microfluidics with the sensing transducers, allowing on demand delievery of extremely small volumes of chemical and biological analytes, resulting in realization of advanced LOC solutions for various chemical and biological sensing applications.

A highly multiplexed refractive index based sensing platform has been demonstrated based on high-Q microring structures which allows independent and individual monitoring of each of the microring sensing element at its corresponding wavelength. The platform has been design in such a fashion that when simultaneously excited, the corresponding resonance frequencies are evenly spaced in the desired FSR range without any spectral overlap. Similarly, a high-Q spiral resonator based sensing platform has been demonstrated, providing a higher sensing area in a small footprint. The designed spiral resonator platform

provided a small footprint of $50\mu m$ by $50\mu m$, and a sensing area more than 6 times of a microring in a similar footprint. Q-factors of $\sim 50K$ has been achieved for both of the designs. The sensitivity performance of $\sim 0.43pg/(mm^2.pm)$, a minimum LOD for mass sensing as $\sim 0.5pg/mm^2$, and a minimum resolution of $1pm$ has been demonstrated for biosensing applications [200].

Another aspect is the optimization of the nanofabrication processes, and repeatability of fabrication for these sensing platforms. I have designed and demonstrated these devices in a manner to be compatible with single step electron beam lithography, single step etching, and extremely low-cost industrial grade microfluidic platform integration. This has enabled me to achieve lower cost of fabrication, device complexity, and much faster lab-to-market time.

CHAPTER 8
CONCLUSION

8.1 Summary of the Work

The objective of this thesis is to investigate and demonstrate compact lab-on-a-chip (LOC) sensor for the Post Translational Modification (PTM) profiling of the proteins used as biomarkers, for early cancer detection. The LOC sensor comprises of an on-chip pre-concentration and filtering device to isolate the targeted low-abundance proteins form the complex input samples and an integrated photonic sensor microarray for profiling the molecular structures of the isolated protein epitopes. The motivation of this work has been extracted from the lack of ability of conventional affinity-based pre-concentration and separation techniques for elucidating PTMs of the proteins, and the unavailability of LOC sensors for this task. The multi-disciplinary research has been focused towards the integration of functional proteomics, microfluidics, and nanofabrication, employing principles of theoretical modeling and simulations, microfluidics, surface chemistry, and nano-optics for the realization of a novel integrated LOC platform for pre-concentration, filtration, and label-free detection of proteins and biomarkers.

8.2 Technical Contributions

8.2.1 Demonstration of affinity-based multiplexed biomolecular capturing and release using miniaturized PDMS micropillar-based platform

I have demonstrated biomolecular (i.e., proteins and biomarkers) filtering and pre-concentration based on an affinity-based separation approach. The target biomolecules are captured and pre-concentrated on the PDMS-based micropillars. The micropillar's surface is specifically functionalized with the specific affinity epitopes corresponding to the biomolecules for en-

hanced affinity-based capturing. The pre-concentrated biomolecules are then released on demand and can be recaptured on a sensing transducer (e.g., optical sensor arrays), allowing a complete label-free sensing and profiling (secondary epitopes such as glycoforms) of the biomolecules.

I demonstrated a multi-step surface functionalization protocol to optimize on-the-flow surface functionalization and capturing efficiency of the biomolecules in a PDMS-based microfluidic platform. I designed, optimized, fabricated, and characterized a PDMS-based microfluidic platform, having a micropillar based biomolecular pre-concentration chamber allowing increased surface-to-volume ratio (SVR) for enhanced biomolecular filtering and preconcentration. The surface of the pre-concentrator chamber is functionalized with the Avidin protein, followed by the use of a biotinylated photo-cleavable (PC) linker conjugated with the biomolecular specific antibodies (i.e., anti-PSA IgGs). The use of PC-biotin linker is the key towards solving the challenges such as sample degradation, introduction of contaminants (due to the release of non-specifically bound proteins), and elution of endogenous proteins (along with the desired protein) [23], faced while releasing the pre-concentration samples from microfluidic devices.

I effectively demonstrated the capture and release of IgG proteins (from Rabbit serum) and PSA cancer biomarkers (fPSA, human serum) using the PC-biotin linker with clinically relevant sample concentrations and volumes. I also demonstrated the capability of multiplexed glycoprofiling for elucidating the PTMs of the PSA cancer biomarker using the SNA and MAA-II lectins. A dynamic working range of $\sim$ 10 orders of magnitude higher compared the commercially available ELISA kit for PSA detection (i.e., $0.01ng/ml$ to $12ng/ml$ for fPSA ELISA kit [192]), has been achieved using the designed PDMS-based micropillar pre-concentration platform. Overall, a minimum LOD of $\sim 10pg/ml$ and a LOQ of $\sim$ $20pg/ml$ has been been achieved for on-chip multiplexed PSA pre-concentration, detection, and glycoprofiling.

8.2.2 Demonstration of nanoporous MWCNT forests and micropillars for multiplexed on-chip biomolecular capturing and release

I demonstrated the use of carbon nanotubes (CNTs) as high porosity material for enhanced on-chip biomolecular pre-concentration applications. I fabricated and utilized CNTs forests and micropillar structures over a silicon substrate to increase the effective surface area of a microfluidic pre-concentrator device. These CNTs grown are multi-walled (concentric walls) with an average height of $\sim 30\mu m$, average diameter of $\sim 8nm - 12nm$, and an average intra-CNT spacing of $\sim 80 - 100nm$, leading to a volume fraction of less than $1\% - 2\%$ CNTs. This resulted in an increased surface are for biomolecular capturing applications.

The MWCNT forests and micropillars has been grown over a silicon substrate, aligned, and bonded with the PDMS based microfluidic channels to develop the biomolecular pre-concentrator and filtering devices. The capturing efficiency and performance of these designed MWCNT forests and micropillar-based pre-concentration platforms have been assessed by employing the PC-biotin linker-based modified lectin immunoassay for the PSA biomarker capturing, pre-concentration, glycoprofiling, and release. The capability of multiplexed glycoprofiling for elucidating the PTMs of the PSA cancer biomarker has been demonstrated by using the SNA and MAA-II lectins. An estimated minimum LOD of $\sim 0.5pg/ml$ and a LOQ of $\sim 1pg/ml$ can be achieved for on-chip multiplexed PSA pre-concentration, detection, and glycoprofiling using the MWCNT forest based platform.

8.2.3 Demonstration of high-Q SOI microresonators with high repeatability, for multiplexed and array based sensing application

I have designed high-Q optical microring and spiral resonators in SOI platform to work as highly sensitive, compact, and scalable transducers, enabling a versatile realization of highly multiplexed and array based chemical and biological sensing platforms. I have also demonstrated the integration of microfluidics with the sensing transducers, allowing on

demand delievery of extremely small volumes of chemical and biological analytes, resulting in realization of advanced LOC solutions for various chemical and biological sensing applications.

A highly multiplexed refractive index based sensing platform has been demonstrated based on high-Q microring structures which allows independent and individual monitoring of each of the microring sensing element at its corresponding wavelength. The platform has been design in such a fashion that when simultaneously excited, the corresponding resonance frequencies are evenly spaced in the desired FSR range without any spectral overlap. Similarly, a high-Q spiral resonator based sensing platform has been demonstrated, providing a higher sensing area in a small footprint. The designed spiral resonator platform provided a small footprint of $50\mu m$ by $50\mu m$, and a sensing area more than 6 times of a microring in a similar footprint. Q-factors of $\sim 50K$ has been achieved for both of the designs. The sensitivity performance of $\sim 0.43pg/(mm^2.pm)$, a minimum LOD for mass sensing as $\sim 0.5pg/mm^2$, and a minimum resolution of $1pm$ has been demonstrated for biosensing applications [200].

Another aspect is the optimization of the nanofabrication processes, and repeatability of fabrication for these sensing platforms. I have designed and demonstrated these devices in a manner to be compatible with single step electron beam lithography, single step etching, and extremely low-cost industrial grade microfluidic platform integration. This has enabled me to achieve lower cost of fabrication, device complexity, and much faster lab-to-market time.

8.3 Future Work

In the end, I would like to briefly discuss a few possible extensions of the work performed in this thesis.

- I have demonstrated on-chip capturing and pre-concentration, release, glycoprofiling, and multiplexed detection of PSA biomarker using PDMS-based microfluidic plat-

form and high-Q optical microresonators. A single chip platform having enhanced fluid handling with the help of on-chip valves and pressure controllers, along with densely integrated optical transducers for enhanced multiplexed sensing and glyco-profiling of biomarkers can be a way forwards for commercialization of a complete product.

- I have demonstrated the biomolecular capturing, pre-concentration, release, glyco-profiling, and multiplexed sensing by tailoring and optimizing the universally accepted chemical strategies. There lies a great potential for improvement and modification of these recipes and procedures for elucidating various other biomolecules such as cancer biomarkers, proteins, DNAs, viruses, glucose, and aptamers.

- The use of nanophotonics and advanced nanofabrication techniques have allowed us to realize biosensing platforms in Si that can decrease the existing clinical LODs for various biomarker sensing applications. Optical material platforms such as SiN, can be another interesting choice apart from the ubiquitous Si, as it provides a window in visible spectrum regime.

Appendices

APPENDIX A

LIST OF CHEMICALS

All the fabrication equipment and cleaning solutions has been provided at the IEN clean-room utility of the Georgia Institute of Technology, Atlanta, US.

Table A.1: List of chemicals and related equipment used for the experiments

No.	Item Name	Manufacturer
1	(3-aminopropyl)triethoxysilane (APTES)	Sigma Aldrich
2	(3-Mercaptopropyl)trimethoxysilane (MPTMS)	Sigma Aldrich
3	2-Propanol (98% Pure)	Sigma Aldrich
4	(3-Dimethylaminopropyl) - N- ethylcarbodiimide hydrochloride (EDC)	Sigma Aldrich
5	N - Hydroxysuccinimide (NHS)	Sigma Aldrich
6	Glutaraldehyde	Sigma Aldrich
7	(3-Glycidyloxypropyl)trimethoxysilane (GPTMS)	Sigma Aldrich
8	Bovine Serum Albumin (BSA)	Sigma Aldrich
9	Tween-20	Sigma Aldrich
10	ATTO 520-Biotin	Sigma Aldrich
11	Avidin (from egg white, lyophilized powder), FITC Conjugate	Sigma Aldrich
12	Sodium Cyanoborohydride	Sigma Aldrich
13	Sodium Periodate	Sigma Aldrich
14	Sodium Acetate	Sigma Aldrich
15	Ethanolamine	Sigma Aldrich
16	Sodium Hydroxide Powder	Sigma Aldrich
17	Photocleavable - Biotin - NHS - Ester	Sigma Aldrich
18	IgG (from Rabbit Serum)	Sigma Aldrich
19	Anti-Rabbit IgG (whole molecule)FITC antibody	Sigma Aldrich
20	Bovine Serum Albumin (BSA)	Sigma Aldrich
21	Amicon Ultra-0.5 Centrifugal Filter Unit with Ultracel-100	Sigma Aldrich
22	N,N-Dimethylformamide	Sigma Aldrich
23	Dimethyl sulfoxide (DMSO)	Sigma Aldrich
24	2-(N-morpholino)ethanesulfonic acid (MES)	Sigma Alrdich
25	Albumin from Bovine Serum (BSA), FITC Conjugate	Thermofisher Scientific
26	Phosphate Buffer Saline(1X-PBS, pH 7.4)	Thermofisher Scientific
27	Avidin (from egg white)	Thermofisher Scientific
28	Sylgard 184 Silicone Elastomer Kit	Dow Corning Corporation
29	SU 8 2000 Series Photo Resists (2000.5, 2010, 2015, 2035)	MicroChem
30	SU8 Developer	MicroChem
31	Silicon Wafers	Wafer - Pro, US
32	Glass Wafers	University Wafers
33	Transparency Photomask	CAD/Art Services
34	ELISA Synblock	BioRad
35	PSA Protein	Fitzgerald Industries
36	PSA antibodies	Fitzgerald Industries
37	Maackia amurensis Lectin - MAA/MAL II - FITC	BioWorld
38	Unconjugated Maackia Amurensis Lectin II (MAL II)	Vector Labs
39	Cy5 labeled Sambucus Nigra Lectin (Cy5-SNA)	Vector Labs
40	Unconjugated Sambucus Nigra Lectin (SNA)	Vector Labs

REFERENCES

[1] R.L.Siegel, K.D.Miller, and A.Jemal, "Cancer statistics, 2018," *CA : A Cancer Journal for Clinicians*, vol. 68, no. 1, pp. 7–30, 2018.

[2] J. R. Prensner, M. A. Rubin, J. T. Wei, and A. M. Chinnaiyan, "Beyond psa: The next generation of prostate cancer biomarkers," *Science translational medicine*, vol. 4, no. 127, 127rv3–127rv3, 2012.

[3] J. Gildersleeve, C. Campbell, O. Oyelaran, J. Gulley, and J. Schlom, *Biomarkers for prostate cancer and methods for their detection*, US Patent 9,804,163, 2017.

[4] D. V. Makarov, S. Loeb, R. H. Getzenberg, and A. W. Partin, "Biomarkers for prostate cancer," *Annual review of medicine*, vol. 60, pp. 139–151, 2009.

[5] B. Adamczyk, T. Tharmalingam, and P. M. Rudd, "Glycans as cancer biomarkers," *Biochimica et Biophysica Acta (BBA)-General Subjects*, vol. 1820, no. 9, pp. 1347–1353, 2012.

[6] C. R. Yonzon, D. A. Stuart, X. Zhang, A. D. McFarland, C. L. Haynes, and R. P. Van Duyne, "Towards advanced chemical and biological nanosensorsan overview," *Talanta*, vol. 67, no. 3, pp. 438–448, 2005.

[7] P. M. Valencia, O. C. Farokhzad, R. Karnik, and R. Langer, "Microfluidic technologies for accelerating the clinical translation of nanoparticles," *Nature nanotechnology*, vol. 7, no. 10, pp. 623–629, 2012.

[8] H. Lodish and S. L. Zipursky, "Molecular cell biology," *Biochemistry and Molecular Biology Education*, vol. 29, pp. 126–133, 2001.

[9] J. Möller, M. A. Schroer, M. Erlkamp, S. Grobelny, M. Paulus, S. Tiemeyer, F. J. Wirkert, M. Tolan, and R. Winter, "The effect of ionic strength, temperature, and pressure on the interaction potential of dense protein solutions: From nonlinear pressure response to protein crystallization," *Biophysical journal*, vol. 102, no. 11, pp. 2641–2648, 2012.

[10] A. J. de Mello and N. Beard, "Focus. dealing with realsamples: Sample pre-treatment in microfluidic systems," *Lab on a Chip*, vol. 3, no. 1, 11N–20N, 2003.

[11] S. Song and A. K. Singh, "On-chip sample preconcentration for integrated microfluidic analysis," *Analytical and bioanalytical chemistry*, vol. 384, no. 1, pp. 41–43, 2006.

[12] B. Jung, R. Bharadwaj, and J. G. Santiago, "Thousandfold signal increase using field-amplified sample stacking for on-chip electrophoresis," *Electrophoresis*, vol. 24, no. 19-20, pp. 3476–3483, 2003.

[13] J. Wang, Y. Zhang, M. R. Mohamadi, N. Kaji, M. Tokeshi, and Y. Baba, "Exceeding 20 000-fold concentration of protein by the on-line isotachophoresis concentration in poly (methyl methacrylate) microchip," *Electrophoresis*, vol. 30, no. 18, pp. 3250–3256, 2009.

[14] Y. Li, D. L. DeVoe, and C. S. Lee, "Dynamic analyte introduction and focusing in plastic microfluidic devices for proteomic analysis," *Electrophoresis*, vol. 24, no. 1-2, pp. 193–199, 2003.

[15] J. D. Ramsey and G. E. Collins, "Integrated microfluidic device for solid-phase extraction coupled to micellar electrokinetic chromatography separation," *Analytical chemistry*, vol. 77, no. 20, pp. 6664–6670, 2005.

[16] K.-T. Liao and C.-F. Chou, "Nanoscale molecular traps and dams for ultrafast protein enrichment in high-conductivity buffers," *Journal of the American Chemical Society*, vol. 134, no. 21, pp. 8742–8745, 2012.

[17] S. J. Kim, Y.-A. Song, and J. Han, "Nanofluidic concentration devices for biomolecules utilizing ion concentration polarization: Theory, fabrication, and applications," *Chemical Society Reviews*, vol. 39, no. 3, pp. 912–922, 2010.

[18] J. M. T. Berg, L John, L. Stryer, J. M. Berg, J. L. Tymoczko, L. Stryer, *et al.*, "Biochemistry," 2002.

[19] A. Ríos, A. Escarpa, M. C. González, and A. G. Crevillén, "Challenges of analytical microsystems," *TrAC Trends in Analytical Chemistry*, vol. 25, no. 5, pp. 467–479, 2006.

[20] M. E. Sandison, S. A. Cumming, W. Kolch, and A. R. Pitt, "On-chip immunoprecipitation for protein purification," *Lab on a Chip*, vol. 10, no. 20, pp. 2805–2813, 2010.

[21] ThermoFisher, *Overview of affinity purification*, ThermoFisher Website, 2017.

[22] P. B. R. Library. (2017). Avidin-biotin interaction.

[23] M. Fonović, S. H. Verhelst, M. T. Sorum, and M. Bogyo, "Proteomics evaluation of chemically cleavable activity-based probes," *Molecular & Cellular Proteomics*, vol. 6, no. 10, pp. 1761–1770, 2007.

[24] F. Guillier, D. Orain, and M. Bradley, "Linkers and cleavage strategies in solid-phase organic synthesis and combinatorial chemistry," *Chemical Reviews*, vol. 100, no. 6, pp. 2091–2158, 2000.

[25] Y. Oda, T. Nagasu, and B. T. Chait, "Enrichment analysis of phosphorylated proteins as a tool for probing the phosphoproteome," *Nature biotechnology*, vol. 19, no. 4, pp. 379–382, 2001.

[26] C. A. Gartner, J. E. Elias, C. E. Bakalarski, and S. P. Gygi, "Catch-and-release reagents for broadscale quantitative proteomics analyses," *Journal of proteome research*, vol. 6, no. 4, pp. 1482–1491, 2007.

[27] S. H. Verhelst, M. Fonović, and M. Bogyo, "A mild chemically cleavable linker system for functional proteomic applications," *Angewandte Chemie*, vol. 119, no. 8, pp. 1306–1308, 2007.

[28] A. E. Speers and B. F. Cravatt, "A tandem orthogonal proteolysis strategy for high-content chemical proteomics," *Journal of the American Chemical Society*, vol. 127, no. 28, pp. 10 018–10 019, 2005.

[29] J. Szychowski, A. Mahdavi, J. J. Hodas, J. D. Bagert, J. T. Ngo, P. Landgraf, D. C. Dieterich, E. M. Schuman, and D. A. Tirrell, "Cleavable biotin probes for labeling of biomolecules via azide- alkyne cycloaddition," *Journal of the American Chemical Society*, vol. 132, no. 51, pp. 18 351–18 360, 2010.

[30] P. P. Geurink, B. I. Florea, N. Li, M. D. Witte, J. Verasdonck, C.-L. Kuo, G. A. van der Marel, and H. S. Overkleeft, "A cleavable linker based on the levulinoyl ester for activity-based protein profiling," *Angewandte Chemie International Edition*, vol. 49, no. 38, pp. 6802–6805, 2010.

[31] J. Olejnik, S. Sonar, E. Krzymanska-Olejnik, and K. J. Rothschild, "Photocleavable biotin derivatives: A versatile approach for the isolation of biomolecules," *Proceedings of the National Academy of Sciences*, vol. 92, no. 16, pp. 7590–7594, 1995.

[32] D. Maurel, S. Banala, T. Laroche, and K. Johnsson, "Photoactivatable and photoconvertible fluorescent probes for protein labeling," *ACS chemical biology*, vol. 5, no. 5, pp. 507–516, 2010.

[33] E. Stern, A. Vacic, N. K. Rajan, J. M. Criscione, J. Park, B. R. Ilic, D. J. Mooney, M. A. Reed, and T. M. Fahmy, "Label-free biomarker detection from whole blood," *Nature nanotechnology*, vol. 5, no. 2, pp. 138–142, 2010.

[34] H. Becker and L. E. Locascio, "Polymer microfluidic devices," *Talanta*, vol. 56, no. 2, pp. 267–287, 2002.

[35] Y. Xia and G. M. Whitesides, "Soft lithography," *Annual review of materials science*, vol. 28, no. 1, pp. 153–184, 1998.

[36] E. D. Goluch, J.-M. Nam, D. G. Georganopoulou, T. N. Chiesl, K. A. Shaikh, K. S. Ryu, A. E. Barron, C. A. Mirkin, and C. Liu, "A bio-barcode assay for on-chip attomolar-sensitivity protein detection," *Lab on a Chip*, vol. 6, no. 10, pp. 1293–1299, 2006.

[37] J. Campbell, N. R. Pollock, A. Sharon, and A. F. Sauer-Budge, "Development of an automated on-chip bead-based elisa platform," *Analytical Methods*, vol. 7, no. 19, pp. 8472–8477, 2015.

[38] M. Zimmermann, E. Delamarche, M. Wolf, and P. Hunziker, "Modeling and optimization of high-sensitivity, low-volume microfluidic-based surface immunoassays," *Biomedical microdevices*, vol. 7, no. 2, pp. 99–110, 2005.

[39] D. R. Kim and X. Zheng, "Numerical characterization and optimization of the microfluidics for nanowire biosensors," *Nano letters*, vol. 8, no. 10, pp. 3233–3237, 2008.

[40] T. M. Squires, R. J. Messinger, and S. R. Manalis, "Making it stick: Convection, reaction and diffusion in surface-based biosensors," *Nature biotechnology*, vol. 26, no. 4, pp. 417–426, 2008.

[41] C.-C. Lin, J.-H. Wang, H.-W. Wu, and G.-B. Lee, "Microfluidic immunoassays," *JALA: Journal of the Association for Laboratory Automation*, vol. 15, no. 3, pp. 253–274, 2010.

[42] H.-Y. Li, V. Dauriac, V. Thibert, H. Senechal, G. Peltre, X.-X. Zhang, and S. Descroix, "Micropillar array chips toward new immunodiagnosis," *Lab on a Chip*, vol. 10, no. 19, pp. 2597–2604, 2010.

[43] E Eteshola and D Leckband, "Development and characterization of an elisa assay in pdms microfluidic channels," *Sensors and Actuators B: Chemical*, vol. 72, no. 2, pp. 129–133, 2001.

[44] D. Kim and A. E. Herr, "Protein immobilization techniques for microfluidic assays," *Biomicrofluidics*, vol. 7, no. 4, p. 041 501, 2013.

[45] H. Jiang, X. Weng, and D. Li, "Microfluidic whole-blood immunoassays," *Microfluidics and nanofluidics*, vol. 10, no. 5, pp. 941–964, 2011.

[46] P. Stroeve and N. Ileri, "Biotechnical and other applications of nanoporous membranes," *Trends in biotechnology*, vol. 29, no. 6, pp. 259–266, 2011.

[47] S. P. Adiga, L. A. Curtiss, J. W. Elam, M. J. Pellin, C.-C. Shih, C.-M. Shih, S.-J. Lin, Y.-Y. Su, S. D. Gittard, J. Zhang, *et al.*, "Nanoporous materials for biomedical devices," *JOM Journal of the Minerals, Metals and Materials Society*, vol. 60, no. 3, pp. 26–32, 2008.

[48] G. D. Chen, F. Fachin, M. Fernandez-Suarez, B. L. Wardle, and M. Toner, "Nanoporous elements in microfluidics for multiscale manipulation of bioparticles," *Small*, vol. 7, no. 8, pp. 1061–1067, 2011.

[49] S. P. Adiga, C. Jin, L. A. Curtiss, N. A. Monteiro-Riviere, and R. J. Narayan, "Nanoporous membranes for medical and biological applications," *Wiley Interdisciplinary Reviews: Nanomedicine and Nanobiotechnology*, vol. 1, no. 5, pp. 568–581, 2009.

[50] F. Fachin, G. D. Chen, M. Toner, and B. L. Wardle, "Integration of bulk nanoporous elements in microfluidic devices with application to biomedical diagnostics," *Journal of Microelectromechanical Systems*, vol. 20, no. 6, pp. 1428–1438, 2011.

[51] M. Meyyappan, L. Delzeit, A. Cassell, and D. Hash, "Carbon nanotube growth by pecvd: A review," *Plasma Sources Science and Technology*, vol. 12, no. 2, p. 205, 2003.

[52] G. D. Chen, F. Fachin, E. Colombini, B. L. Wardle, and M. Toner, "Nanoporous micro-element arrays for particle interception in microfluidic cell separation," *Lab on a Chip*, vol. 12, no. 17, pp. 3159–3167, 2012.

[53] C. B. Jacobs, M. J. Peairs, and B. J. Venton, "Review: Carbon nanotube based electrochemical sensors for biomolecules," *Analytica Chimica Acta*, vol. 662, no. 2, pp. 105–127, 2010.

[54] R. Malhotra, V. Patel, J. P. Vaqué, J. S. Gutkind, and J. F. Rusling, "Ultrasensitive electrochemical immunosensor for oral cancer biomarker il-6 using carbon nanotube forest electrodes and multilabel amplification," *Analytical chemistry*, vol. 82, no. 8, pp. 3118–3123, 2010.

[55] B. V. Chikkaveeraiah, A. Bhirde, R. Malhotra, V. Patel, J. S. Gutkind, and J. F. Rusling, "Single-wall carbon nanotube forest arrays for immunoelectrochemical measurement of four protein biomarkers for prostate cancer," *Analytical chemistry*, vol. 81, no. 21, pp. 9129–9134, 2009.

[56] P. Hu, T. Tanii, G.-J. Zhang, T. Hosaka, and I. Ohdomari, "Ultrasensitive detection of biomolecules using functionalized multi-walled carbon nanotubes," *Sensors and Actuators B: Chemical*, vol. 124, no. 1, pp. 161–166, 2007.

[57] J. Choi and Y. Zhang, *Single, double, multiwall carbon nanotube properties & applications*, Sigma Aldrich Website, 2017.

[58] H.-C. Wu, X. Chang, L. Liu, F. Zhao, and Y. Zhao, "Chemistry of carbon nanotubes in biomedical applications," *Journal of Materials Chemistry*, vol. 20, no. 6, pp. 1036–1052, 2010.

[59] M. Walker, D. Burns, C. Elliott, M. Gowland, and E. C. Mills, "Is food allergen analysis flawed? health and supply chain risks and a proposed framework to address urgent analytical needs," *Analyst*, vol. 141, no. 1, pp. 24–35, 2016.

[60] ThermoFisher, *Overview of post-translational modifications (ptms)*, ThermoFisher Website, 2017.

[61] H. Li, L. Wei, P. Fang, and P. Yang, "Recent advances in the fabrication and detection of lectin microarrays and their application in glycobiology analysis," *Analytical Methods*, vol. 6, no. 7, pp. 2003–2014, 2014.

[62] R. Apweiler, H. Hermjakob, and N. Sharon, "On the frequency of protein glycosylation, as deduced from analysis of the swiss-prot database," *Biochimica et Biophysica Acta (BBA)-General Subjects*, vol. 1473, no. 1, pp. 4–8, 1999.

[63] D. Pihíková, P. Kasák, and J. Tkac, "Glycoprofiling of cancer biomarkers: Label-free electrochemical lectin-based biosensors," *Open Chem.*, vol. 13, no. 1, pp. 636–655, 2015.

[64] L. Krishnamoorthy and L. K. Mahal, "Glycomic analysis: An array of technologies," *ACS chemical biology*, vol. 4, no. 9, pp. 715–732, 2009.

[65] N. F. Reuel, B. Mu, J. Zhang, A. Hinckley, and M. S. Strano, "Nanoengineered glycan sensors enabling native glycoprofiling for medicinal applications: Towards profiling glycoproteins without labeling or liberation steps," *Chemical Society Reviews*, vol. 41, no. 17, pp. 5744–5779, 2012.

[66] W. R. Alley Jr, B. F. Mann, and M. V. Novotny, "High-sensitivity analytical approaches for the structural characterization of glycoproteins," *Chemical reviews*, vol. 113, no. 4, pp. 2668–2732, 2013.

[67] L. Krishnamoorthy and L. K. Mahal, "Lectin microarrays: Simple tools for the analysis of complex glycans," in *Functional and Structural Proteomics of Glycoproteins*, Springer, 2010, pp. 91–102.

[68] K. T. Pilobello, L. Krishnamoorthy, D. Slawek, and L. K. Mahal, "Development of a lectin microarray for the rapid analysis of protein glycopatterns," *Chembiochem*, vol. 6, no. 6, pp. 985–989, 2005.

[69] A. Kuno, N. Uchiyama, S. Koseki-Kuno, Y. Ebe, S. Takashima, M. Yamada, and J. Hirabayashi, "Evanescent-field fluorescence-assisted lectin microarray: A new strategy for glycan profiling," *Nature methods*, vol. 2, no. 11, pp. 851–856, 2005.

[70] K. T. Pilobello, D. E. Slawek, and L. K. Mahal, "A ratiometric lectin microarray approach to analysis of the dynamic mammalian glycome," *Proceedings of the National Academy of Sciences*, vol. 104, no. 28, pp. 11 534–11 539, 2007.

[71] H. Tateno, N. Uchiyama, A. Kuno, A. Togayachi, T. Sato, H. Narimatsu, and J. Hirabayashi, "A novel strategy for mammalian cell surface glycome profiling using lectin microarray," *Glycobiology*, vol. 17, no. 10, pp. 1138–1146, 2007.

[72] K.-L. Hsu and L. K. Mahal, "A lectin microarray approach for the rapid analysis of bacterial glycans," *Nature protocols*, vol. 1, no. 2, pp. 543–549, 2006.

[73] L. Krishnamoorthy, J. W. Bess, A. B. Preston, K. Nagashima, and L. K. Mahal, "Hiv-1 and microvesicles from t cells share a common glycome, arguing for a common origin," *Nature chemical biology*, vol. 5, no. 4, pp. 244–250, 2009.

[74] D. Weinrich, P. Jonkheijm, C. M. Niemeyer, and H. Waldmann, "Applications of protein biochips in biomedical and biotechnological research," *Angewandte Chemie International Edition*, vol. 48, no. 42, pp. 7744–7751, 2009.

[75] F. Rusmini, Z. Zhong, and J. Feijen, "Protein immobilization strategies for protein biochips," *Biomacromolecules*, vol. 8, no. 6, pp. 1775–1789, 2007.

[76] P. Jonkheijm, D. Weinrich, H. Schröder, C. M. Niemeyer, and H. Waldmann, "Chemical strategies for generating protein biochips," *Angewandte Chemie International Edition*, vol. 47, no. 50, pp. 9618–9647, 2008.

[77] J. Wang, "Survey and summary: From dna biosensors to gene chips," *Nucleic acids research*, vol. 28, no. 16, pp. 3011–3016, 2000.

[78] Y. Cui, Q. Wei, H. Park, and C. M. Lieber, "Nanowire nanosensors for highly sensitive and selective detection of biological and chemical species," *Science*, vol. 293, no. 5533, pp. 1289–1292, 2001.

[79] J. Kim, J. Cho, P. M. Seidler, N. E. Kurland, and V. K. Yadavalli, "Investigations of chemical modifications of amino-terminated organic films on silicon substrates and controlled protein immobilization," *Langmuir*, vol. 26, no. 4, pp. 2599–2608, 2010.

[80] M Grundner and H Jacob, "Investigations on hydrophilic and hydrophobic silicon (100) wafer surfaces by x-ray photoelectron and high-resolution electron energy loss-spectroscopy," *Applied Physics A*, vol. 39, no. 2, pp. 73–82, 1986.

[81] A. P. Turner, "Biosensors: Sense and sensibility," *Chemical Society Reviews*, vol. 42, no. 8, pp. 3184–3196, 2013.

[82] S. Sang, W. Zhang, and Y. Zhao, *Review on the design art of biosensors*. INTECH Open Access Publisher, 2013.

[83] A. L. Washburn, M. S. Luchansky, A. L. Bowman, and R. C. Bailey, "Quantitative, label-free detection of five protein biomarkers using multiplexed arrays of silicon photonic microring resonators," *Analytical chemistry*, vol. 82, no. 1, pp. 69–72, 2009.

[84] A. L. Washburn, L. C. Gunn, and R. C. Bailey, "Label-free quantitation of a cancer biomarker in complex media using silicon photonic microring resonators," *Analytical chemistry*, vol. 81, no. 22, pp. 9499–9506, 2009.

[85] M. S. Luchansky and R. C. Bailey, "Silicon photonic microring resonators for quantitative cytokine detection and t-cell secretion analysis," *Analytical chemistry*, vol. 82, no. 5, pp. 1975–1981, 2010.

[86] F. Ghasemi, E. S. Hosseini, X. Song, D. S. Gottfried, M. Chamanzar, M. Raeiszadeh, R. D. Cummings, A. A. Eftekhar, and A. Adibi, "Multiplexed detection of lectins using integrated glycan-coated microring resonators," *Biosensors and Bioelectronics*, vol. 80, pp. 682–690, 2016.

[87] Y. Sun and X. Fan, "Optical ring resonators for biochemical and chemical sensing," *Analytical and bioanalytical chemistry*, vol. 399, no. 1, pp. 205–211, 2011.

[88] M. Soltani, S. Yegnanarayanan, and A. Adibi, "Ultra-high q planar silicon microdisk resonators for chip-scale silicon photonics," *Optics express*, vol. 15, no. 8, pp. 4694–4704, 2007.

[89] E. S. Hosseini, S. Yegnanarayanan, A. H. Atabaki, M. Soltani, and A. Adibi, "High quality planar silicon nitride microdisk resonators for integrated photonics in the visible wavelength range," *Optics express*, vol. 17, no. 17, pp. 14 543–14 551, 2009.

[90] K. J. Vahala, "Optical microcavities," *Nature*, vol. 424, no. 6950, pp. 839–846, 2003.

[91] D. Armani, T. Kippenberg, S. Spillane, and K. Vahala, "Ultra-high-q toroid microcavity on a chip," *Nature*, vol. 421, no. 6926, pp. 925–928, 2003.

[92] H. Lee, T. Chen, J. Li, K. Y. Yang, S. Jeon, O. Painter, and K. J. Vahala, "Chemically etched ultrahigh-q wedge-resonator on a silicon chip," *Nature Photonics*, vol. 6, no. 6, pp. 369–373, 2012.

[93] N. M. Hanumegowda, I. M. White, and X. Fan, "Aqueous mercuric ion detection with microsphere optical ring resonator sensors," *Sensors and Actuators B: Chemical*, vol. 120, no. 1, pp. 207–212, 2006.

[94] R. Soref, J. Guo, and G. Sun, "Low-energy mos depletion modulators in silicon-on-insulator micro-donut resonators coupled to bus waveguides," *Optics express*, vol. 19, no. 19, pp. 18 122–18 134, 2011.

[95] Z. Xia, A. A. Eftekhar, M. Soltani, B. Momeni, Q. Li, M. Chamanzar, S. Yegnanarayanan, and A. Adibi, "High resolution on-chip spectroscopy based on miniaturized microdonut resonators," *Optics express*, vol. 19, no. 13, pp. 12 356–12 364, 2011.

[96] P. Dumon, W. Bogaerts, V. Wiaux, J. Wouters, S. Beckx, J. Van Campenhout, D. Taillaert, B. Luyssaert, P. Bienstman, D. Van Thourhout, *et al.*, "Low-loss soi photonic wires and ring resonators fabricated with deep uv lithography," *IEEE Photonics Technology Letters*, vol. 16, no. 5, pp. 1328–1330, 2004.

[97] F. DellOlio and V. M. Passaro, "Optical sensing by optimized silicon slot waveguides," *Optics Express*, vol. 15, no. 8, pp. 4977–4993, 2007.

[98] T. Claes, J. G. Molera, K. De Vos, E. Schacht, R. Baets, and P. Bienstman, "Label-free biosensing with a slot-waveguide-based ring resonator in silicon on insulator," *IEEE Photonics journal*, vol. 1, no. 3, pp. 197–204, 2009.

[99] P Prabhathan, V. Murukeshan, Z. Jing, and P. V. Ramana, "Compact soi nanowire refractive index sensor using phase shifted bragg grating," *Optics express*, vol. 17, no. 17, pp. 15 330–15 341, 2009.

[100] B. Little, S. Chu, W Pan, D Ripin, T Kaneko, Y Kokubun, and E Ippen, "Vertically coupled glass microring resonator channel dropping filters," *IEEE Photonics Technology Letters*, vol. 11, no. 2, pp. 215–217, 1999.

[101] W. H. Pernice, C. Xiong, and H. X. Tang, "High q micro-ring resonators fabricated from polycrystalline aluminum nitride films for near infrared and visible photonics," *Optics express*, vol. 20, no. 11, pp. 12 261–12 269, 2012.

[102] D. Rabus, M Hamacher, U Troppenz, and H Heidrich, "High-q channel-dropping filters using ring resonators with integrated soas," *IEEE Photonics Technology Letters*, vol. 14, no. 10, pp. 1442–1444, 2002.

[103] Z. Xia, S. C. Davis, A. A. Eftekhar, A. S. Gordin, M. Askari, Q. Li, F. Ghasemi, K. H. Sandhage, and A. Adibi, "Magnesiothermically formed porous silicon thin films on silicon-on-insulator optical microresonators for high-sensitivity detection," *Advanced Optical Materials*, vol. 2, no. 3, pp. 235–239, 2014.

[104] G. A. Rodriguez, S. Hu, and S. M. Weiss, "Porous silicon ring resonator for compact, high sensitivity biosensing applications," *Optics express*, vol. 23, no. 6, pp. 7111–7119, 2015.

[105] P. Rabiei, W. H. Steier, C. Zhang, and L. R. Dalton, "Polymer micro-ring filters and modulators," *Journal of lightwave technology*, vol. 20, no. 11, p. 1968, 2002.

[106] X. Fan, I. M. White, S. I. Shopova, H. Zhu, J. D. Suter, and Y. Sun, "Sensitive optical biosensors for unlabeled targets: A review," *analytica chimica acta*, vol. 620, no. 1, pp. 8–26, 2008.

[107] H. K. Hunt and A. M. Armani, "Label-free biological and chemical sensors," *Nanoscale*, vol. 2, no. 9, pp. 1544–1559, 2010.

[108] A. L. Washburn and R. C. Bailey, "Photonics-on-a-chip: Recent advances in integrated waveguides as enabling detection elements for real-world, lab-on-a-chip biosensing applications," *Analyst*, vol. 136, no. 2, pp. 227–236, 2011.

[109] W. Bogaerts, P. De Heyn, T. Van Vaerenbergh, K. De Vos, S. Kumar Selvaraja, T. Claes, P. Dumon, P. Bienstman, D. Van Thourhout, and R. Baets, "Silicon microring resonators," *Laser & Photonics Reviews*, vol. 6, no. 1, pp. 47–73, 2012.

[110] F. Ghasemi, M. Chamanzar, A. A. Eftekhar, and A. Adibi, "An efficient technique for the reduction of wavelength noise in resonance-based integrated photonic sensors," *Analyst*, vol. 139, no. 22, pp. 5901–5910, 2014.

[111] D.-X. Xu, M Vachon, A Densmore, R Ma, S Janz, A Delâge, J Lapointe, P Cheben, J. Schmid, E Post, *et al.*, "Real-time cancellation of temperature induced resonance shifts in soi wire waveguide ring resonator label-free biosensor arrays," *Optics express*, vol. 18, no. 22, pp. 22 867–22 879, 2010.

[112] M. Iqbal, M. A. Gleeson, B. Spaugh, F. Tybor, W. G. Gunn, M. Hochberg, T. Baehr-Jones, R. C. Bailey, and L. C. Gunn, "Label-free biosensor arrays based on silicon ring resonators and high-speed optical scanning instrumentation," *IEEE Journal of Selected Topics in Quantum Electronics*, vol. 16, no. 3, pp. 654–661, 2010.

[113] M. S. Luchansky, A. L. Washburn, T. A. Martin, M. Iqbal, L. C. Gunn, and R. C. Bailey, "Characterization of the evanescent field profile and bound mass sensitivity of a label-free silicon photonic microring resonator biosensing platform," *Biosensors and Bioelectronics*, vol. 26, no. 4, pp. 1283–1291, 2010.

[114] S. M. Grist, S. A. Schmidt, J. Flueckiger, V. Donzella, W. Shi, S. T. Fard, J. T. Kirk, D. M. Ratner, K. C. Cheung, and L. Chrostowski, "Silicon photonic microdisk resonators for label-free biosensing," *Optics express*, vol. 21, no. 7, pp. 7994–8006, 2013.

[115] S. Schmidt, J. Flueckiger, W. Wu, S. M. Grist, S. T. Fard, V. Donzella, P. Khumwan, E. R. Thompson, Q. Wang, P. Kulik, *et al.*, "Improving the performance of silicon photonic rings, disks, and bragg gratings for use in label-free biosensing," in *SPIE NanoScience+ Engineering*, International Society for Optics and Photonics, 2014, pp. 91660M–91660M.

[116] A. Yalcin, K. C. Popat, J. C. Aldridge, T. A. Desai, J. Hryniewicz, N. Chbouki, B. E. Little, O. King, V. Van, S. Chu, *et al.*, "Optical sensing of biomolecules using microring resonators," *IEEE Journal of Selected Topics in Quantum Electronics*, vol. 12, no. 1, pp. 148–155, 2006.

[117] A Ksendzov and Y Lin, "Integrated optics ring-resonator sensors for protein detection," *Optics letters*, vol. 30, no. 24, pp. 3344–3346, 2005.

[118] F. Ghasemi, A. A. Eftekhar, D. S. Gottfried, X. Song, R. D. Cummings, and A. Adibi, "Self-referenced silicon nitride array microring biosensor for toxin detection using glycans at visible wavelength," in *SPIE BiOS*, International Society for Optics and Photonics, 2013, 85940A–85940A.

[119] C.-Y. Chao, W. Fung, and L. J. Guo, "Polymer microring resonators for biochemical sensing applications," *IEEE Journal of selected Topics in quantum electronics*, vol. 12, no. 1, pp. 134–142, 2006.

[120] P. Girault, N. Lorrain, L. Poffo, M. Guendouz, J. Lemaitre, C. Carré, M. Gadonna, D. Bosc, and G. Vignaud, "Integrated polymer micro-ring resonators for optical sensing applications," *Journal of Applied Physics*, vol. 117, no. 10, p. 104 504, 2015.

[121] M. Soltani, S. Yegnanarayanan, Q. Li, and A. Adibi, "Systematic engineering of waveguide-resonator coupling for silicon microring/microdisk/racetrack resonators: Theory and experiment," *IEEE Journal of Quantum Electronics*, vol. 46, no. 8, pp. 1158–1169, 2010.

[122] A. A. Eftekhar, Z. Xia, F. Ghasemi, and A. Adibi, "Ultra-compact multiplexed lab-on-chip sensors using miniaturized integrated photonic resonators," in *Photonics Conference (IPC), 2012 IEEE*, IEEE, 2012, pp. 439–440.

[123] K. Worhoff, P. V. Lambeck, and A. Driessen, "Design, tolerance analysis, and fabrication of silicon oxynitride based planar optical waveguides for communication devices," *Journal of Lightwave Technology*, vol. 17, no. 8, pp. 1401–1407, 1999.

[124] A. Mekis, S. Gloeckner, G. Masini, A. Narasimha, T. Pinguet, S. Sahni, and P. De Dobbelaere, "A grating-coupler-enabled cmos photonics platform," *IEEE Journal of Selected Topics in Quantum Electronics*, vol. 17, no. 3, pp. 597–608, 2011.

[125] P. E. Barclay, K. Srinivasan, M. Borselli, and O. Painter, "Efficient input and output fiber coupling to a photonic crystal waveguide," *Optics letters*, vol. 29, no. 7, pp. 697–699, 2004.

[126] D.-X. Xu, J. H. Schmid, G. T. Reed, G. Z. Mashanovich, D. J. Thomson, M. Nedeljkovic, X. Chen, D. Van Thourhout, S. Keyvaninia, and S. K. Selvaraja, "Silicon photonic integration platformhave we found the sweet spot?" *IEEE Journal of Selected Topics in Quantum Electronics*, vol. 20, no. 4, pp. 189–205, 2014.

[127] X. Chen, C. Li, C. K. Fung, S. M. Lo, and H. K. Tsang, "Apodized waveguide grating couplers for efficient coupling to optical fibers," *IEEE Photonics Technology Letters*, vol. 22, no. 15, pp. 1156–1158, 2010.

[128] Z. Cheng, X. Chen, C. Wong, K. Xu, C. K. Fung, Y. Chen, and H. K. Tsang, "Focusing subwavelength grating coupler for mid-infrared suspended membrane waveguide," *Optics letters*, vol. 37, no. 7, pp. 1217–1219, 2012.

[129] G. Roelkens, D. Van Thourhout, and R. Baets, "High efficiency grating coupler between silicon-on-insulator waveguides and perfectly vertical optical fibers," *Optics letters*, vol. 32, no. 11, pp. 1495–1497, 2007.

[130] B. Schmid, A. Petrov, and M. Eich, "Optimized grating coupler with fully etched slots," *Optics express*, vol. 17, no. 13, pp. 11 066–11 076, 2009.

[131] M. A. Cooper, "Optical biosensors in drug discovery," *Nature reviews. Drug discovery*, vol. 1, no. 7, p. 515, 2002.

[132] F. Abbasi, H. Mirzadeh, and A.-A. Katbab, "Modification of polysiloxane polymers for biomedical applications: A review," *Polymer International*, vol. 50, no. 12, pp. 1279–1287, 2001.

[133] J. C. McDonald, D. C. Duffy, J. R. Anderson, D. T. Chiu, H. Wu, O. J. Schueller, and G. M. Whitesides, "Fabrication of microfluidic systems in poly (dimethylsiloxane)," *Electrophoresis*, vol. 21, no. 1, pp. 27–40, 2000.

[134] P. Kim, K. W. Kwon, M. C. Park, S. H. Lee, S. M. Kim, and K. Y. Suh, "Soft lithography for microfluidics: A review," 2008.

[135] J. M. Ng, I. Gitlin, A. D. Stroock, and G. M. Whitesides, "Components for integrated poly (dimethylsiloxane) microfluidic systems," *Electrophoresis*, vol. 23, no. 20, pp. 3461–3473, 2002.

[136] H. Lorenz, M Despont, N Fahrni, N LaBianca, P. Renaud, and P Vettiger, "Su-8: A low-cost negative resist for mems," *Journal of Micromechanics and Microengineering*, vol. 7, no. 3, p. 121, 1997.

[137] R. Yang, B.-R. Lu, J. Wan, S.-Q. Xie, Y. Chen, E. Huq, X.-P. Qu, and R. Liu, "Fabrication of micro/nano fluidic channels by nanoimprint lithography and bonding using su-8," *Microelectronic Engineering*, vol. 86, no. 4-6, pp. 1379–1381, 2009.

[138] E. H. Conradie and D. F. Moore, "Su-8 thick photoresist processing as a functional material for mems applications," *Journal of Micromechanics and Microengineering*, vol. 12, no. 4, p. 368, 2002.

[139] L. J. Kricka, "Microchips, microarrays, biochips and nanochips: Personal laboratories for the 21st century," *Clinica Chimica Acta*, vol. 307, no. 1-2, pp. 219–223, 2001.

[140] C.-Y. Huang, C.-H. Kuo, W.-T. Hsiao, K.-C. Huang, S.-F. Tseng, and C.-P. Chou, "Glass biochip fabrication by laser micromachining and glass-molding process," *Journal of Materials Processing Technology*, vol. 212, no. 3, pp. 633–639, 2012.

[141] N. Zammatteo, L. Jeanmart, S. Hamels, S. Courtois, P. Louette, L. Hevesi, and J. Remacle, "Comparison between different strategies of covalent attachment of dna to glass surfaces to build dna microarrays," *Analytical biochemistry*, vol. 280, no. 1, pp. 143–150, 2000.

[142] A. J. Hart and A. H. Slocum, "Rapid growth and flow-mediated nucleation of millimeter-scale aligned carbon nanotube structures from a thin-film catalyst," *The Journal of Physical Chemistry B*, vol. 110, no. 16, pp. 8250–8257, 2006.

[143] J. Wang and Y. Lin, "Functionalized carbon nanotubes and nanofibers for biosensing applications," *TrAC Trends in Analytical Chemistry*, vol. 27, no. 7, pp. 619–626, 2008.

[144] J. V. Veetil and K. Ye, "Development of immunosensors using carbon nanotubes," *Biotechnology progress*, vol. 23, no. 3, pp. 517–531, 2007.

[145] E. Asenath Smith and W. Chen, "How to prevent the loss of surface functionality derived from aminosilanes," *Langmuir*, vol. 24, no. 21, pp. 12 405–12 409, 2008.

[146] A. Bange, H. B. Halsall, and W. R. Heineman, "Microfluidic immunosensor systems," *Biosensors and Bioelectronics*, vol. 20, no. 12, pp. 2488–2503, 2005.

[147] E. H. Shah, "Electrical resistance in carbon nanotube–insulator–metal diode arrays for optical rectenna," PhD thesis, Georgia Institute of Technology, 2016.

[148] R. G. Acres, A. V. Ellis, J. Alvino, C. E. Lenahan, D. A. Khodakov, G. F. Metha, and G. G. Andersson, "Molecular structure of 3-aminopropyltriethoxysilane layers formed on silanol-terminated silicon surfaces," *The Journal of Physical Chemistry C*, vol. 116, no. 10, pp. 6289–6297, 2012.

[149] H. Yang, F. Li, C. Shan, D. Han, Q. Zhang, L. Niu, and A. Ivaska, "Covalent functionalization of chemically converted graphene sheets via silane and its reinforcement," *Journal of Materials Chemistry*, vol. 19, no. 26, pp. 4632–4638, 2009.

[150] F. Zhang, K. Sautter, A. M. Larsen, D. A. Findley, R. C. Davis, H. Samha, and M. R. Linford, "Chemical vapor deposition of three aminosilanes on silicon dioxide: Surface characterization, stability, effects of silane concentration, and cyanine dye adsorption," *Langmuir*, vol. 26, no. 18, pp. 14 648–14 654, 2010.

[151] E. P. Plueddemann, "Chemistry of silane coupling agents," in *Silane coupling agents*, Springer, 1991, pp. 31–54.

[152] B Arkles, J. Steinmetz, J Zazyczny, and P Mehta, "Factors contributing to the stability of alkoxysilanes in aqueous solution," *Journal of Adhesion Science and Technology*, vol. 6, no. 1, pp. 193–206, 1992.

[153] A. Ahmed, C. Bonner, and T. A. Desai, "Bioadhesive microdevices for drug delivery: A feasibility study," *Biomedical Microdevices*, vol. 3, no. 2, pp. 89–96, 2001.

[154] J. Kim, P. Seidler, C. Fill, and L. S. Wan, "Investigations of the effect of curing conditions on the structure and stability of amino-functionalized organic films on silicon substrates by fourier transform infrared spectroscopy, ellipsometry, and fluorescence microscopy," *Surface Science*, vol. 602, no. 21, pp. 3323–3330, 2008.

[155] N. Aissaoui, L. Bergaoui, J. Landoulsi, J.-F. Lambert, and S. Boujday, "Silane layers on silicon surfaces: Mechanism of interaction, stability, and influence on protein adsorption," *Langmuir*, vol. 28, no. 1, pp. 656–665, 2011.

[156] Y. G. Hsu and J. H. Huang, "Model reaction of epoxy-containing siloxane," *Journal of non-crystalline solids*, vol. 208, no. 3, pp. 259–266, 1996.

[157] B Riegel, S Blittersdorf, W Kiefer, S Hofacker, M Müller, and G Schottner, "Kinetic investigations of hydrolysis and condensation of the glycidoxypropyltrimethoxysilane / aminopropyltriethoxy-silane system by means of ft-raman spectroscopy i," *Journal of non-crystalline solids*, vol. 226, no. 1, pp. 76–84, 1998.

[158] N. S. K. Gunda, M. Singh, L. Norman, K. Kaur, and S. K. Mitra, "Optimization and characterization of biomolecule immobilization on silicon substrates using (3-aminopropyl) triethoxysilane (aptes) and glutaraldehyde linker," *Applied Surface Science*, vol. 305, pp. 522–530, 2014.

[159] N. R. Glass, R. Tjeung, P. Chan, L. Y. Yeo, and J. R. Friend, "Organosilane deposition for microfluidic applications," *Biomicrofluidics*, vol. 5, no. 3, p. 036 501, 2011.

[160] J. A. Howarter and J. P. Youngblood, "Optimization of silica silanization by 3-aminopropyltriethoxysilane," *Langmuir*, vol. 22, no. 26, pp. 11 142–11 147, 2006.

[161] O. Seitz, P. G. Fernandes, R. Tian, N. Karnik, H.-C. Wen, H. Stiegler, R. A. Chapman, E. M. Vogel, and Y. J. Chabal, "Control and stability of self-assembled monolayers under biosensing conditions," *Journal of Materials Chemistry*, vol. 21, no. 12, pp. 4384–4392, 2011.

[162] R. M. Pasternack, S. Rivillon Amy, and Y. J. Chabal, "Attachment of 3-(aminopropyl) triethoxysilane on silicon oxide surfaces: Dependence on solution temperature," *Langmuir*, vol. 24, no. 22, pp. 12 963–12 971, 2008.

[163] A Ramachandran, S Wang, J Clarke, S. Ja, D Goad, L Wald, E. Flood, E Knobbe, J. Hryniewicz, S. Chu, *et al.*, "A universal biosensing platform based on optical micro-ring resonators," *Biosensors and Bioelectronics*, vol. 23, no. 7, pp. 939–944, 2008.

[164] G. T. Hermanson, *Bioconjugate techniques*. Academic press, 2013.

[165] B. Johs, J. A. Woollam, C. M. Herzinger, J. N. Hilfiker, R. A. Synowicki, and C. L. Bungay, "Overview of variable-angle spectroscopic ellipsometry (vase): Ii. advanced applications," in *Optical Metrology: A Critical Review*, International Society for Optics and Photonics, vol. 10294, 1999, p. 1 029 404.

[166] D. L. Plata, E. R. Meshot, C. M. Reddy, A. J. Hart, and P. M. Gschwend, "Multiple alkynes react with ethylene to enhance carbon nanotube synthesis, suggesting a polymerization-like formation mechanism," *ACS nano*, vol. 4, no. 12, pp. 7185–7192, 2010.

[167] V. Krivitsky, L.-C. Hsiung, A. Lichtenstein, B. Brudnik, R. Kantaev, R. Elnathan, A. Pevzner, A. Khatchtourints, and F. Patolsky, "Si nanowires forest-based on-chip biomolecular filtering, separation and preconcentration devices: Nanowires do it all," *Nano letters*, vol. 12, no. 9, pp. 4748–4756, 2012.

[168] N. S. K. Gunda, M. Singh, Y. Purwar, S. L. Shah, K. Kaur, and S. K. Mitra, "Microspot with integrated pillars (msip) for detection of dengue virus ns1," *Biomedical microdevices*, vol. 15, no. 6, pp. 959–971, 2013.

[169] N. Yanagisawa and D. Dutta, "Enhancement in the sensitivity of microfluidic enzyme-linked immunosorbent assays through analyte preconcentration," *Analytical chemistry*, vol. 84, no. 16, pp. 7029–7036, 2012.

[170] E. Dressaire and A. Sauret, "Clogging of microfluidic systems," *Soft matter*, vol. 13, no. 1, pp. 37–48, 2017.

[171] J. Han, J. Fu, and R. B. Schoch, "Molecular sieving using nanofilters: Past, present and future," *Lab on a Chip*, vol. 8, no. 1, pp. 23–33, 2008.

[172] M Van Hecke, "Jamming of soft particles: Geometry, mechanics, scaling and isostaticity," *Journal of Physics: Condensed Matter*, vol. 22, no. 3, p. 033 101, 2009.

[173] D. Genovese and J. Sprakel, "Crystallization and intermittent dynamics in constricted microfluidic flows of dense suspensions," *Soft Matter*, vol. 7, no. 8, pp. 3889–3896, 2011.

[174] G. M. Whitesides and B. Grzybowski, "Self-assembly at all scales," *Science*, vol. 295, no. 5564, pp. 2418–2421, 2002.

[175] E. Di Stasio and R. De Cristofaro, "The effect of shear stress on protein conformation: Physical forces operating on biochemical systems: The case of von willebrand factor," *Biophysical chemistry*, vol. 153, no. 1, pp. 1–8, 2010.

[176] E. Sollier, C. Murray, P. Maoddi, and D. Di Carlo, "Rapid prototyping polymers for microfluidic devices and high pressure injections," *Lab on a Chip*, vol. 11, no. 22, pp. 3752–3765, 2011.

[177] C. K. Dixit, S. K. Vashist, F. T. ONeill, B. OReilly, B. D. MacCraith, and R. OKennedy, "Development of a high sensitivity rapid sandwich elisa procedure and its comparison with the conventional approach," *Analytical chemistry*, vol. 82, no. 16, pp. 7049–7052, 2010.

[178] C. K. Dixit, S. K. Vashist, B. D. MacCraith, and R. O'kennedy, "Multisubstrate-compatible elisa procedures for rapid and high-sensitivity immunoassays," *nature protocols*, vol. 6, no. 4, p. 439, 2011.

[179] ClickChemistry-Tools, *Pc biotin-nhs ester*, Click Chemistry Website, 2017.

[180] M. F. Clark and A. Adams, "Characteristics of the microplate method of enzyme-linked immunosorbent assay for the detection of plant viruses," *Journal of general virology*, vol. 34, no. 3, pp. 475–483, 1977.

[181] R. M. Lequin, "Enzyme immunoassay (eia)/enzyme-linked immunosorbent assay (elisa)," *Clinical chemistry*, vol. 51, no. 12, pp. 2415–2418, 2005.

[182] R. D. Cummings and M. E. Etzler, "Antibodies and lectins in glycan analysis," 2009.

[183] J. Wu, J. Zhu, H. Yin, R. J. Buckanovich, and D. M. Lubman, "Analysis of glycan variation on glycoproteins from serum by the reverse lectin-based elisa assay," *Journal of proteome research*, vol. 13, no. 4, pp. 2197–2204, 2014.

[184] S. Chen, T. LaRoche, D. Hamelinck, D. Bergsma, D. Brenner, D. Simeone, R. E. Brand, and B. B. Haab, "Multiplexed analysis of glycan variation on native proteins captured by antibody microarrays," *Nature methods*, vol. 4, no. 5, p. 437, 2007.

[185] L. Klukova, T. Bertok, M. Petrikova, A. Sediva, D. Mislovicova, J. Katrlik, A. Vikartovska, J. Filip, P. Kasak, A. Andicsová-Eckstein, *et al.*, "Glycoprofiling as a novel tool in serological assays of systemic sclerosis: A comparative study with three bioanalytical methods," *Analytica chimica acta*, vol. 853, pp. 555–562, 2015.

[186] Y. Li, S.-C. Tao, G. S. Bova, A. Y. Liu, D. W. Chan, H. Zhu, and H. Zhang, "Detection and verification of glycosylation patterns of glycoproteins from clinical specimens using lectin microarrays and lectin-based immunosorbent assays," *Analytical chemistry*, vol. 83, no. 22, pp. 8509–8516, 2011.

[187] Pierce, *Ez-link nhs-pc-lc-biotin*, Pierce Website, 2017.

[188] P. Damborskỳ, K. M. Koczula, A. Gallotta, and J. Katrlík, "Lectin-based lateral flow assay: Proof-of-concept," *Analyst*, vol. 141, no. 23, pp. 6444–6448, 2016.

[189] P. Damborskỳ, M. Zámorová, and J. Katrlík, "Determining the binding affinities of prostate-specific antigen to lectins: Spr and microarray approaches," *Proteomics*, vol. 16, no. 24, pp. 3096–3104, 2016.

[190] P. Damborskỳ, D. Damborská, Š. Belickỳ, J. Tkáč, and J. Katrlík, "Sweet strategies in prostate cancer biomarker research: Focus on a prostate specific antigen," *BioNanoScience*, vol. 8, no. 2, pp. 690–700, 2018.

[191] P. Jolly, P. Damborsky, N. Madaboosi, R. R. Soares, V. Chu, J. P. Conde, J. Katrlik, and P. Estrela, "Dna aptamer-based sandwich microfluidic assays for dual quantification and multi-glycan profiling of cancer biomarkers," *Biosensors and Bioelectronics*, vol. 79, pp. 313–319, 2016.

[192] ThermoFisherScienctific. (2018). Psa (free) human elisa kit.

[193] L. Zhu, J. Xu, Y. Xiu, Y. Sun, D. W. Hess, and C. Wong, "Growth and electrical characterization of high-aspect-ratio carbon nanotube arrays," *Carbon*, vol. 44, no. 2, pp. 253–258, 2006.

[194] V Datsyuk, M Kalyva, K Papagelis, J Parthenios, D Tasis, A Siokou, I Kallitsis, and C Galiotis, "Chemical oxidation of multiwalled carbon nanotubes," *Carbon*, vol. 46, no. 6, pp. 833–840, 2008.

[195] F Avilés, J. Cauich-Rodríguez, L Moo-Tah, A May-Pat, and R Vargas-Coronado, "Evaluation of mild acid oxidation treatments for mwcnt functionalization," *Carbon*, vol. 47, no. 13, pp. 2970–2975, 2009.

[196] Y. Peng and H. Liu, "Effects of oxidation by hydrogen peroxide on the structures of multiwalled carbon nanotubes," *Industrial & Engineering Chemistry Research*, vol. 45, no. 19, pp. 6483–6488, 2006.

[197] X. Yu, S. N. Kim, F. Papadimitrakopoulos, and J. F. Rusling, "Protein immunosensor using single-wall carbon nanotube forests with electrochemical detection of enzyme labels," *Molecular Biosystems*, vol. 1, no. 1, pp. 70–78, 2005.

[198] Y. Gao and I. Kyratzis, *Covalent immobilization of proteins on carbon nanotubes using the cross-linker 1-ethyl-3-(3-dimethylaminopropyl) carbodiimidea critical assessment*, 2008.

[199] M. Soltani, "Novel integrated silicon nanophotonic structures using ultra-high q resonators," PhD thesis, Georgia Institute of Technology, 2009.

[200] A. Usman, R. Dehghannasiri, A. Eftekhar, and A. Adibi, "Highly sensitive biomolecular detection using compact high-q silicon spiral resonators," in *Frontiers in Optics*, Optical Society of America, 2017, FM3D–1.

[201] Y. Wang, J. Flueckiger, C. Lin, and L. Chrostowski, "Universal grating coupler design," in *Photonics North 2013*, International Society for Optics and Photonics, vol. 8915, 2013, 89150Y.

[202] L. Chrostowski and M. Hochberg, *Silicon photonics design: from devices to systems*. Cambridge University Press, 2015.

[203] Z. Xia, "Highly sensitive, multiplexed integrated photonic structures for lab-on-a-chip sensing," PhD thesis, Georgia Institute of Technology, 2015.

[204] L. Chrostowski, S. Grist, J. Flueckiger, W. Shi, X. Wang, E. Ouellet, H. Yun, M. Webb, B. Nie, Z. Liang, *et al.*, "Silicon photonic resonator sensors and devices," in *SPIE LASE*, International Society for Optics and Photonics, 2012, pp. 823 620–823 620.

[205] I. J. Goldstein, H. C. Winter, and R. D. Poretz, "Plant lectins: Tools for the study of complex carbohydrates," in *New Comprehensive Biochemistry*, vol. 29, Elsevier, 1997, pp. 403–474.

VITA

Ahmad Usman received his B.Sc. and M.Sc. in Electrical Engineering from University of Engineering and Technology (UET), Lahore, Pakistan in 2008 and 2011, respectively. At the Georgia Institute of Technology, he has received his M.Sc. in Electrical Engineering (majors in Optics and Microsystems) and M.Sc. in Mechanical Engineering (majors in MEMS and Nanotechnology) in 2014 and 2016, respectively. He also holds the certification of MEMS from the Georgia Institute of Technology. He is a recipient of the prestigious US Fulbright scholarship and has been awarded HRDI-UESTPs/UETs scholarship award from the Higher Education Commission (HEC) of Pakistan.

Ahmad has been working on silicon-based optical microresonator platforms for on-chip cancer detection during his PhD at the Georgia Institute of Technology. His work involves development of multi-functional and high throughput MEMS based optical and electrical platforms for biosensing.

He also has interests and worked in the domain of Renewable Energy, Smart Grids, Power Electronics, and Wireless Power Transfer. Besides his research, he has been a member of The IET and IEEE, has served as a senator in the Georgia Techs Student Government Association (SGA,2015-16) and has been the vice-president of the Pakistan Student Association (PSA,2014-15). He is an amateur photographer, a cooking enthusiast, and has traveled to 35 states in US during his PhD.